Université catholique de Louvain

Secteur des sciences et technologies
Earth and Life Institute



Methane clathrate hydrate stability in the martian subsurface and outgassing scenarios

Elodie Gloesener

Thèse présentée en vue de l'obtention du grade de
Docteur en Sciences

Septembre 2019

"*You know what Mars is? It's like a thing I got for Christmas seventy years ago–don't know if you ever had one–they called them kaleidoscopes, bits of crystal and cloth and beads and pretty junk. You held it up to the sunlight and looked in through at it, and it took your breath away. All the patterns! Well, that's Mars. Enjoy it.*"

–Ray Bradbury
The Martian Chronicles

Remerciements

Je voudrais remercier toutes les personnes qui ont contribué, de près ou de loin, à la réalisation de ce travail de thèse. Et parce que ces dernières années ont été riches en émotions, le chemin aurait été immensément plus compliqué sans la famille/les amis/les collègues avec qui les partager.

Merci à ma promotrice, Véronique Dehant, pour son dynamisme, son enthousiasme sans faille et ses retours motivants sur mon travail. Merci à mon co-promoteur, Özgür Karatekin, pour sa confiance et la liberté qu'il m'a laisée quant à la direction que je voulais donner à mes recherches. Les nombreuses collaborations scientifiques qu'il a initiées ont, sans aucun doute, été des moteurs dans le développement de mes compétences et connaissances tout au long de mon parcours doctoral.

Je remercie également les membres de mon jury, Olivier Mousis, Ann Carine Vandaele, Michel Crucifix, Johan Yans et Marie-Laurence De Keersmaecker pour avoir pris le temps de lire ce manuscrit et pour leur commentaires constructifs qui ont permis l'amélioration de ce dernier.

Durant ma thèse, j'ai eu l'occasion d'effectuer des manipulations expérimentales (dont la création et l'enflammement de clathrates de méthane!). Merci à Mathieu Choukroun et Tuan Vu de m'avoir accueillie dans leur équipe au Jet Propulsion Laboratory. Leur disponibilité et leur expertise ont grandement contribué à faire de ce séjour une expérience enrichissante.

Merci à Orkun Temel, Jorge Pla-García, Scot Rafkin, Jean-Michel Herri, Baptiste Bouillot et Johannes Benkhoff pour les échanges positifs et les collaborations fructueuses. Je tiens également à remercier Germán Martínez and Michael D. Smith pour avoir partagé les données des instruments REMS (Rover Environmental Monitoring Station) et TES (Thermal Emission Spectrometer) sur le cycle de la vapeur d'eau sur Mars.

À mes collègues et amis, d'hier et d'aujourd'hui, dont la bonne humeur, les histoires et les rires ont égayé ces années de thèse. Merci à Antony, Sébastien, Marie-Hélène, Jérémy, Marie-Julie, Rose-Marie, Tilio, Mikael, Marie, Matthias, Andres, Luca, Alphonso, Alexis, Ping, Michel, Bart, Raphaël, Lebi, Birgit, Aymeric, Pascale, Nicolas B., Bruno, Tim, Koen, Ronny, Cédric, Lena, Pierre, Nicolas G., Pascal, Laurence, Maria, Aurélien H., Wim, Paul, Aurélien A., Amedeo, Elisa, Gregoire, Ann Carine, Séverine, Valérie, Arnaud, Yannick, Lori, Sébastien V., Frank, Nuno, Fabien, Ian, Arianna, Loïc et Shohei. Mention spéciale à Margaux et Kevin pour une ambiance en conférence toujours réussie.

À mes amis, merci pour leur présence dans les joies comme dans les peines, à travers les doutes et les certitudes. En particulier, merci à :

- *La fine équipe*, Laura et Sandrine, parce que vous êtes une bouffée d'oxygène, une source d'apaisement dans les moments de stress.
- Mes *Blue Brothers*, Audrey, Vivien et Amandine, pour nos éternels appels Skype et téléphoniques, nos discussions animées autour d'un verre (ou plus) à Liège, Bruxelles et Kiruna.
- Mes *Friends*, Audrey, Eli, Johan, Raf, Nico, Fanny, Marine, Thibaut, Laura et Damien, parce que "I'll be there for you" est un peu notre refrain.

Je termine ces remerciements avec les membres de ma famille auprès desquels j'ai toujours pu trouver encouragements et réconfort. Merci à mon grand-père, mes soeurs de coeur, Bernadette et Catherine, Daniel, Véronique, Marie, Antoine, Clothilde, Yves, Vivette, Véro et Pierre pour les fous rires sans arrêt renouvelés, l'énergie insufflée et l'inspiration retrouvée. Merci à ma grand-mère qui m'a soutenue tout au long de ma vie. Je suis sûre qu'elle aurait fait partie de mes premiers lecteurs si elle avait pu. Merci à mes *Sistaaa*, Julie et Kory, qui me montrent chaque jour que, quelles que soient les difficultés, il faut poursuivre ses rêves. Merci à ma mère pour son soutien indéfectible depuis le début. Enfin, je remercie mon père pour sa relecture attentive, ses commentaires éclairés, son écoute, ses encouragements, sa bienveillance et j'en passe. Merci papa d'avoir toujours cru en moi!

Contents

1 Introduction **1**

2 Methane on Mars **5**
2.1 Observations of martian methane 6
2.2 Theoretical objections 14
2.3 Methane generation mechanisms on Mars 16
2.3.1 Biological origin 17
2.3.2 Geologic production 19
2.3.3 Meteoritic and cometary source 22
2.3.4 Photochemical production 24
2.4 Methane subsurface reservoirs on Mars 25
2.5 Methane loss mechanisms on Mars 27
2.6 Current and future missions 30
2.7 Summary 31

3 Clathrate hydrates **33**
3.1 Molecular structure 34
3.1.1 Structure I 35
3.1.2 Structure II 35
3.1.3 Structure H 36
3.1.4 High pressure clathrate structures 38
3.2 Characteristics of guest molecules 38
3.3 Properties: clathrate vs water ice 40
3.4 Stability of clathrate hydrates 42
3.4.1 Clathrate stability zone 44
3.5 Formation and dissociation processes 46
3.6 Clathrate hydrates in the Solar System 47
3.6.1 Comets 47
3.6.2 Mars 48
3.6.3 Outer Solar System 49
3.7 Summary 50

4 Models **51**
4.1 Methane migration in the martian crust and outgassing scenarios . . . 52
4.2 Thermodynamic modelling of clathrates . . . 53
4.3 Thermal model . . . 65
4.3.1 Determination of surface temperature on slopes . . . 65
4.3.2 Subsurface temperature . . . 68
4.4 Transport of gases in porous media . . . 71
4.4.1 Mass transfer versus mass transport . . . 71
4.4.2 Mechanisms of gas transport . . . 72
4.4.3 Advective flux . . . 73
4.4.4 Molecular diffusive flux . . . 74
4.4.5 Bulk diffusive flux . . . 75
4.4.6 Knudsen diffusive flux . . . 75
4.4.7 Effective diffusion coefficient . . . 76
4.4.8 Adsorption . . . 77
4.4.9 Gas transport models . . . 78
4.5 Summary . . . 83

5 Methane clathrate stability and composition on Mars **85**
5.1 Methane clathrate stability zone: a sensitivity study . . . 86
5.1.1 Subsurface pressure . . . 86
5.1.2 Subsurface composition . . . 87
5.1.3 Heat flow . . . 89
5.1.4 Presence of magnesium perchlorate . . . 89
5.1.5 Initial gas phase . . . 92
5.1.6 Sloping surface . . . 92
5.2 Methane clathrate stability zone: Global maps . . . 96
5.3 Variability of methane trapping . . . 100
5.4 Variation of clathrate stability zone in the past . . . 103
5.5 Summary . . . 107

6 Transport of CH_4 and H_2O gases in the martian soil **109**
6.1 Water vapor diffusion and ice stability . . . 111
6.1.1 Ice stability key parameters . . . 112
6.1.2 Ice stability at selected locations . . . 119
6.2 Methane outgassing scenarios . . . 124
6.2.1 Coupling with atmospheric models . . . 129
6.3 Summary . . . 133

7 Conclusions and perspectives **135**

A Calculation of the fugacity **143**

B Crank-Nicolson scheme **149**

Bibliography **153**

Chapter 1

Introduction

Many processes on Mars have yet to be understood, and the series of methane (CH_4) detection and non-detection in the atmosphere of the planet over the last two decades has raised numerous questions about methane generation and destruction mechanisms, which still remain unexplained. Several detections have been reported from Earth-based and Mars orbit instruments (Formisano et al., 2004; Krasnopolsky et al., 2004; Geminale et al., 2008, 2011; Mumma et al., 2009; Fonti and Marzo, 2010) with abundances ranging up to tens of parts per billion by volume (ppbv), while in-situ measurements performed by the Mars Science Laboratory (MSL) rover at Gale crater showed some peaks up to ~ 7 ppbv and strong seasonal variations of CH_4 background levels (Webster et al., 2015, 2018). Recently and for the first time, an in-situ spike detection has been confirmed from orbit by the Mars Express team who reanalyzed data recorded in 2013 (Giuranna et al., 2019). The first measurements from the ExoMars Trace Gas Orbiter mission, dedicated in particular to the study of methane and other trace gases, have been newly published (Korablev et al., 2019) and show the non-detection of martian methane with an upper limit 10 to 100 times lower than previously reported positive detections (Mumma et al., 2009; Webster et al., 2018).

The detection of methane on Mars was unexpected, given its relatively short lifetime of 300-600 terrestrial years predicted by photochemistry. Its presence in the martian atmosphere implies therefore the existence of a subsurface reservoir or an active primary source. Even more suprising is the spatial and temporal heterogeneity of CH_4, evidenced by both remote-sensing and in-situ observations, which considerably challenges our current understanding of atmospheric chemistry and physics on Mars. Indeed, the rapid variations in methane concentration observed in the planet's atmosphere (detections followed by non-detections) result in a much shorter CH_4 lifetime than mentioned above and imply strong

destruction mechanisms acting about 600 times faster than photochemistry (Lefèvre and Forget, 2009). In addition, methane being potentially related to present or past life, the search for this gas and the investigation about the still unidentified but probably subterranean CH_4 source(s) remain a major goal of present and future Mars missions.

It has been suggested that methane on Mars could originate from biological (Atreya et al., 2007; Weiss et al., 2000), geological (Oze and Sharma, 2005; Etiope and Sherwood Lollar, 2013) or exogenous (Kress and McKay, 2004; Keppler et al., 2012) production mechanisms. On the other hand, ancient CH_4 could be stored in subsurface reservoirs such as clathrate hydrates (Chastain and Chevrier, 2007). Their destabilization stimulated by pressure and temperature changes could be the source of the recent observations of martian methane. Clathrate hydrates or clathrates are crystalline compounds formed by water and gas in low temperature and high pressure conditions and capable of trapping a large amount of methane. Indeed, at standard pressure and temperature (STP) conditions, one cubic meter of CH_4 clathrates contains more than 160 cubic meters of methane. Clathrate hydrates have been discovered incidentally in 1810 during low-temperature experiments on liquid water and dichlorine gas (Davy, 1811) but were not believed to occur in nature at that time. It is only in the early sixties that clathrates were proposed to exist in other Solar System bodies (Miller, 1961), a few years before their discovery in the terrestrial permafrost (Makogon, 1965). More than 130 compounds, including methane, are known to be clathrate hydrate formers (Sloan and Koh, 2007). Wherever thermodynamic stability conditions are met and gas and water are available, clathrates can form. These compounds appear to be omnipresent in nature (permafrost, marine sediments) and methane accounts for 99% of their total amount of gas (Sloan and Koh, 2007). By only considering continental clathrates, Klauda and Sandler (2005) estimated a total amount of trapped gas of 4.4×10^{16} m^3 (STP). On Mars, a clathrate reservoir less than 2×10^3 to 2×10^7 m^3 that would dissociate each year would explain the reported atmospheric methane levels (Elwood Madden et al., 2007).

Although the knowledge about the occurrence of clathrate hydrates on Earth is growing from year to year, the detailed global clathrate inventory is still very incomplete (Sloan and Koh, 2007). On Mars, clathrate global distribution is expected to be at least as complex as on Earth (Lasue et al., 2015). The formation/dissociation cycle of clathrates and the thickness of their stability zone depend on many factors such as subsurface composition, local heat flow, salinity of the water involved in the clathrate formation (Elwood Madden et al., 2007) and climate change due to seasonal and obliquity variations (Prieto-Ballesteros et al.,

2006; Root and Elwood Madden, 2012). This thesis work results from the need to provide a better estimation of the subsurface distribution of clathrates on Mars and to evaluate them as a potential source for martian methane. Moreover, while many studies have focused on atmospheric modeling of methane by considering instantaneous or sustained surface emissions with a constant release rate (Lefèvre and Forget, 2009; Mischna et al., 2011; Holmes et al., 2015; Viscardy et al., 2016), models of methane transport in the subsurface constraining the intensity, variation and duration of the surface flux are still sparse (Stevens et al., 2015, 2017; Moores et al., 2019). Both types of study need to be conducted together with the investigation of potential CH_4 sinks in order to efficiently interpret methane observations. For this purpose, we have developed a diffusive-adsorptive model of gas transport, for which the CH_4 source depths are constrained by the estimated stability zone of clathrate hydrates on Mars.

This manuscript is organized as follows. In order to have a better picture of the methane enigma on Mars, the Chapter 2 is dedicated to the review of all methane observations (remote sensing and in-situ measurements) made to date and their comparison. The various proposed generation and loss methane processes as well as the potential subsurface reservoirs are also discussed. Chapter 3 addresses the properties and structures of clathrates, which will be useful to model methane trapping. The clathrate stability zone, which is investigated for Mars later in the manuscript, is defined in this chapter as well. The different models used and developed are presented in Chapter 4, which is divided into two major parts. One is dedicated to the study of methane clathrate stability and composition and the second one elaborates on the diffusive gas transport in the porous martian regolith. The results that apply to these two parts are shown in Chapter 5 and Chapter 6, respectively. Finally, conclusions and perspectives are exposed in the last chapter.

Chapter 2

Methane on Mars

Contents

2.1 Observations of martian methane 6
2.2 Theoretical objections 14
2.3 Methane generation mechanisms on Mars . . 16
2.3.1 Biological origin 17
2.3.2 Geologic production 19
2.3.3 Meteoritic and cometary source 22
2.3.4 Photochemical production 24
2.4 Methane subsurface reservoirs on Mars . . . 25
2.5 Methane loss mechanisms on Mars 27
2.6 Current and future missions 30
2.7 Summary 31

The discovery of methane on Mars is a very fascinating subject because it could possibly be related to past or present life. On the other hand, Mars could be more geologically active than we thought. Nowadays, martian methane remains surrounded by a lot of mystery as its source and sink are unknown. Indeed, its observed spatial and temporal variations challenge our current understanding of atmospheric chemistry and physics and as a result its presence on the Red Planet is still debated today.

In the coming months/years, the ExoMars Trace Gas Orbiter, currently in orbit around Mars, will provide new CH_4 data. This mission, launched in 2016 and specially designed to detect methane and other trace gases, will help to definitely demonstrate the presence or absence of martian methane and may shed light on mechanisms of methane production and destruction.

In this chapter, we review the different methane observations made to date, the various proposed generation and loss processes as well as

potential subsurface reservoirs such as clathrate hydrates. These compounds are of great interest because they could have stored over long time period methane related to a past era of Mars.

2.1 Observations of martian methane

The measurements used to highlight the presence of methane in the atmosphere of Mars were made from Earth, space and in situ. Ground-based observations are made difficult by the presence of Earth's atmosphere, ~ 60 times thicker than that of Mars and containing ~ 1800 ppbv methane. These observations exploit the Doppler effect where martian lines are displaced from the center of the corresponding terrestrial lines when Mars is approaching or moving away from the Earth. For example, the Doppler shift for a relative velocity of 17 km/s is 0.17 cm^{-1} at 3000 cm^{-1} (Zahnle et al., 2011). The choice of the observing site is important: its elevation must be sufficiently high to reduce the abundance of telluric methane as well as the width of CH_4 absorption lines, proportional to the local atmospheric pressure. Observations from space do not suffer from telluric contamination but both spectral resolution and signal-to-noise ratio of the instruments used are usually rather low. To study methane from space-based instruments, a few thousands spectra are thus summed for each measurement.

The first claim of methane presence in the martian atmosphere was made in 1969 based on the data recorded by the Mariner 7 infrared spectrometer. However, the strong absorption features detected have been misinterpreted and can be associated to CO_2 ice (Herr and Pimentel, 1969). Several attempts have been made afterwards to observe methane on Mars using the Mariner 9 Infrared Interferometer Spectrometer (IRIS) (Maguire, 1977) and the Short-Wavelength Spectrometer of the Infrared Space Observatory (ISO) (Lellouch et al., 2000), yielding upper limits of 20 and 50 parts per billion by volume (ppbv) respectively. Between these two attempts with space-based instruments, observations were conducted in 1988 by Krasnopolsky et al. (1997) using the 4-m telescope and Fourier transform spectrometer (FTS) at the Kitt Peak National Observatory in Arizona. This tentative detection of martian methane suggested a mixing ratio of 70 ± 50 ppbv, marginally consistent with the previous measurements from Mariner 9.

It is only in the early 2000s that positive detections have been announced. Indeed, in 2004, three teams independently reported the identification of methane in the martian atmosphere using Earth-based and Mars orbit instruments (Krasnopolsky et al., 2004; Formisano et al.,

2004; Mumma et al., 2004). Krasnopolsky et al. (2004) used the Fourier Transform Spectrometer (FTS) at the Canada-France-Hawaii Telescope located in Mauna Kea (altitude of ∼4 km), Hawaii. The spectral resolution of the instrument is about 0.02 cm^{-1} at 3000 cm^{-1} with a resolving power $\lambda/\Delta\lambda \sim 180{,}000$. The observations were made in January 1999 focusing on the strong methane absorption band at 3018 cm^{-1} and showed a global CH_4 mixing ratio of 10 ± 3 ppbv. Assuming this amount represents a steady-state value (the CH_4 mass injected into the atmosphere balances the integrated loss over the martian year) and using an estimated photochemical lifetime of methane of 340 Earth years, Krasnopolsky et al. (2004) calculated a global CH_4 flux at the martian surface of 270 tonnes per year.

A global average methane mixing ratio similar to Krasnopolsky et al. (2004) was found by Formisano et al. (2004), who observed Mars in January, February and May 2004 using the Planetary Fourier Spectrometer (PFS) onboard the Mars Express spacecraft. The PFS data do not suffer from telluric contamination, but the spectral resolution is quite low (1.3 cm^{-1}). Therefore, Formisano et al. (2004) focused as well on the strong methane spectral band centered at 3018 cm^{-1} given that the signal-to-noise ratio of the PFS instrument is much greater in that region. This team evidenced a non-uniform CH_4 distribution in the atmosphere with mixing ratios varying between 0 and 30 ppbv and decreasing from eastern to western longitudes. These spatial variations were surprizing given that methane was expected to be well-mixed in the martian atmosphere (Krasnopolsky et al., 2004). Indeed, the CH_4 lifetime predicted by standard photochemical models (300-600 terrestrial years) is significantly larger than both vertical and horizontal mixing times (10 days and 0.5 year respectively). The observed variations in CH_4 concentration therefore suggested the presence of localized active sources and/or sinks.

The third CH_4 detection reported in 2004 was by Mumma et al. (2004) at the annual meeting of the Division for Planetary Sciences (DPS) of the American Astronomical Society. Methane absorption lines at 3029 and 3039 cm^{-1} were searched using the ground-based high-resolution spectrometers CSHELL (Cryogenic Echelle Spectrograph) of the NASA Infrared Telescope Facility and NIRSPEC (Near Infrared Spectrograph) of the Keck II Telescope, both located in Mauna Kea. A third instrument was also used, Phoenix of the Gemini South Telescope in Chile, but suffered from internal scattered light. Therefore, Phoenix data have not been published and the authors have deferred discussion related to the measurements of this instrument. The observations performed by Mumma et al. (2004) in January and March 2003, times corresponding to summer in the martian northern hemisphere, evidenced

localized spots with methane levels as high as 250 ppbv. However, the maximum local concentration had been revised down by a factor 5 in the corresponding work published in 2009, in which observations performed in 2006 are analysed as well. Mumma et al. (2009) reported local CH_4 mixing ratios up to 45 ppbv measured in March 2003 with localized enriched regions including Terra Sabae (0°, 50°E), Nili Fossae (22°N, 75°E) and Syrtis Major (8°N, 70°E). These regions are consistent with the areas of high methane abundance reported by Formisano et al. (2004). Mumma et al. (2009) estimated that the methane plumes observed during northern summer 2003, if spread uniformly over the planet, would generate a global average mixing ratio of 6 ppbv. In June 2003, Encrenaz et al. (2005) were unable to detect methane using as well the NASA IRTF and found upper limits consistent with earlier reports. However, the region with the strongest CH_4 plumes observed by Mumma et al. (2004, 2009) was not in the field of view at that period. Three years later in the early martian spring (February 2006), the mean mixing ratio observed by Mumma et al. (2009) decreased to only 3 ppbv. This value is in agreement with the methane abundance observed at the same time period by Krasnopolsky (2012) using the IRTF/CSHELL (at 3029 and 3039 cm^{-1}). Indeed, the analysis of the measurements gave a CH_4 level of ∼3 ppbv outside the Valles Marineris region, where a positive detection of ∼10 ppbv was made. However, this last claim is quite puzzling given that Villanueva et al. (2013) did not detect any methane (at 2999 cm^{-1}) over Valles Marineris just 28 days before the detection made by Krasnopolsky (2012). The observed variations of the methane mixing ratio from 2003 to 2006 implies the existence of an unknown destruction process much more efficient than standard photochemistry. As a result, the CH_4 lifetime in the martian atmosphere could be as short as 0.6 Earth years (Mumma et al., 2009).

Geminale et al. (2008, 2011) kept working on PFS data and confirmed the spatial variations of CH_4 in the martian atmosphere through the analysis of averaged spectra obtained from 2004 to 2009. Over this time period and investigated regions, the mean methane mixing ratio was 15 ppbv. In addition, CH_4 seasonal behaviour was studied and the methane mixing ratio variations seemed to indicate a maximum during northern spring and a minimum in northern winter. Maps of CH_4 column density for each season were obtained by averaging data over the entire period of observations. Enriched regions of methane were located southward the equator during northern spring, at high northern and southern latitudes during the northern summer (maximum CH_4 mixing ratio of 45 ppbv above the north polar cap) and northward the equator during the northern fall and winter. Geminale et al. (2011) explained this increase

of methane abundance during local winter by the global circulation that transports non-condensable gases such as methane towards regions where CO_2 is condensing. This phenomenon was indeed predicted by numerical simulations with a general circulation model (GCM) for Mars (Lefèvre and Forget, 2009). However, the methane peak over the north pole when ice is sublimating during local summer cannot be explained by global circulation. Geminale et al. (2011) suggested therefore that the north polar cap could be associated with methane reservoirs. They also reported a correlation between water vapour and methane, the latter seeming to follow the diurnal cycle of H_2O. This association between H_2O and CH_4 was as well pointed out by Mumma et al. (2009).

In addition to PFS, another space-based instrument was used to observe methane in the martian atmosphere. Indeed, data collected by TES (Thermal Emission Spectrometer) onboard Mars Global Surveyor (MGS) were analysed by Fonti and Marzo (2010) using a statistical clustering technique. They searched the CH_4 absorption band at 1306 cm^{-1} by averaging a few thousand spectra taken over three martian years (1999-2005). This fourth independent positive detection revealed the presence of three broad regions enriched in methane: Tharsis, Elysium and Arabia Terra. These locations are expected to harbor favourable geological conditions such as residual geothermal activity for the first two sites and strong hydration for the third one. The CH_4 abundance observed by TES was the highest ($\geq$ 60 ppbv) in the Tharsis region with an apparent decrease from west to east, in opposition with the geographical trend deduced from PFS data (Formisano et al., 2004). On the other hand, the Arabia Terra area corresponds to the methane-rich region observed by Mumma et al. (2009). In addition, the analysis performed by Fonti and Marzo (2010) suggested that the CH_4 spatial distribution follows a seasonal cycle but also varies from one year to another. The global average mixing ratio ranged from 5 $\pm$ 1 to 33 $\pm$ 9 ppbv with a peak during northern summer and autumn followed by a sharp decrease in winter. This trend is relatively similar to what Geminale et al. (2008) observed except for the sudden decline during winter. Fonti et al. (2015) carefully revisited their previous results and their statistical analysis of TES spectra and were not able to either confirm or refute the temporal and spatial variability of methane.

Aoki et al. (2018) performed measurements to detect CH_4 in the martian atmosphere at 1326-1338 cm^{-1} using the Echelon-Cross-Echelle Spectrograph (EXES) onboard the Stratospheric Observatory for Infrared Astronomy (SOFIA). Due to the high altitude of SOFIA ($\sim$13.7 km), the effects of terrestrial atmosphere are notably diminished, which gives access to CH_4 lines that are otherwise buried in the strong absorp-

tion of terrestrial methane when measurements are made from ground-based instruments. The observations with the EXES spectrograph were carried out in March 2016, which corresponds to northern summer on Mars. Despite the strong accuracy of the SOFIA facility, Aoki et al. (2018) were not able to unambiguously detect methane, upper limits ranging from 1 to 9 ppbv.

Recently, first results from Trace Gas Orbiter covering an observation period from April to August 2018 did not show any methane detection in the martian atmosphere and found an upper limit of about 0.05 ppbv (Korablev et al., 2019).

The global CH_4 mixing ratio reported during all these remote-sensing observations is represented in Fig. 2.1 as a function of solar longitude L_s. These methane levels were not measured the same martian year (see Table 2.1) and are averaged when data cover several seasonal cycles. The black and grey lines have been obtained by averaging the data in each of the following groups: $L_s = 0° \pm 45°$, $90° \pm 45°$, $180° \pm 45°$, $270° \pm 45°$. The trend of these data sets seems to indicate a maximum methane content during northern spring and summer ($0° \leq L_s \leq 180°$) and a minimum during northern winter ($270° \leq L_s \leq 360°$). All the data sets show a similar pattern with an increase of the methane mixing ratio during northern spring and summer except for the measurements of Geminale et al. (2011) which peak at the beginning of northern spring and subsequently decrease to reach a minimum value during winter.

Despite some inconsistencies, reported CH_4 detections are generally in agreement regarding the spatial and temporal variations of methane abundance.Remote-sensing observations suggest that methane release in the martian atmosphere could be a rare or intermittent process although orbital data from PFS and TES support a more regular behavior with latitudinal, seasonal and interannual variabilities. Accordingly, the CH_4 measurements announced during these last 15 years could indicate one or few outgassing events spanning several years, but varying in intensity depending on seasonally controlled surface conditions.

In addition to the observations from Earth and Mars orbiters, methane has been searched in-situ by the Tunable Laser Spectrometer (TLS) of the Sample Analysis at Mars (SAM) instrument suite on Curiosity rover operating since 2012 (Webster et al., 2013, 2015, 2018). The TLS instrument has a spectral resolution ($0.0002\ cm^{-1}$) far better than the previous spectrometers used to detect methane on Mars (Webster et al., 2013), but unlike former measurements that gave the column-integrated CH_4 concentration, Curiosity can only sample the near-surface atmosphere ($\sim$1 m) at its landing site, Gale crater (-4.6°N, 137.4°E). Two methods of atmospheric ingestion are used by TLS-SAM (Webster et al., 2018).

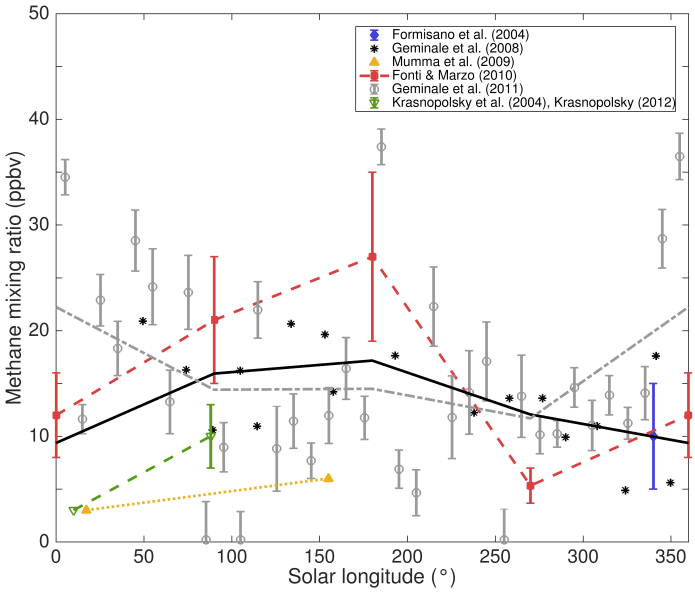

Figure 2.1: Observed seasonal variations of the global CH_4 mixing ratio in the martian atmosphere from remote-sensing measurements. Methane concentrations were not observed the same martian year and are averaged when data cover several seasonal cycles.

In the first referred as direct ingest method, the gas is delivered to the evacuated sample cell through an inlet port located on the side of the Curiosity rover. This procedure, where the cell needs ∼20 min to be filled to ∼7 mbar, produces uncertainties of ∼2 ppbv for each measurement. The second, that allows more precise measurements of low background levels, is an enrichment method where atmospheric gas is transported through a second inlet port, flowing slowly over a carbon dioxide scrubber material. The latter procedure, which lasts ∼2 hours, efficiently removes incoming CO_2 and effectively enriches the methane abundance by a factor of ∼25.

Webster et al. (2013) first reported the non-detection of methane with an upper limit of 1.3 ppbv for observations performed in October and November 2012, and in June 2013. Subsequent observations over a 20-month period showed CH_4 background levels with a mean value of 0.69 ± 0.25 ppbv and sporadic elevated levels up to ~ 7.2 ppbv, implying that methane is episodically released in the atmosphere of Mars (Webster et al., 2015). Recently, Webster et al. (2018) reported strong seasonal variations of CH_4 background levels which reach a maximum at the end of the northern summer. The measurements covering now a 5-Earth

year (or almost 3-Mars year) period are represented in Fig. 2.2. The average mixing ratio of CH_4 background levels determined using these new observations is 0.41 ± 0.16 ppbv. Moreover, the improved analysis of Webster et al. (2018) produced a mean value for the occasional methane spikes of ∼7.6 ppbv, an amount slightly higher than previously reported (Webster et al., 2015).

In addition, an in-situ measurement has been independently confirmed from orbit by Giuranna et al. (2019) who reanalyzed data recorded by Mars Express in June 2013 and found a methane concentration of 15.5 ppbv above Gale crater shortly after a CH_4 spike was observed by Curiosity.

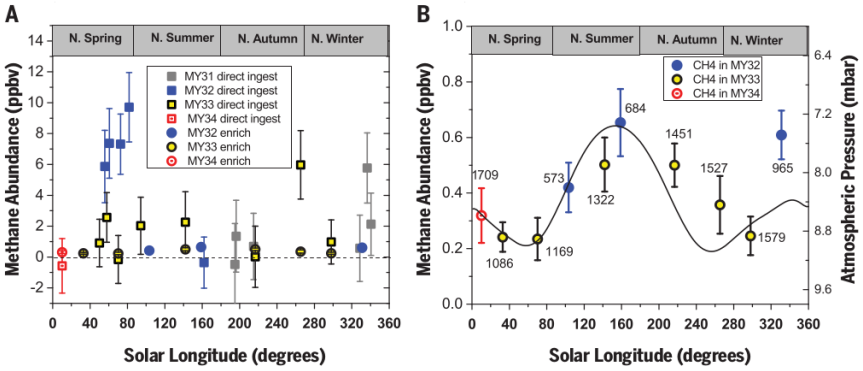

Figure 2.2: The TLS-SAM methane measurements as a function of solar longitude (Webster et al., 2018). (A) Measurements from direct ingests (squares) and enrichment ingests (circles with smaller error bars). A CH_4 spike up to ∼7 ppbv occurred during observations conducted the first martian year. (B) Background measurements show strong seasonal variation. The solid line represents the mean values over the 3 Mars years of atmospheric pressure recorded by REMS (Rover Environmental Monitoring Station) instrument.

Both remote-sensing and in-situ observations seem to indicate that methane release in the martian atmosphere is a sporadic and/or localized process. Plausible correlations of the background CH_4 values with surface temperatures and atmospheric water vapour suggest that methane discharge could be associated to microseepage release, or physical/chemical processes taking place on dust or at the surface (Webster et al., 2018).

Table 2.1: Summary of detections and non-detections of methane in the martian atmosphere.

Instrument	**Wavenumber (cm^{-1})**	**Period of observations**	**Mixing ratio (ppbv)**	**Ref.**
IRIS[1] (Mariner 9)	1306	1971-1972	≤ 20	(a)
FTS[2] (Kitt Peak)	2650-2800, 1229-1237	06/1988	70 ± 50	(b)
ISO[3]	3018	07/1997	≤ 50	(c)
FTS (CFHT[4])	3018	01/1999	10 ± 3	(d)
PFS[5] (Mars Express)	3018	01-02/2004, 05/2004	10 ± 5 (global) 30 (local max)	(e)
TEXES[6] (IRTF[7])	1230-1236, 1237-1244	06/2003	≤ 20 (morning side) ≤ 70 (evening side)	(f)
CSHELL[8] (IRTF)/ NIRSPEC[9] (Keck II)	3029, 3039	01/2003, 03/2003	45 (local max) 6 (global)	(g)
CSHELL (IRTF)/ NIRSPEC (Keck II)	3029, 3039	02/2006	≤ 3	(g)
TES[10] (MGS)[11]	1306	1999-2005	5-33	(h)
PFS (Mars Express)	3018	2004-2009	15 (global) 45 (local)	(i)
CSHELL (IRTF)	3029, 3039	02/2006	$\sim$10 (local) $\sim$3 (elsewhere)	(j)
CSHELL (IRTF)	3029, 3039	12/2009	≤ 8	(j)
CSHELL (IRTF)/ NIRSPEC (Keck II)	2999	01/2006 11/2009 04/2010	≤ 7.8 ≤ 6.6 ≤ 7.2	(k)
TLS[12] (Curiosity)	3057	10-11/2012, 06/2013	≤ 1.3	(l)
TLS (Curiosity)	3057	2012-2014	0.69 ± 0.25 (background) 7.2 ± 2.1 (peak)	(m)
EXES[13] (SOFIA[14])	1326-1338	03/2016	$\leq$ 1-9	(n)
TLS (Curiosity)	3057	2012-2017	0.41 ± 0.16 (background) 7.6 ± 1.6 (peak)	(o)
PFS	3018	06/2013	15.5 ± 2.5 (local)	(p)
NOMAD[15]/ACS[16] (Trace Gas Orbiter)	3023-3066	04-08/2018	≤ 0.05	(q)

(a) Maguire (1977)
(b) Krasnopolsky et al. (1997)
(c) Lellouch et al. (2000)
(d) Krasnopolsky et al. (2004)
(e) Formisano et al. (2004)
(f) Encrenaz et al. (2005)
(g) Mumma et al. (2009)
(h) Fonti and Marzo (2010)
(i) Geminale et al. (2011)
(j) Krasnopolsky (2012)
(k) Villanueva et al. (2013)
(l) Webster et al. (2013)
(m) Webster et al. (2015)
(n) Aoki et al. (2018)
(o) Webster et al. (2018)
(p) Giuranna et al. (2019), (q) Korablev et al. (2019)

[1] Infrared Interferometer Spectrometer
[2] Fourier Transform Spectrometer
[3] Infrared Space Observatory
[4] Canada-France-Hawaii Telescope
[5] Planetary Fourier Spectrometer
[6] Texas Echelon Cross Echelle Spectrograph
[7] NASA Infrared Telescope Facility
[8] Cryogenic Echelle Spectrograph
[9] Near Infrared Spectrograph
[10] Thermal Emission Spectrometer
[11] Mars Global Surveyor
[12] Tunable Laser Spectrometer
[13] Echelon-Cross-Echelle Spectrograph
[14] Stratospheric Observatory for Infrared Astronomy
[15] Nadir and Occultation for MArs Discovery
[16] Atmospheric Chemistry Suite

2.2 Theoretical objections

Reported observations of methane in the martian atmosphere are broadly consistent regarding the CH_4 spatial and temporal variations. In total, five independent teams searching for at least five different absorption features and using six instruments (three Earth-based, two in Mars-orbit and one in-situ) have detected methane on Mars. Although its presence on the Red Planet was unexpected, methane variability on short time scales turned out to be more surprising and questioned. Indeed, the CH_4 lifetime required to fit published detections is about 600 times shorter than the one predicted by standard atmospheric photochemistry models (Lefèvre and Forget, 2009). Theoretical and technical objections were thus raised about the spectroscopic interpretations implying the presence of CH_4 on Mars (Zahnle et al., 2011; Zahnle, 2015).

In general, measurements from space-based instruments are criticized due to their weak spectral resolution, which makes methane detection very challenging. Villanueva et al. (2013) suggested that those measurements may be affected by micro-vibrations or unrecognized solar/water signatures dominating the spectral regions used for methane identification. Zahnle et al. (2011) questioned the MGS-TES analysis performed by Fonti and Marzo (2010) claiming that the methane detection made depends on spatial and seasonal correlations with observations from Geminale et al. (2008) and Mumma et al. (2009). Indeed, due to the low resolution of TES data and the presence of nearby H_2O and CO_2 lines, the association of the spectral feature observed at 1306 cm^{-1} with methane is not singular according to Zahnle et al. (2011). However, before to positively identify methane, Fonti and Marzo (2010) explicitly investigated each possible contribution to this spectral region from other martian species such as CO_2 and H_2O using a radiative transfer model with a complete atmospheric and surface description. This latter method was not commented by Zahnle et al. (2011). Regarding PFS data, Zahnle et al. (2011) observed that methane presence was inferred indirectly by Formisano et al. (2004) and Geminale et al. (2008) who fitted their spectra model to PFS observations at 3018 cm^{-1} by adding 10-60 ppbv CH_4. They noted in addition that the width of the methane absorption feature between predictions and measurements did not match. However, Zahnle et al. (2011) offered no alternative way to explain this feature at this wavenumber without methane.

Ground-based observations are more criticized by Zahnle et al. (2011) because of interference by Earth's atmosphere along the line of sight. In addition, Zahnle et al. (2011) suggested that measurements from Krasnopolsky et al. (2004) may be misinterpreted also due to the pre-

sence of martian CO_2 lines that would prevent to detect small amounts of methane and that the assumed CH_4 absorption feature could be associated to instrumental artifacts. Although observations from Mumma et al. (2009) show much stronger signals than those of Krasnopolsky et al. (2004), Zahnle et al. (2011) questioned them in more details suggesting that blue-shifted retrievals were distorted due to contamination by telluric $^{13}CH_4$ lines, much stronger than the martian $^{12}CH_4$ lines. Indeed, when Mumma et al. (2009) observed methane plumes in 2003, telluric $^{13}CH_4$ lines superposed on the blue wings of the telluric $^{12}CH_4$ lines at 3029 and 3039 cm^{-1} preventing to identify blue-shifted martian $^{12}CH_4$ lines without appropriate corrections. This possible misinterpretation could explain why Mumma et al. (2009) did not detect significant amounts of methane using the same spectral lines when the martian spectrum was red-shifted three years later. Actually, Zahnle et al. (2011) suggested that the atmospheric model used by Mumma et al. (2009) as the basis to subtract Earth's spectral absorptions assumed a ^{13}C isotopic abundance slightly higher than the actual value. As a consequence, this treatment would have introduced emission (not absorption) at the wavelengths of the telluric $^{13}CH_4$ lines reducing therefore the martian methane signal. However, such emissions did not appear on the blue wing of telluric $^{12}CH_4$ when Mars was red-shifted in 2006. Villanueva et al. (2013) used this argument to evidence that telluric $^{13}CH_4$ was thus properly removed while Zahnle et al. (2011) proposed that Mumma et al. (2009) underestimated martian $^{13}CH_4$ and that their retrieval uncertainty was similar to the claimed methane signal. The detection of the CH_4 doublet at 2999 cm^{-1} performed by Mumma et al. (2009) in May 2005 (Fig. S2 from their supporting online material) was also questioned by Zahnle et al. (2011) due to interference with temperature-sensitive telluric water lines. This leads to the same type of problem as previously mentioned for $^{13}CH_4$, especially since terrestrial contamination at these specific wavelengths, where methane detections are claimed, is particularly undocumented (Zahnle et al., 2011). Nevertheless, using the same method at the same wavenumber (2999 cm^{-1}), Villanueva et al. (2013) unsuccessfully searched for methane on Mars in January 2006, which seems surprising if the previous detection was wrongly attributed to CH_4 due to improper corrections of telluric H_2O lines.

In-situ identification by the TLS-SAM experiment was also contested by Zahnle (2015) arguing that the methane detected comes from the rover itself. However, Webster et al. (2018) stated that there was no identified source large enough to sustain the random spikes during the observed 2-month period of high CH_4 levels or even to produce an instantaneous CH_4 cloud of $\sim$7 ppbv around the rover. Although some residual terrestrial

methane is present in the rover chamber, this amount is too small to serve as a bulk source in the ingestion experiments (Webster et al., 2018). In addition, this residual methane is taken into account in martian CH_4 detections by subtracting the signal obtained when the cell is empty from each measurement with martian air filling the cell. Finally, no sign of gross leakage from the rover chamber was observed during the 5-Earth year period of the mission (Webster et al., 2018).

2.3 Methane generation mechanisms on Mars

The origin of methane on Mars is still unknown and can be related to subsurface or exogenous processes, some of them being presented in Fig. 2.3. Methane could be potentially linked to life, it would then be referred as biotic CH_4 and would derive from past or present microbes (methanogens) or thermogenic degradation of organic matter. In contrast, abiotic CH_4 could be produced by geochemical processes, such as low temperature Sabatier reaction (Etiope and Sherwood Lollar, 2013) or volcanic degassing, or by thermal degradation of abiotic organics (Oehler and Etiope, 2017). In this section, we review all the proposed production and destruction mechanisms of methane on Mars.

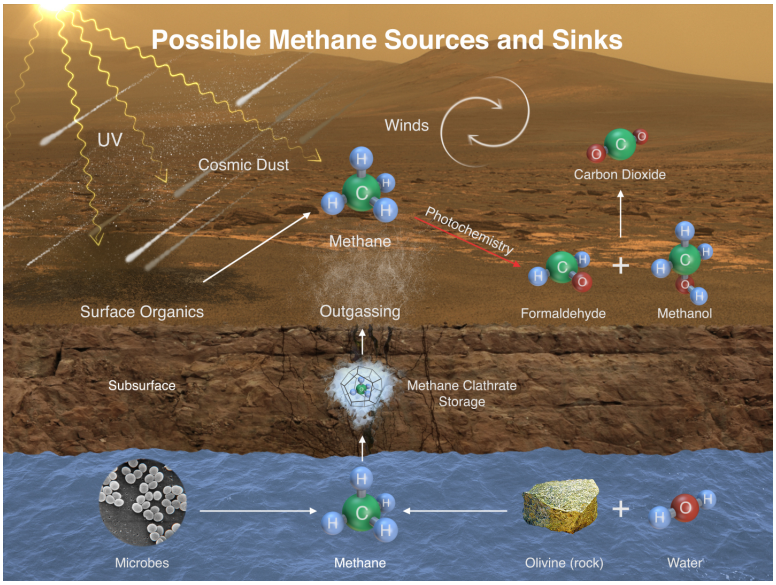

Figure 2.3: Possible sources and sinks of methane on Mars. Credits: NASA.

2.3.1 Biological origin

On Earth, methane is mainly produced by biological activity (90-95%). One can therefore wonder if modern or extinct microbial colonies are responsible for the presence of methane on Mars. Given the particularly inhospitable conditions for life at the planet's surface (extremely low temperatures and dessicated conditions, CO_2 atmosphere, high levels of radiation), living organisms, if currently present on Mars, would rather be located in the subsurface. Candidate sources could be methanogenic microbes that are known to exist in extreme terrestrial environments harboring conditions similar to those expected on present-day Mars. These organisms produce methane and require liquid water as well as a source of H_2 and carbon such as CO or CO_2 although CO is energetically more advantageous (Zahnle et al., 2011). The chemical reactions involved are as follows:

$$4\ CO + 2\ H_2O \rightarrow CH_4 + 3\ CO_2 \tag{2.1}$$

$$4\ H_2 + CO_2 \rightarrow CH_4 + 2\ H_2O \tag{2.2}$$

The temperature of methanogenic habitats should be at least 0°C, which occurs at depths from 150 m to 8 km, depending of the soil thermal conductivity and the local heat flow (Tung et al., 2005). Microbial colonies could thus exist in the subpermafrost aquifers on Mars (Atreya et al., 2007) but the habitable niches would be constrained by the availability of H_2 and CO/CO_2 necessary for autotrophic[1] methanogenesis. Carbon dioxide is abundant in the martian atmosphere and cryosphere, while CO and H_2 atmospheric mixing ratios are equal to ∼700 ppmv and 40 ± 10 ppmv respectively (Atreya and Gu, 1995; Krasnopolsky, 1993; Nair et al., 1994). These gases are expected to diffuse down through the subsurface to supply the methanogens. However, the diffusion time of these species through the soil is quite long and they may be lost during this period where they are in contact with oxidizing minerals (Krasnopolsky et al., 2004). As a consequence, the thickness of the biotic layer would be limited to the top few hundred meters of the martian subsurface (Weiss et al., 2000). On the other hand, microbes could also use gases derived from hydrothermal systems, which would extend the habitable layer deeper in the crust. Indeed, H_2 may be locally available via processes such as serpentinization (Oze and Sharma, 2005).

Although not excluded, a biological methane source is puzzling because atmospheric CO levels, that would have been depleted due to con-

[1] Related to an organism able to synthesize its own food using energy from light or inorganic chemical reactions

sumption by methanogens, remain abundant on Mars (Zahnle et al., 2011). As a result, life could be restricted to subsurface pockets located several kilometers deep where liquid water is available and the atmospheric gas fluxes very low (Weiss et al., 2000). Another possibility is that methane could have been generated by ancient living organisms in the past of the planet and subsequently trapped in subsurface reservoirs. The current destabilization of these reservoirs could thus release methane in the martian atmosphere. Alternatively, possible remains of this past microbial life could be degraded due to high temperatures related to burial, magmatic heating, hydrothermal systems, and impacts, leading thereby to methane production (Oehler and Etiope, 2017).

Useful information regarding the methane origin, biotic or abiotic, can be obtained by measuring combined CH_4 isotope-isotopologue and ethane data (Etiope, 2018). On Earth, the ratio between the two stable carbon isotopes, ^{13}C and ^{12}C, is conventionally expressed as $\delta^{13}C$ relative to the standard VPDB (Vienna Pee Dee Belemnite standard):

$$\delta^{13}C = \left(\frac{\left(\frac{^{13}C}{^{12}C}\right)_{\text{sample}}}{\left(\frac{^{13}C}{^{12}C}\right)_{\text{standard}}} - 1 \right) \times 1000‰ \tag{2.3}$$

Typically, low values of $\delta^{13}C$ (< -50‰, ^{12}C-enriched CH_4) are related to microbial activity, while high values (> -50‰, ^{13}C-enriched CH_4) are often attributed to abiotic gas. Similarly, hydrogen isotopic composition (D/H ratio) of methane could be examined in addition to the $^{13}C/^{12}C$ ratio to provide supplementary information and thus a better identification of the CH_4 origin (Webster and Mahaffy, 2011; Etiope, 2018). An alternative test to determine if martian methane could be associated to life is the measurement of methane/ethane ratio. Indeed, trace amounts of C_2H_6 can be produced by microbes and high CH_4/C_2H_6 ratios (>1000) are generally related to biological sources (Etiope, 2018). However, the problem is not that simple and the interpretation of all these data could be laborious given that methane of different origins may have comparable $^{13}C/^{12}C$ or CH_4/C_2H_6 ratios. For instance, the carbon isotopic composition of methane produced by photodegradation of abiotic organic material in Mars-like surface conditions is similar to that of terrestrial microbial origin (Keppler et al., 2012). Moreover, the original CH_4 isotopic composition can considerably change during gas migration in the subsurface because of chemical and physical processes such as oxidation or molecular fractionation (Etiope, 2018). In this way, the observed CH_4 isotopic ratio in the martian atmosphere could be misleading and should be carefully interpreted using, for instance, additional

geological analysis.

2.3.2 Geologic production

Thermogenesis of abiotic organics

Methane can be produced by thermogenesis of organic matter, which can derive either from biological activity as mentioned previously or from abiotic processes (Oehler and Etiope, 2017). Abiotic organics are delivered to Mars by meteorites, comets and interplanetary dust particles. Assuming present-day fluxes of meteoritic material, Flynn (1996) calculated a total carbon amount of 10^{15} kg delivered to the martian surface over the age of the Solar System. However, he mentioned that this carbon content should likely be higher than the latter estimation since the meteoritic flux was larger during the first half-billion years of Mars history. The thermal degradation of this abiotic organic matter, transported and accumulated in sedimentary basins by fluvial (during Mars' aqueous period) or aeolian processes (Grotzinger et al., 2013), may have led to methane production (Oehler and Etiope, 2017). In thermogenesis, CH_4 quantities, that become proportionately more important with increasing temperature, are expected to form along with other hydrocarbons above $\sim$60°C (Oehler and Etiope, 2017). The depth at which this temperature is reached in the martian subsurface depends on the local heat flow and the presence of heterogeneities in crustal thermal properties. On Mars, the largest lithospheric thermal gradients ($\sim$10 to >20°C km^{-1}) derived from gravity and topography data are found in the Noachian cratered southern highlands (McGovern et al., 2002, 2004). Assuming a surface temperature of 0°C and a geothermal gradient of 20°C km^{-1}, the required burial depth to start generating thermogenic methane would be 3 km. Once formed at depth by thermogenesis, methane would have to migrate upwards and be either trapped in subsurface reservoirs or released in the martian atmosphere (Oehler and Etiope, 2017).

Hydrothermal alteration of crustal rocks

The hydration of crustal ferromagnesian minerals (olivine [$(Mg,Fe)_2SiO_4$] and pyroxenes [$(Mg,Fe)SiO_3$]) produces H_2 as well as minerals from the serpentine group ($[Mg,Fe]_3Si_2O_5[OH_4]$) (Oze and Sharma, 2005). This process, called serpentinization, is common on Earth and takes place over a wide range of temperatures (<100°C to $\sim$400°C). The molecular hydrogen thus formed may then react with CO_2 or CO to generate methane via Fischer-Tropsch Type reactions (Etiope and Sherwood Lollar, 2013). However, serpentinization could directly lead to CH_4 pro-

duction, without the intermediary of H_2, if the reaction occurs in the presence of carbon-bearing hydrothermal fluid (Oze and Sharma, 2005), although it has not yet been observed experimentally (Etiope, 2015). Serpentinization could still be active nowadays in the martian crust due to deep magmatic activity, even if it is presumably less frequent than in the past of the planet (Chassefière and Leblanc, 2011b). A likely scenario would involve reactions occurring at low temperatures (<100°C) similar to those observed at Lost City, a serpentinization site in the Atlantic Ocean (Atreya et al., 2007). These moderate temperatures would be certainly reached in the martian subsurface at depths corresponding to the stability region of liquid water (approximately 2 to 20 km deep; Oze and Sharma (2005)), necessary for the serpentinization process. By contrast, Black Smoker type temperatures are predicted to be reached around 25-50 km deep (Atreya et al., 2007). In addition, olivine and pyroxene minerals have been detected at the martian surface using in particular OMEGA (Observatoire pour la Minéralogie, l'Eau, les Glaces, et l'Activité) and CRISM (Compact Reconnaissance Imaging Spectrometer for Mars) data (Ehlmann and Edwards, 2014). Their distributions, more important in the southern highlands, show especially large surface exposure at Nili Fossae, the region related to methane plumes (Mumma et al., 2009). Interestingly, this area corresponds to one of the few places where serpentine deposits have been observed as well (Ehlmann et al., 2010). If serpentinization is currently active on Mars, its products should not be observable with surface or orbital measurements given that reactions would take place in the martian crust. Nevertheless, the presence of serpentine deposits in several ancient martian terrains suggests that serpentinization was an effective process in the past of the planet (Ehlmann et al., 2010).

Other proposed geothermal reactions for abiotic CH_4 production on Mars are reduction of graphite with H_2O (<400°C), iron carbonate ($FeCO_3$) decomposition with water (∼300°C), uncatalyzed aqueous CO_2 reduction (150-300°C) (Etiope and Sherwood Lollar, 2013; Oehler and Etiope, 2017) and magma driven fluid interactions with basaltic crust where magmatic CO_2 is converted to CH_4 (Lyons et al., 2005). In the latter process, methane becomes the dominant C species in the fluid phase for temperatures below 430°C or depths shallower than ∼9.5 km.

Fischer-Tropsch Type (Sabatier) reactions

Fischer-Tropsch Type (FTT) reactions, often mentioned regarding CH_4 production on Mars, involve the catalytic hydrogenation of CO/CO_2 (Etiope and Sherwood Lollar, 2013; Oehler and Etiope, 2017). The CO_2-

based FTT reaction, referred as the Sabatier reaction, forms methane by one step following:

$$CO_2 + 4\ H_2 \rightarrow CH_4 + 2\ H_2O \tag{2.4}$$

This process takes place at temperatures varying between <100°C and ∼500°C (Oehler and Etiope, 2017) and with the help of a metal catalyst, which lowers the activation energy required for the reaction (Etiope, 2015). The latter, thus occurring on the surface of a metal, is illustrated in Fig. 2.4. Ultramafic rocks[2] are optimal for FTT-Sabatier reactions since they contain transition metals such as iron, nickel and chromium that have been experimentally used to efficiently catalyze the FTT synthesis above 200°C (Wang et al., 2011). Rhodium and ruthenium, much less abundant in ultramafic rocks (only trace amounts) than the previous cited metals, are however more effective catalysts that support the Sabatier reaction below 100°C (Etiope and Ionescu, 2015).

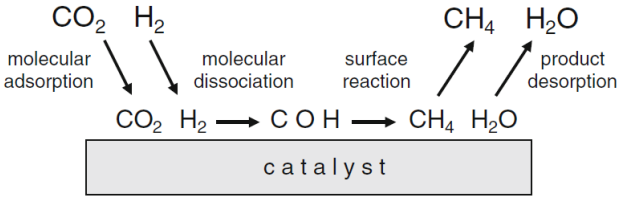

Figure 2.4: Production of methane via FTT-Sabatier reaction (Etiope, 2015).

The FTT synthesis is not very efficient in aqueous solution (Etiope, 2015). Therefore, the simplest way to produce methane, by this process and at moderate temperatures, is to proceed in a dry system such as unsaturated rocks and gas-filled fractures (Oehler and Etiope, 2017). This type of CH_4 formation is generally associated to serpentinization that makes H_2 available for the reaction. However, the FTT synthesis could be completely independent of the latter mechanism since H_2 can derive as well from radiolysis[3] of water, cataclasis[4] of silicates in the presence of water in fault zones, or volcanic degassing (Smith et al., 2005).

[2] Igneous rocks with a very low silica content (<45 wt% SiO_2) and composed of more than 90% mafic minerals (rich in magnesium and iron).
[3] Dissociation of molecules by radioactive isotopes.
[4] Deformation of rocks by crushing and shearing.

Volcanic degassing

As on Earth, primordial CH_4 delivered by meteorites during Mars accretion could be present in deep martian rocks, magma and the mantle. Methane could also be produced in the upper mantle from CO and CO_2 (Oehler and Etiope, 2017) or via carbonate reduction with pressures and temperatures ranging from 5 to 11 GPa and from 500 to 1500°C respectively (Scott et al., 2004). In this last case, one possible reaction can be written as follows:

$$8\ FeO + CaCO_3 + 2\ H_2O \rightarrow 4\ Fe_2O_3 + CH_4 + CaO \tag{2.5}$$

Although the volcanoes on Mars are potentially still active today, last phases of activity being as young as two million years in the regions of Tharsis and Elysium (Neukum et al., 2004), this magmatic methane is more likely associated to the past of the planet where volcanism was more significant.

Even if a volcanic origin of CH_4 is possible, it is important to note that volcanoes are not a large source of methane on Earth and represent less than 0.2 % of the total CH_4 budget (Atreya et al., 2007). In addition, amounts of sulfur dioxide in terrestrial fumarolic gases are 100 to 1000 times larger than those of methane. However, SO_2 has been unsuccessfully searched for in the martian atmosphere with a derived upper limit of 0.3 ppbv (Encrenaz et al., 2011). For these reasons, a volcanic origin of methane on Mars seems unlikely.

2.3.3 Meteoritic and cometary source

Methane on Mars can also be produced from exogeneous sources. The annual flux of micrometeoritic material to the top of the martian atmosphere has been estimated at 12,000 tonnes, but only a fraction of this amount (∼20%) is expected to reach the surface unaltered, the other part being heated above 900 K and pyrolysed upon atmospheric entry (Flynn, 1996). Among the total meteoritic flux, carbonaceous chondrites, a class of meteorites containing a few percent of organic matter and carrying minor amounts of free methane, represent just a small proportion. Court and Sephton (2009) studied the methane generated by ablation and pyrolysis of carbonaceous meteorites during entry in the atmosphere of Mars and found that this process, although leading to CH_4 quantities around two orders of magnitude larger than the free methane amounts in a representative carbonaceous chondrite, can only supply about 8 kg of methane every year. This mass is extremely low compared to the required 126-270 tonnes yr^{-1} (Formisano et al., 2004; Krasnopolsky et al.,

2004) and does not contribute to any measurable level of methane on Mars.

Once at the surface, CH_4 can be produced from meteoritic organic material exposed to ultraviolet (UV) radiation (Keppler et al., 2012; Schuerger et al., 2012). Indeed, Keppler et al. (2012) carried out experiments where samples of carbonaceous chondrite were irridiated and converted into significant amounts of methane under Mars-like surface conditions. The penetration depth of UV radiation is assumed ranging from 20 to 130 nm (Keppler et al., 2012), which suggests that all the organic matter available in meteorites would not be accessible for methane formation, although covering silicates layers may eventually be removed by physical and chemical weathering. Assuming an annual deposition rate of unaltered carbon at the martian surface of 2.4×10^5 kg (Flynn, 1996), Schuerger et al. (2012) estimated globally averaged methane abundance accumulated over geological time, due to photodegradation of this carbonaceous material, between 2.2 and 11 ppbv for conversion rates of organics to CH_4 of 20 and 100%, respectively. This evaluation was made based on a methane lifetime in the martian atmosphere of ∼330 terrestrial years (Lefèvre and Forget, 2009).

Delivery of methane by comets has also been considered, as well as the CH_4 synthesis via chemistry in the resulting impact cloud where reactions are catalyzed by recondensed dust (Kress and McKay, 2004). Assuming that the CH_4 content in cometary ice is about 1% (Gibb et al., 2003), the mean annual methane supply from infall of comets on Mars is predicted to be 1-2 tonnes (Formisano et al., 2004; Krasnopolsky, 2006; Atreya et al., 2007), far below the required amount to maintain a steady state CH_4 mixing ratio of 10 ppbv. However, this rate is probably not meaningful because of the rather low impact frequency of a typical size comet (1 km radius). Given its short lifetime of a few hundred years, present-day methane on Mars could consitute the residues of large quantities injected into the atmosphere via a cometary impact that occurred hundreds or thousands of years ago. It has been estimated that a comet with a radius ranging from ∼130 m to ∼360 m impacting Mars 100 to 2000 years ago respectively would have supplied enough methane to explain current levels (Formisano et al., 2004; Atreya et al., 2007), but the probability of such an event is only 0.0011 % (Krasnopolsky, 2006).

Although comets, meteorites and interplanetary dust could contribute to methane concentrations observed on Mars, the spatial variation of CH_4 remains problematic to explain with this kind of source. Indeed, the gas should be uniformly distributed in the atmosphere few months after the impact event or with a constant micrometeoritic flux bringing in methane. Schuerger et al. (2012) showed that surface impacts, airbursts

of bolides, and cascading airbursts of low-density rubble-pile comets were all enable to create large CH_4 variations in the martian atmosphere. Similarly, photodegradation of micrometeorites would unlikely produce observable spatial and temporal fluctuations in the CH_4 concentration without the support of another active generation mechanism (Keppler et al., 2012). Webster et al. (2018) actually reported variation in the CH_4 background levels measured at Gale crater larger than that predicted due to UV-irridiated organics. Recently, Fries et al. (2016) proposed that high methane events are correlated with meteor showers, occurring when Mars passes through the dust trail left behind by comets orbiting the Sun. However, Roos-Serote et al. (2016) did not find any correlation between both events by analysing data including new methane measurements from the SAM instrument.

2.3.4 Photochemical production

Bar-Nun and Dimitrov (2006, 2007) suggested that methane production by photolysis at 184.9 nm of water vapor in the presence of CO is possible and favored thermodynamically under the martian conditions. This proposed CH_4 formation process is based on experiments carried out at pressure of 390 mbar and at temperature of 329 K and on thermodynamic equilibrium calculations performed under the experimental and martian atmospheric conditions. At first, H_2O photolysis generates a hydrogen atom and an OH radical:

$$H_2O \xrightarrow{h\nu} OH + H \tag{2.6}$$

The OH radical reacts then quickly with CO to form carbon dioxide and another hydrogen atom following:

$$OH + CO \rightarrow CO_2 + H \tag{2.7}$$

About half of the hydrogen atoms recombine to form H_2 while the other part can react with CO to produce CH_2O, CH_3OH and then CH_4. A possible pathway for these reactions was proposed by Bar-Nun and Dimitrov (2006, 2007) as follows:

$$H + CO + M \rightarrow HCO + M, \tag{2.8}$$
$$HCO + H + M \rightarrow CH_2O + M, \tag{2.9}$$
$$HCO + HCO \rightarrow CH_2O + CO, \tag{2.10}$$
$$CH_2O + CH_2O \rightarrow CH_3OH + CO, \tag{2.11}$$
$$CH_3OH + H \rightarrow CH_3 + H_2O, \tag{2.12}$$
$$CH_3 + H + M \rightarrow CH_4 + M. \tag{2.13}$$

However, Krasnopolsky (2007) claimed that the proposed reaction scheme was not quantitatively justified by chemical kinetics, reaction rates being too slow to replenish CH_4 at a rate that counterbalance its destruction and the presence of O_2 preventing one of the key reactions. In addition, he mentioned the inappropriate application of thermodynamic equilibrium calculations to the martian atmosphere.

In their answer to Krasnopolsky (2007), Bar-Nun and Dimitrov (2007) estimated that the possibility of CH_4 formation by their approach can not be ruled out given that the kinetic analysis performed by Krasnopolsky (2007) was not the most representative one. Indeed, a reliable conclusion on methane formation can be determined only by a complete Adequate Kinetic Model followed by a Generalized Kinetic Analysis (Bar-Nun and Dimitrov, 2007). Moreover, they demonstrated that the presence of molecular oxygen in experiments does not prevent CH_4 formation. And although martian atmosphere is not in thermodynamic equilibrium, experimental results have been replicated fairly well by Bar-Nun and Dimitrov (2007) using thermodynamic equilibrium calculations, as methane mixing ratio between both differs by a factor of less than 2. Bar-Nun and Dimitrov (2007) eventually recommended to repeat experiments in more Mars-like conditions to determine if CH_4 production by photolysis of H_2O in the presence of CO is a process currently at work on the Red Planet.

2.4 Methane subsurface reservoirs on Mars

Once generated, CH_4 will move along faults and fractures and through permeable layers in the subsurface and be either trapped in reservoirs or released into the martian atmosphere by seepage at the surface. Regardless of its production mechanism, past or present methane could be stored in clathrate hydrates, zeolites or sealed traps.

Under appropriate low temperature and high pressure conditions, water can solidify in the presence of gases to form clathrate hydrates. These

crystalline compounds are constituted by a lattice of hydrogen-bonded water molecules forming cavities inside of which guest gas molecules are trapped. These ice-like solids are known for their capacity to store a large amount of gas, including methane, in a very stable and compact configuration. On Earth, they are present in permafrost and in marine sediments, mainly along continental margins. They tend to form massive deposits within high porosity spaces and beneath less permeable sediment layers, where migrating gas and ice can accumulate (Elwood Madden et al., 2009). Thermodynamic conditions prevailing on Mars favor clathrate formation from near subsurface to deep down in the cryosphere (<15 m up to 24 km deep; Max et al. (2011)) and kinetics experiments (Gainey and Elwood Madden, 2012) showed that their dissociation, initiated by a change in temperature, pressure or composition of the reservoir, is a feasible mechanism for near-surface methane release. The thickness of their stability zone is complex to determine and depends on many factors such as local geothermal gradient, pressure, salinity of the water involved in the clathrate formation, average surface temperature, recent thermal history of the crust and the subsurface heterogeneity. Clathrate hydrate reservoirs formed in the past of Mars in contact with an ancient CH_4 source could have remained stable at depth over geologic time. Their estimated storage capacity from the methane possibly released by early serpentinization processes is largely sufficient to account for intermittent CH_4 releases (Lasue et al., 2015), such as the plume observed by Mumma et al. (2009). In addition, it has been proposed that methane could come from metastable sub-micron particles of clathrate hydrate transported intact from the subsurface into the atmosphere and dissociated under the effect of water condensation on the clathrate crystals (Chassefière, 2009). This process could explain the spatial and temporal correlations between methane and water vapour mixing ratios observed by Geminale et al. (2008, 2011) and Mumma et al. (2009).

Zeolites, commonly deriving from the interaction between low temperature (< 200°C) alkaline brines and volcanic glass, have been proposed as potential methane reservoirs that would trap CH_4 by adsorption (Holmes et al., 2015; Mousis et al., 2016). These materials are expected to be widespread on Mars and have actually been detected in various places of the Red Planet (Ruff, 2004; Carter et al., 2013). Most of hydrous minerals have been discovered on ancient terrains as they were formed during the Noachian period when liquid water was frequently present at the surface, although some zeolites, perhaps resulting from ice-volcano interactions, have been observed in younger lowlands as well (Carter et al., 2013). Chabazite and clinoptilolite have been suggested as zeolite storage reservoirs comparable to clathrate hydrates but support-

ing higher temperatures (Mousis et al., 2016). Indeed, like clathrates, the trapping in these zeolites becomes more efficient with increasing temperature and from a gas phase enriched in CH_4 (i.e., from an atmosphere richer in methane on early Mars or from a current/past subsurface source; Mousis et al. (2016); Thomas et al. (2009)). This is why, given the poor atmospheric CH_4 levels and the cold surface temperatures, chabazite and clinoptilolite could not serve as methane sinks if they are in contact with the current martian atmosphere. However, if they are located at sufficient depth to remain isolated from the atmosphere, zeolites could have conserved enough amounts of methane originated from an ancient or modern source. Processes such as impacts, seismic activity or erosion could lead to their destabilization and the subsequent CH_4 release in the atmosphere of Mars (Mousis et al., 2016).

Finally, methane could accumulate in subsurface traps sealed by ice and be periodically discharged when permafrost melts or sublimes. Such reservoirs could be either porous sedimentary rocks or fracture zones related to impacts or serpentinization (Oehler and Etiope, 2017). Indeed, the latter process generates large volume expansion resulting thereby in episodic cracking (Macdonald and Fyfe, 1985). In addition, it has been suggested that ancient methane could have been trapped in fluid inclusions and interstitial sites in basalt (McMahon et al., 2013). This methane could then be released in the present-day martian atmosphere due to erosion processes.

Any methane, biotic or abiotic, past or present, could be sequestered in the aforementioned subsurface reservoirs. It is certainly possible that the early martian atmosphere was richer in methane due to volcanism and hydrothermal activity. As the planet cooled, a growing layer of permafrost could have trapped some of the CH_4 as clathrate hydrates (Pellenbarg et al., 2003). Alternatively, methane currently generated at depth in the martian crust would migrate upwards to reach the local hydrate stability zone and be enclathrated. It could also seep into a sealed trap in the cryosphere where surrounding porous spaces are filled with ice or clathrates. Methane could eventually remain as a gas pocket or diffuse through the neighboring ice and be converted to CH_4 clathrates (Pellenbarg et al., 2003).

2.5 Methane loss mechanisms on Mars

Currently, the only methane sink accepted on Mars is its photochemical destruction through its photolysis by the Lyman α line above $\sim$80 km altitude, and its oxidation by OH or $O(^1D)$ below (Haberle et al., 2017),

leading to a CH_4 chemical lifetime of about 300 terrestrial years (Lefèvre and Forget, 2009). However, the spatial and temporal heterogeneity of methane observed on Mars (see section 2.1) implies powerful destruction mechanisms acting about 600 times faster than photochemistry (Lefèvre and Forget, 2009). Several loss processes have been proposed but none of them has been identified to date.

Although the reported CH_4 levels on Mars are far too low to support widespread colonies of methanotrophs (Zahnle et al., 2011), microbial organisms could be concentrated locally, in serpentinization systems for instance. The anaerobic oxidation of methane is a major sink on Earth with the consumption of 80-90% of the CH_4 produced in marine sediments and has been suggested as a plausible metabolism for both ancient and present-day Mars (Marlow et al., 2014). In this process mediated by methanotrophic archaea and sulfate-reducing bacteria, methane is oxidized with sulfate as the electron acceptor in groundwater. Various sulfate minerals have been detected on the martian surface especially in numerous locations correlated with expected aqueous activity (Murchie et al., 2009). In particular, sulfate-bearing rocks have been discovered overlying a unit with olivine and serpentine beneath the Syrtis Major lava flows (Ehlmann and Mustard, 2012).

More likely than a biological sink, diverse loss processes implying interactions with mineral grains have been proposed. Large-scale electric fields generated during martian dust storms are expected to dissociate methane and could even explain the reported CH_4 atmospheric heterogeneity given the regional and temporal variability of this phenomenon (Farrell et al., 2006). Electric discharges in dust storms are also associated with the production of large amounts of hydrogen peroxide (H_2O_2) that can oxidize methane (Atreya et al., 2007). However, numerical modelling showed that both aforementioned mechanisms are not significant on Mars (Kok and Renno, 2009). Although the heterogeneous oxidation of methane by the martian surface has been suggested as a possible chemical sink (Lefèvre and Forget, 2009; Mumma et al., 2009), experiments using H_2O_2 and perchlorate salts showed that these strong oxidants were probably not responsible for the methane atmospheric variations on Mars (Gough et al., 2011).

Zahnle et al. (2011) pointed out the importance of not supposing the existence of an unknown source of oxidizing power so strong that it would overwhelm the redox budget of the martian atmosphere. Although the present atmosphere is oxidized, it is expected to not evolve anymore and to be now in a steady state with the balance between the (net oxidizing) escape of hydrogen and the (net reducing) escape of oxygen (Chassefière and Leblanc, 2011a). However, these escape fluxes actually differ,

the H flux being at least 4 times larger than the O flux, which requires therefore the presence of an unknown surface sink of oxygen (Nair et al., 1994). Chassefière and Leblanc (2011a) proposed the oxidation of the methane released at the surface as a probable mechanism that would remove oxygen from the atmosphere. Indeed, assuming that CH_4 is discharged without H_2, they found a good agreement between the methane surface flux constrained by observations (including its estimated lifetime of 200 days) and the value needed for the balance of the H and O escape fluxes. Since most of the methane generation mechanisms imply H_2 production, this hypothesis favors the presence of near subsurface reservoirs, such as clathrate hydrates, from which ancient methane would be presently expelled, while the H_2 formed at the same time period as CH_4 would have been released sooner to the atmosphere due to its high volatility (Chassefière and Leblanc, 2011a). However, this theory is only consistent if the methane release and its subsequent oxidation have been a small but steady process since at least 3 Myr (Chassefière and Leblanc, 2011a), which is in conflict with the sporadic discharges suggested by the observations (Mumma et al., 2009; Webster et al., 2015, 2018).

Alternatively, Gough et al. (2010) proposed that methane could be reversibly adsorbed in the uppermost layer of the martian regolith. The seasonal cycle of adsorption during winter and desorption in the summer months is consistent with the reported variability of methane. However, this hypothesis ignores competition for adsorption sites and other species such as xenon still remain continuously in the martian atmosphere though they should be adsorbed faster than CH_4 (Zahnle et al., 2011). Moreover, the efficiency of the adsorption process was found very limited by Meslin et al. (2011) who investigated atmosphere-subsurface exchanges with a Global Climate Model and were unable to reproduce large seasonal CH_4 variations. For thermodynamic reasons and as mentioned in the previous section, the sequestration of methane in clathrates and zeolites from the current martian atmosphere with low CH_4 abundances could not act either as a significant loss mechanism (Thomas et al., 2009; Mousis et al., 2016).

Recently, experiments have supported the proposed methane sink by formation of Si-CH_3 covalent bonds on mineral grain sites activated by wind erosion (Jensen et al., 2014). The experimentally observed CH_4 lifetime corresponds well with the period estimated from the measurements. Indeed, a plume of 270 tonnes (Krasnopolsky et al., 2004) would take about one third of a year to be removed with only $\sim 10^6$ tonnes of activated silicate (Jensen et al., 2014). Interactions with UV radiation may however lead to the instability of this potential sink and the pres-

ence of methylated material on Mars should be investigated in the future (Jensen et al., 2014).

2.6 Current and future missions

The spatial and temporal variations of methane mixing ratio observed in the martian atmosphere and its resulting short lifetime challenge considerably our current understanding of the atmospheric chemistry and physics on Mars. This is why present and future searches for CH_4 are an important priority.

NASA's Curiosity rover will continue to monitor seasonal variations of CH_4 levels at Gale crater. Likewise, the ESA's probe Mars Express, still in operation, will remain in search for martian methane with the PFS spectrometer. MAVEN (Mars Atmosphere and Volatile EvolutioN), the NASA's orbiter launched in 2013, is currently studying atmospheric escape and may provide useful contextual information although it is not equipped to measure methane. The Mars Orbiter Mission (MOM), India's first spacecraft to Mars launched at the same time period as MAVEN, carries a methane sensor (Lele, 2014). The science phase of this mission is underway with the use of five instruments investigating the surface and atmosphere of the Red Planet. In 2016, the ESA Roscosmos ExoMars Trace Gas Orbiter (TGO) dedicated in particular to the study of methane and other trace gases was launched. The measurement campaign has started after an aerobraking phase that was conducted over a year from March 2017. TGO carries four instruments including two spectrometer suites able to precisely detect and monitor any CH_4 plumes: Nadir and Occultation for MArs Discovery (NOMAD) that covers a spectral range from the ultraviolet to the infrared (Vandaele et al., 2015) and Atmospheric Chemistry Suite (ACS) that operates in the infrared range (Korablev et al., 2018). Both instruments allow methane identification with a very high accuracy (ppt level; Vandaele et al. (2015); Korablev et al. (2018)), preventing therefore any confusion induced by instrumental artefacts. In other words, NOMAD and ACS will be able to detect any discharge of methane with an improved sensitivity of about 100 times compared to the performances obtained with Mars orbit and Earth instruments and around 10 times better than in-situ measurements from the Curiosity rover (Webster et al., 2015, 2018). In addition to methane, TGO is searching for a suite of related trace gases as well as isotopologues that will help to clarify the mechanisms of methane production and destruction.

In the coming years, missions to Mars will remain in the foreground. NASA's InSight mission, newly landed on the Red Planet in November 2018, carries three science instruments that will investigate the interior structure and processes in order to better understand the planet's evolution. The year 2020 will see the launch of two other missions: NASA's Mars 2020 rover and the second part of the ESA Roscosmos ExoMars Program including a rover and a surface platform. Both rovers aim to discover preserved evidences of past life and, for that purpose, will drill, collect and analyze underground samples, more conducive to the conservation of biosignatures. These future missions, focused on subsurface processes, may thereby shed new light on martian methane and its still unidentified but probably subterranean source(s).

2.7 Summary

Several detections of methane in the martian atmosphere have been reported from Earth-based and Mars orbit instruments (Formisano et al., 2004; Krasnopolsky et al., 2004; Geminale et al., 2008, 2011; Mumma et al., 2009; Fonti and Marzo, 2010) with abundances ranging up to tens of ppbv. These observations have evidenced spatial variability of CH_4, suggesting the presence of localized subsurface sources. Recently, Webster et al. (2015, 2018) reported in situ detection of methane performed by the Mars Science Laboratory rover at Gale crater. The measurements covering a 5-Earth year period showed strong seasonal variations of CH_4 background levels which reach a maximum at the end of the northern summer. Webster et al. (2018) observed an average mixing ratio of 0.41 $\pm$ 0.16 ppbv with elevated levels up to $\sim$ 7 ppbv, implying that methane is episodically released in the atmosphere of Mars.

Although the presence of methane on Mars remains controversial (Zahnle et al., 2011; Zahnle, 2015), its multiple detections in the planet's atmosphere have raised numerous questions about its potential sources. Given the relatively short lifetime of CH_4 in the martian atmosphere (standard photochemical models predict a lifetime of 300-600 terrestrial years), its presence implies the existence of a subsurface reservoir or an active primary source. It has been suggested that methane on Mars could have a biological origin and be generated by organisms living in the subsurface where conditions are more hospitable (Weiss et al., 2000; Atreya et al., 2007). Methane can also be produced through several abiologic processes, including serpentinization where ultramafic rocks react with water producing H_2 (Oze and Sharma, 2005) that can then be used to form methane via Fischer-Tropsch Type reactions (Etiope and

Sherwood Lollar, 2013). This hypothesis is supported by observations of serpentine deposits on Mars, in particular in the Nili Fossae region (Ehlmann et al., 2010). Regarding the CH_4 loss process, several have been proposed such as heterogeneous chemistry (Lefèvre and Forget, 2009), triboelectricity (Farrell et al., 2006; Atreya et al., 2007) or physical and chemical sequestration in the soil (Gough et al., 2010; Jensen et al., 2014) but none of them has been identified to date.

Independently of methane formation mechanism(s), CH_4 produced in the past or at present-day could be stored in subsurface reservoirs such as clathrate hydrates (Chastain and Chevrier, 2007) or zeolites (Holmes et al., 2015; Mousis et al., 2016). Thermodynamic conditions prevailing on Mars favor clathrate formation from near subsurface to deep down in the cryosphere (until several kilometers deep) and kinetics experiments (Gainey and Elwood Madden, 2012) showed that their dissociation, initiated by a change in temperature, pressure or composition of the reservoir, is a feasible mechanism for near-surface methane release on Mars.

Many processes on the Red Planet have yet to be understood, but in a near future, Trace Gas orbiter will surely reveal new interesting clues concerning methane on Mars and its possible sources so that methane will remain a hot topic. And with the constantly growing number of atmospheric observations and future missions dedicated to the subsurface, this martian mystery is getting closer to be uncovered.

Chapter 3

Clathrate hydrates

Contents

3.1 Molecular structure 34
3.1.1 Structure I 35
3.1.2 Structure II 35
3.1.3 Structure H 36
3.1.4 High pressure clathrate structures 38
3.2 Characteristics of guest molecules 38
3.3 Properties: clathrate vs water ice 40
3.4 Stability of clathrate hydrates 42
3.4.1 Clathrate stability zone 44
3.5 Formation and dissociation processes 46
3.6 Clathrate hydrates in the Solar System . . . 47
3.6.1 Comets 47
3.6.2 Mars 48
3.6.3 Outer Solar System 49
3.7 Summary 50

The purpose of this chapter is to review the molecular structures of the three common types of clathrate, their thermo-physical properties and to compare them with water ice, a component with which they share many similarities. This chapter deals also with clathrate stability, formation and dissociation and defines the clathrate stability zone that will be specifically investigated for Mars in the following chapters. Finally, the end of this chapter is dedicated to the possible existence of clathrate hydrates in other Solar System bodies. Any reader that would like to know more about clathrates is referred to Sloan and Koh (2007).

3.1 Molecular structure

As crystalline compounds, clathrates involve the repetitive and three-dimensional translation of the unit cell. The latter is itself composed of hydrogen-bonded water molecules forming distinct polyhedral cavities (or cages) that interact with their entrapped gas molecule through weak van der Waals forces to lower the free energy and enhance clathrate stability (Buffett, 2000). Five types of cavity are encountered in clathrate hydrates formed in nature and are referred to as s^f, where f is the number of faces with s sides per cage (e.g., Sloan and Koh (2007)). The various cavities and their configuration are shown in Fig. 3.1:

- The pentagonal dodecahedron (5^{12}, 12 pentagonal faces), which is common to all clathrate hydrate structures, contains 20 water molecules.
- The tetrakaidecahedron ($5^{12}6^2$, 14 faces consisting of 2 facing hexagons and 12 connecting pentagons) includes 24 water molecules.

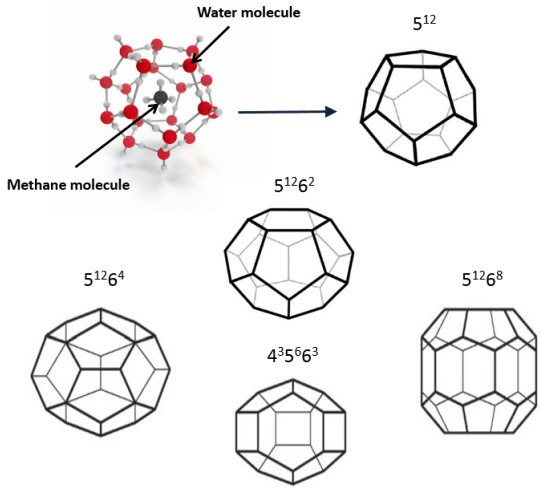

Figure 3.1: The different types of cavity in clathrate hydrates: the 5^{12} cage showing methane and water molecules (top left, credits: Mikkel Juul Jensen) and geometry of other cages where the line intersections represent the positions of oxygen atoms.

- The most spherical cage, the hexakaidecahedron ($5^{12}6^4$, 16 faces including 4 hexagons, each surrounded entirely by pentagonal faces) is composed of 28 water molecules.

- The irregular dodecahedron ($4^3 5^6 6^3$, 12 faces where two groups of three pentagons face each other and are separated by a band that alternates squares and hexagons) is also formed with 20 water molecules.
- The icosahedron ($5^{12}6^8$, 20 faces with 2 facing hexagons surrounded by pentagons and separated by a central band made of 6 hexagons), which is the most oblate cavity, contains 36 water molecules.

The different structures of clathrate hydrate have been mostly deduced from x-ray diffraction studies. Each of them consists of a particular arrangement of cavities, the cage type and number being specific to a given structure. The structures commonly observed in clathrate hydrates formed in natural environments are the cubic structures I and II denoted by the symbols sI and sII, respectively, and the hexagonal structure sH. These structures are described below.

3.1.1 Structure I

The unit cell of structure I is composed of 46 water molecules forming 2 small and 6 large cavities corresponding to pentagonal dodecahedra (5^{12}) and tetrakaidecahedra ($5^{12}6^2$), respectively. The small cavities are located at the center and the corners of the unit cell to form a body-centered cubic structure with an average lattice parameter $a = 12$ Å. The 5^{12} cages are linked by the large cavities as shown in Fig. 3.2. The theoretical hydration number (the ratio between the number of water molecules and the number of gas molecules) for the sI clathrates with one molecule per cage is 5.75 (46/8). However, the latter is generally higher because some cavities often remain empty. For instance, Circone et al. (2005) directly measured the composition of structure I methane clathrate along the equilibrium curve near 273 K, by monitoring the pressure of free gas during the formation and dissociation of clathrates, and found an average hydration number of $\sim$6.

3.1.2 Structure II

In the structure II, the unit cell is a face-centered cubic lattice, which fits within a cube of 17.3 Å on a side, and is composed of 136 water molecules forming 16 small and 8 large cavities. The small cages are the same as in structure I, although their diameter is slightly smaller due to a minor distortion of the cages. Their different arrangement, as represented in Fig. 3.3, creates large cavities of type $5^{12}6^4$. In this structure, if all cavities are filled with one guest species, the hydration number equals 5.67 (136/24).

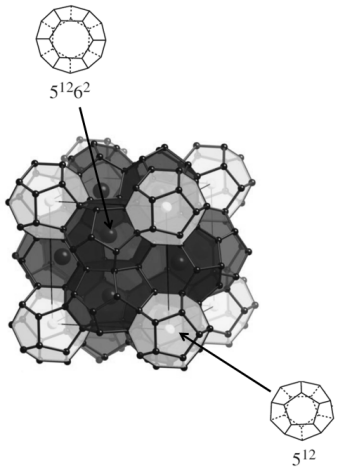

Figure 3.2: The unit cell of sI clathrate hydrate (Ranieri et al., 2017).

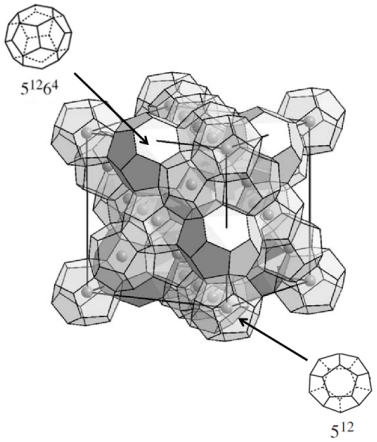

Figure 3.3: The unit cell of sII clathrate hydrate (Skiba et al., 2009).

3.1.3 Structure H

The sH clathrates are less frequent in nature than those with a cubic structure. Their hexagonal unit cell, with lattice parameters $a = 12.2$ Å, $c = 10.1$ Å, $\alpha = \beta = 90°$ and $\gamma = 120°$, contains 34 water molecules forming three different types of cavity: small (5^{12}), medium ($4^3 5^6 6^3$) and large ($5^{12}6^8$), the small cavities being identical to those of structures I and II. The sH clathrate unit cell contains six cages including 3 small, 2 medium and 1 large. This structure is organized in layers as shown in Fig. 3.4 where layers of 5^{12} cavities alternate with layers of medium $4^3 5^6 6^3$ and large $5^{12}6^8$ cavities. The hydration number for the structure

H with a fully occupied lattice is 5,67 (34/6).

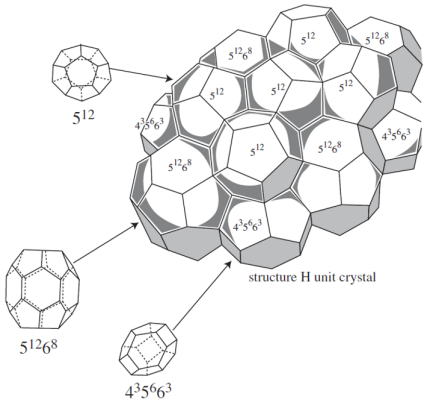

Figure 3.4: The unit cell of sH clathrate hydrate (Maslin et al., 2010).

Generally, each cavity can contain at most one guest molecule and as they are prevented from collapse by the repulsive interactions with their guest molecule or the guests trapped in the neighboring cavities, clathrates require a minimum occupancy level to be stable. The term simple clathrate is used when only one guest species is trapped in the cages of the structure. The binary (or double) clathrate contains two gas species, one occupying the small cavities and the other guest only occupying the large cages. Finally, mixed (or multicomponent) clathrates include several species in the cavities of the same type.

The different structure parameters previously discussed are listed in Table 3.1 for sI, sII and sH clathrates. They will be used in the following chapters, in particular to determine the cavity occupancy of methane clathrate.

Table 3.1: Clathrate hydrate structure parameters (Sloan and Koh, 2007).

	sI		**sII**		**sH**		
Cavity type	Small	Large	Small	Large	Small	Medium	Large
Description	5^{12}	$5^{12}6^2$	5^{12}	$5^{12}6^4$	5^{12}	$4^35^66^3$	$5^{12}6^8$
Number of cages per unit cell	2	6	16	8	3	2	1
Average cavity radius[a] (Å)	3.95	4.33	3.91	4.73	3.94	4.04	5.79
Coordination number[b]	20	24	20	28	20	20	36
H_2O molecules per unit cell	46		136		34		

[a] The cavity radius will change with temperature, pressure and guest composition.
[b] The number of water molecules per cavity.

3.1.4 High pressure clathrate structures

The three molecular structures presented above form at near-ambiant pressure. However, when pressure increases (in the GPa range), clathrate can undergo structural transitions as a result of its compression. Methane sI clathrate has been observed to change to a dense hexagonal structure (sH') around 1 GPa, and then to a structure called filled-ice above 2 GPa (Loveday et al., 2001a,b). This last structure has a network closely related to hexagonal ice (Ih), where water molecules are organized in sheets. Therefore, the methane molecules do not occupy cages anymore but instead sit between the sheets. Systems forming sII clathrates at low pressure appear to have an additional intermediate stage between the hexagonal and filled-ice structures where they adopt a tetragonal structure (sT) (Loveday and Nelmes, 2008). Whichever guest gas is considered, the filled-ice structure seems to be the final structure adopted by clathrate hydrates upon compression (Choukroun et al., 2013).

In this work, we consider the pressure range related to the upper martian crust (max 20 km deep, < 200 MPa) as well as gas species consistent with the composition of the martian atmosphere. Knowing that methane and carbon dioxide form sI clathrate, whereas nitrogen and argon are sII clathrate formers (Sloan and Koh, 2007), the relevant clathrate structures are the cubic structures described in sections 3.1.1 and 3.1.2.

3.2 Characteristics of guest molecules

The guest molecule must satisfy two criteria: one regarding its chemical nature and the other on its size and shape. Indeed, the guest must not carry either a strong hydrogen-bonding group or several moderately strong hydrogen-bonding groups (Jeffrey, 1984). On the other hand, clathrate hydrates cannot form without guests of the proper size as these guests have to adequately fill the cavities in order to optimize the van der Waals interactions between them and the water molecules. When the guest/cavity size ratio is less than 0.76, the guest molecule can fit in the cavity but the molecular attractive forces contribute less to the stability of the cage. And when this ratio is larger than 1, the guest cannot enter into the cavity without distortion (Sloan and Koh, 2007). Consequently, a guest species occupies preferentially a type of cage according to its size and favors the crystallization of a type of structure. A comparison between the size of guest molecules and the cavities they occupy in simple clathrates is given in Fig. 3.5.

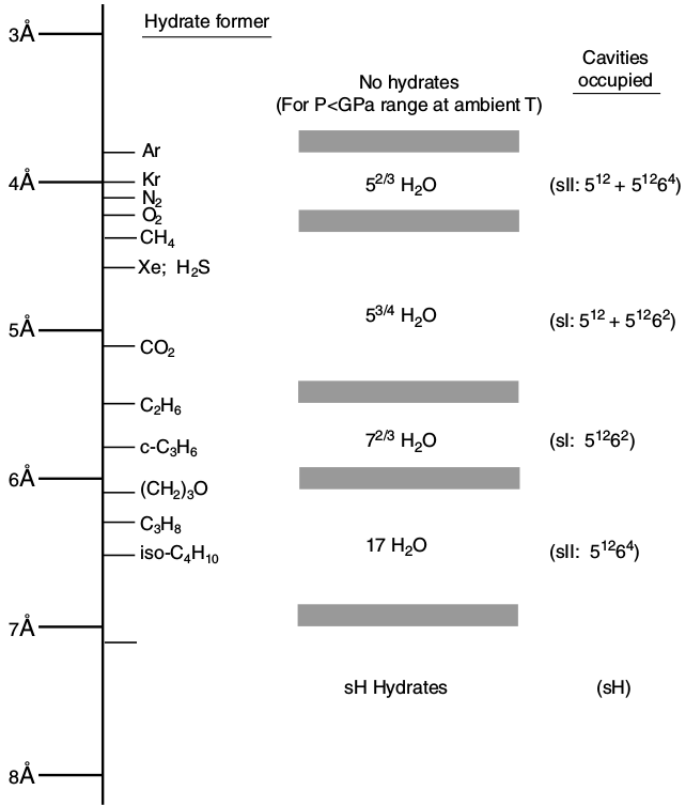

Figure 3.5: Comparison between the size of guest molecules and the cavities they occupy in simple clathrates (Sloan and Koh, 2007). The corresponding hydration numbers are listed in the central column.

At standard temperature and pressure conditions, molecules smaller than 3.5 Å are unable to stabilize any cavity, while those having diameters above 7.5 Å are too large to occupy the cages of sI and sII clathrates. The guests between 4.2 and 6 Å, such as methane, hydrogen sulfide, carbon dioxide and ethane, are sI clathrate formers. However, while CH_4, H_2S and CO_2 fit into small and large cavities, C_2H_6 can only enter into large cages. As a result, the hydration number of ethane clathrate is higher than the one calculated for a fully occupied lattice and equals 7.67 (46/6). Structure II is formed with molecules having diameters between 6 and 7 Å, such as propane and iso-butane, or with small species (d $<$ 4.2 Å) like argon and nitrogen. Although these last guests can fit into all cage types of sI and sII, their small size is more adapted to the 5^{12} cavity. The ratio small/large cavities being higher in the sII unit cell, structure II is therefore more stable for Ar and N_2.

Contrary to sI and sII clathrates that can form with a single guest type, two sizes of molecules are required to stabilize the sH structure, which thus always crystallizes to form binary clathrate. Guests of size between 7 and 9 Å can fit into the large $5^{12}6^8$ cavity provided that they meet the shape requirements, while the smaller companion molecules occupy the medium and small cages. For structure H, both size and shape of the guest molecule are significant because formation of these clathrates at low pressure requires really effective space filling of the large cavity. The shape is not a critical parameter for sI and sII clathrates since almost all molecules with the proper size will stabilize the structure (Sloan and Koh, 2007).

It is interesting to note that binary clathrates including two sI guests can adopt a structure II depending on pressure and/or composition. This is the case for the CH_4/C_2H_6 mixture, while the combination of methane and carbon dioxide always forms sI clathrate (Sloan and Koh, 2007). Finally, although molecules smaller than 3.5 Å, such as H_2 (d = 2.72 Å), cannot form clathrate at ambient pressure, H_2/H_2O mixtures have been observed to form sII hydrogen clathrate in recent high-pressure experiments (200 MPa) with the small and large cavities occupied by a cluster of two and four H_2 molecules, respectively (Mao et al., 2002). However, Lokshin et al. (2004) reported a maximum occupancy of only one D_2 molecule in the small cage, while the large cage occupancy can vary from two to four D_2 molecules depending on the temperature. Multiple occupancy of the large cage of structure II at high pressure has been also recognized for nitrogen, oxygen and argon clathrates (Chazallon and Kuhs, 2002; Manakov et al., 2004).

3.3 Properties: clathrate vs water ice

Ice Ih is sometimes used as a proxy for clathrate hydrate properties. All common clathrate structures consist of at least 85% water and, although they present a cage-like organization, their hydrogen-bonded H_2O network has strong similarities with water ice. The O-H bond angles and bond lengths in ice Ih are nearly the same in clathrate compounds (Sloan and Koh, 2007), while the frequencies of vibrational modes of O-H and O-O bonds are identical in both structures (Dartois and Deboffle, 2008; Dartois and Schmitt, 2009). However the presence of gas molecules within clathrate hydrate strongly affects the molecular interactions, resulting in some differences in the thermo-physical properties such as mechanical strength, thermal conductivity and density (see Table 3.2).

Table 3.2: Some properties of water ice compared to those of methane clathrate. Unless indicated, all values are from Sloan and Koh (2007).

Property	Water ice Ih	CH_4 clathrate
Density (kg m^{-3})	916[a]	912[a]
H_2O diffusion jump time (μs)	2.7	> 200
Dielectric constant at 273 K	94[a]	$\sim$58[a]
Young's modulus at 268 K (GPa)	9.5	$\sim$8.4
Poisson's ratio	0.3301	0.3140
Thermal conductivity at 263 K (W m^{-1} K^{-1})	2.18	0.51
Heat capacity within 250 - 270 K (J kg^{-1} K^{-1})	1900 (250 K)-2100 (270 K)	2080
Linear thermal expansion at 200 K (10^{-6} K^{-1})	56	77
Heat of dissociation (kJ mol^{-1})	6	18.01 ($\rightarrow$ ice + gas)[b] 53.5 ($\rightarrow$ liquid water + gas)[b]

[a] Max (2003)
[b] Anderson (2004)

Despite similar elastic properties, compression deformation experiments at 260-287 K and 50-100 MPa have shown that methane clathrate is as much as 40 times stronger than ice Ih (Durham et al., 2003). This higher mechanical strength has been attributed to the slower H_2O diffusion rate in the clathrate lattice (Durham et al., 2003). Indeed, as can be seen in Table 3.2, this rate is two orders of magnitude larger in clathrate hydrates than in ice (Sloan and Koh, 2007). However, at lower stresses (< 0.5 MPa), relevant to near-surface regions of planetary bodies, clathrate hydrates and water ice seem to have comparable flow behaviors (Choukroun et al., 2010a). In any case, the mechanical properties of clathrate hydrates can be useful for the characterization of planetary surfaces, especially the formation of chaotic terrains, large areas of depressions possibly linked to clathrate dissociation (Rodriguez et al., 2006; Komatsu et al., 2011). The volume increase associated with the destabilization of clathrates leads to the discharge of gases and fluidized sediments and the subsequent formation of landforms. The loss of subsurface clathrate layers with a potentially high intrinsic strength could thus amplify these surface mass movements (Durham et al., 2003).

The thermal conductivity of clathrate hydrates is unusually low, about a fifth of that of water ice, with average values of 0.4-0.7 W m^{-1} K^{-1} at pressures lower than 100 MPa and temperatures from 100 to 270 K (Choukroun et al., 2013), which makes it closer to that of liquid water (0.605 W m^{-1} K^{-1}). In addition, the thermal conductivity of clathrates

has been found to increase slightly with increasing temperature (Ross et al., 1981), while most crystalline structures behave inversely. This curious glass-like behavior is related to the resonant coupling between guest and host vibrations, which also results in a notable decrease in the transport of heat (Tse and White, 1988). The thermal expansivity is another property where clathrates and water ice diverge. Again, this difference is due to the presence of guest molecules whose motions exert an internal pressure to weaken the hydrogen bonds of the host lattice (Tse, 1990).

The density of clathrate hydrates can considerably vary since it depends mainly on the nature of the guest species and the degree of cage occupancy. At standard conditions, the density of clathrates relevant to planetary environments ranges from ∼900 kg m^{-3} for CH_4 to ∼1800 kg m^{-3} for Xe (Choukroun et al., 2013). Note that methane clathrate is the only clathrate compound less dense than water ice.

3.4 Stability of clathrate hydrates

Clathrate hydrate stability is affected by the nature and the partial pressure of guest gas(es) as well as the presence of inhibitors such as ammonia, salts and alcohols. The phase diagrams of clathrates all have the particularity of presenting a lower quadruple point Q_1 where ice, liquid water, clathrate and gaseous phases coexist. This specific point is generally located near 273 K since the solubility of clathrate formers in water is usually too small to significantly affect the freezing point of water (Sloan and Koh, 2007). The existence of an upper quadruple point Q_2 where the liquid water, gaseous, clathrate and liquefied gas phases coexist will be determined by the fact that the guest gas is liquefiable above 273 K. The guest species with a critical point far below Q_1, such as methane and nitrogen (critical temperatures of 191 and 126 K respectively), therefore present only one quadruple point. The quadruple points are specific to a given system and are listed in Table 3.3 for the species relevant to this study.

Various phase diagrams corresponding to systems with one and two quadruple points or with inhibitors are schematically represented in Fig. 3.6 where I, L_W, H, V and L_{HC} stand for ice, liquid water, clathrate hydrate, vapor and liquid hydrocarbon, respectively. The CH_4 + H_2O system with one quadruple point is represented in Fig. 3.6a. The three-phase lines delimit areas where the two phases common to these lines are stable. Clathrate hydrate formation can thus occur at lower temperatures and higher pressures to the left of their stability limit represented

Table 3.3: Quadruple points of clathrate hydrates relevant to this study.

Guest	T (K), P (MPa) at Q_1	T (K), P (MPa) at Q_2
CH_4[a]	272.9, 2.563	No Q_2
CO_2[a]	273.1, 1.256	283.0, 4.499
N_2[a]	271.9, 14.338	No Q_2
Ar[b]	272.2, 8.267	No Q_2
H_2[c]	263.85, 105.0	No Q_2

[a] Sloan and Koh (2007)
[b] Nagashima et al. (2018)
[c] Chapoy et al. (2010)

by the I-H-V and L_W-H-V lines. For a system with an upper quadruple point, such as CO_2 + H_2O, the stability region of clathrates is bounded beyond Q_2 by the L_W-H-L_{HC} line, almost vertical due to the relative incompressibility of the three phases, as can be seen in Fig. 3.6b. Therefore, Q_2 is often approximated as the maximum temperature of clathrate hydrate formation (Sloan and Koh, 2007). When a mixture of hydrocarbons is present, the L_W-V-L_{HC} line becomes an area and the quadruple point Q_2 evolves consequently into a line. The presence of inhibitor (e.g., methanol in Fig. 3.6c) in the free water phase decreases the ice - liquid water transition moving the quadruple point Q_1 towards lower temperatures with a shift that depends on the inhibitor concentration. The stability limit of clathrate hydrates is thus shifted approximately parallel (on a plot of ln P versus T) towards lower temperature and higher pressure.

The dissociation curves of the different clathrates considered in this work are represented in Fig. 3.7 together with the phase diagram of H_2O. The experimental equilibrium data derive from Deaton and Frost (1946); Larson (1955); Marshall et al. (1964); Jhaveri and Robinson (1965); Takenouchi and Kennedy (1965); Robinson et al. (1967); Miller and Smythe (1970); Falabella (1975); Holder et al. (1980); Ng and Robinson (1985); Makogon and Sloan (1994); Kuhs et al. (2000); Yasuda and Ohmura (2008); Mohammadi and Richon (2010, 2011). The stability curve of H_2 clathrate is not shown in Fig. 3.7 because, as mentioned in section 3.2, they cannot form at low pressure. The nature of the guest gas influences the pressure of the lower quadruple point, which is connected to the water triple point (273.16 K, 0.62 kPa) via the I-L_W-V line denoting the transition between liquid water and ice. It is interesting to note that carbon dioxide clathrate forms at lower pressure than methane clathrate below 273 K.

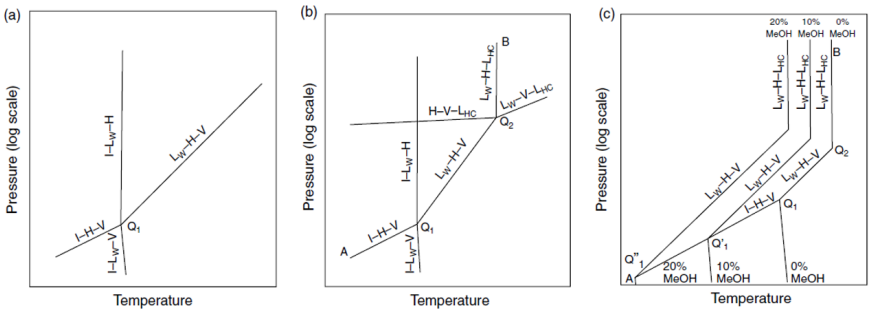

Figure 3.6: Phase diagrams for different systems (Sloan and Koh, 2007). (a) Methane + water system. (b) Carbon dioxide + water system with an upper quadruple point. (c) System with two quadruple points and methanol (CH_3OH, often abbreviated MeOH) as inhibitor. The L_W-H-V line is shifetd towards higer pressure and lower temperature (that is to the left of the diagram) with the increase of methanol concentration in the free water phase.

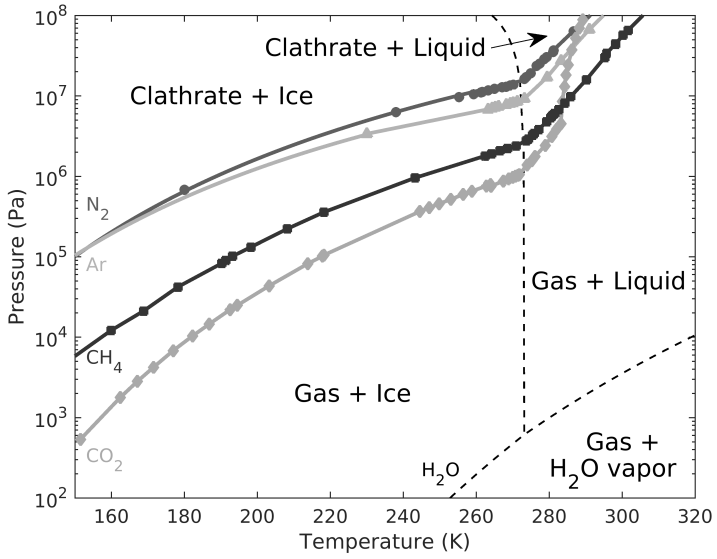

Figure 3.7: Phase diagram of H_2O (black dotted line) and stability curves of CH_4, CO_2, N_2 and Ar clathrate hydrates.

3.4.1 Clathrate stability zone

The first step in establishing where clathrate hydrates occur is to determine the clathrate stability zone (CSZ), the region where temperature-pressure conditions required for their formation are met. An example

of CSZ for methane clathrate in permafrost is given in Fig. 3.8 where the pressure was converted to depth assuming hydrostatic conditions. The first intersection of the solid (clathrate stability limit) and dashed (geothermal gradient) lines marks the top of the CSZ, which is typically located at depths between 100 and 300 m. Note that clathrates with the shallower stability depth are the most easily destabilized since they are at the phase boundary. The second crossing point indicates the base of the CSZ, where the temperature becomes too warm for clathrates to remain stable. On Mars, due to colder surface and subsurface temperatures, the geothermal gradient on Fig. 3.8 will be shifted to the left, extending therefore the cryosphere and the clathrate stability zone.

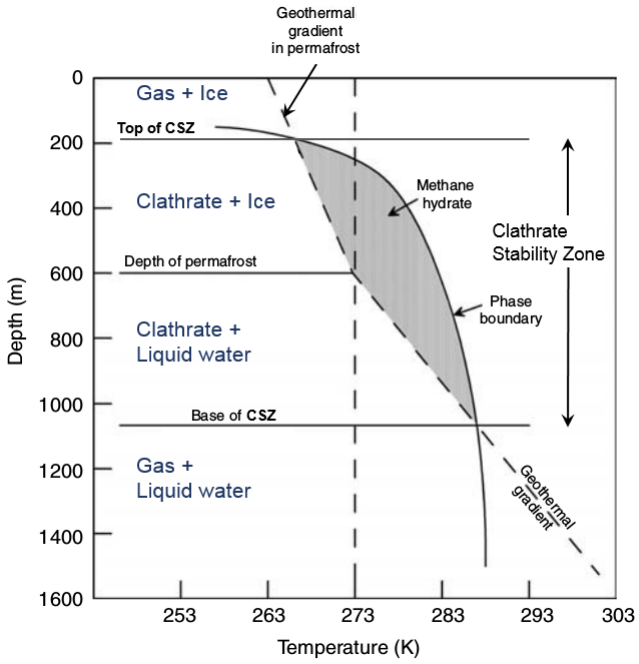

Figure 3.8: Methane clathrate stability zone in permafrost. (Adapted from Sloan and Koh (2007)).

Although the clathrate stability zone can correspond to large subsurface areas, that does not mean that clathrate hydrates are actually present in these regions. Indeed, methane availability is the most critical parameter controlling the occurrence of clathrates. Defining global stability regions based only on temperature-pressure conditions gives thus an upper bound to possible clathrate occurrences.

3.5 Formation and dissociation processes

The formation of clathrate hydrates has many similarities with crystallization; i.e., it can be divided in two consecutive steps: nucleation followed by growth. The nucleation process is stochastic and therefore unpredictable. It is typically initiated at the water-gas interface or on solid substrates (heterogeneous nucleation) from a metastable supercooled and supersaturated fluid. During this phase, small clusters of water and gas grow to achieve the critical size required to initiate the growth phase and expand spontaneously. However, supersaturation does not always guarantee clathrate formation. Even if temperature and pressure conditions are thermodynamically favorable, there is a given degree of supersaturation below which spontaneous crystallization is unlikely. During the growth phase, two processes become of major importance: mass transfer during which components are adsorbed on the growing crystal surface and heat transfer related to the exothermic nature of clathrate formation.

On Earth, methane clathrates can form following three ways (Sloan and Koh, 2007): in situ formation from biotic methane generally associated to sparse reservoirs (3% of the pore volume under the best conditions; Klauda and Sandler (2005)) dispersed over wide areas, formation from free gas (perhaps recycled gas if it comes from dissociated clathrates) moving upward, and formation from methane-saturated (or supersaturated) rising fluids. Massive and localized clathrate deposits are related to faults and fractures that act as conduits for methane emitted from deep sources. The accumulation of gas in relatively porous subsurface layers can also lead to rich-clathrate deposits (70-80% of the pore volume; Sloan and Koh (2007)).

On Mars, assuming that methane is generated at depth in the crust (by serpentinization followed by Fischer-Tropsch reactions for example), its path to the atmosphere will cross several boundaries. When methane gas bubbles and methane-saturated fluids rise through soil layers following preferential pathways along faults and fractures, they reach the CSZ where clathrate hydrates should form at the gas-water interface under the form of a thin film along the surface of the bubble. At the transition between liquid water and water ice, the rising methane-rich fluid is expected to interact with the pre-existing permafrost layer and to freeze itself, so that CH_4 clathrates are incorporated into the water ice matrix under the form of small inclusions (Chassefière and Leblanc, 2011b). The accumulation of clathrate-coated bubbles in area of high porosity and beneath less permeable layers may also result in formation of massive deposits (Elwood Madden et al., 2009). If methane is produced contin-

uously in the subsurface, the base of the martian cryosphere could be gradually enriched in small amounts of methane clathrate hydrate and the CH_4 diffusion through the overlying ice would expand the methane clathrate hydrate reservoir with time. Therefore, methane clathrates could eventually form near the surface at the top of their stability zone, although formation rates at these shallow depths would be significantly lower than those at the base of the CSZ (Gainey and Elwood Madden, 2012).

Clathrate dissociation is an endothermic process in which heat must be supplied in order to break the hydrogen bonds as well as the van der Waals interaction forces between guest and host lattice. Destabilization is triggered by heating, depressurization and/or thermodynamic inhibitor injection. Small and disseminated clathrate reservoirs are easily decomposed, while massive deposits undergo a much slower dissociation, on the one hand because of a low surface to volume ratio (Sloan and Koh, 2007), and on the other hand because the "self-preservation" effect where a protective ice layer forms from dissociated clathrates and prevents the rest from further dissociation (Yakushev and Istomin, 1992). It is interesting to notice that the dissociation of methane clathrate in ice and gas requires less heat than its decomposition in water and gas (see Table 3.2).

3.6 Clathrate hydrates in the Solar System

For the moment, no direct observation of clathrates has been made outside the Earth and their existence on Solar System bodies is inferred based on our current knowledge of the temperature-pressure conditions and gases present on the moons and planets.

3.6.1 Comets

Delsemme and Swings (1952) suggested that clathrate hydrates could exist in cometary nuclei and would be destabilized with their approach to perihelion. Indeed, the presence of these compounds would adequately explain the similar sublimation rate of the various volatile species observed in cometary spectra. In addition, nucleus models showed that long-period comets as well as short-period comets could be formed by clathrate hydrates (Marboeuf et al., 2008, 2009). Recently, coma measurements by the Rosetta mission observing 67P/Churyumov-Gerasimenko provided outgassing pattern that would be consistent with gas release from either amorphous ice or clathrates, or both (Luspay-Kuti et al., 2016).

3.6.2 Mars

It was established, as early as 1970, that CO_2 clathrate was thermodynamically stable in the polar cap on Mars (Miller and Smythe, 1970). Max and Clifford (2000) suggested the existence of methane clathrate in the martian subsurface four years before the first reported detection of this gas in the planet's atmosphere. Stability models suggest that methane clathrates could have remained stable from several meters deep in polar regions and from several tens of meters deep in equatorial regions (Chastain and Chevrier, 2007; Root and Elwood Madden, 2012). Methane clathrate reservoirs might be very localized and occupy only a small part of the martian cryosphere as their presence depends on the availability of methane and water. In addition, methane could be trapped in clathrate hydrates as a minor compound with other gas species. In the binary CO_2-CH_4 system, increasing the CO_2 content and therefore decreasing the amount of CH_4 trapped in clathrates reduces the formation pressure and allows clathrate hydrates to form at shallower depth (Chastain and Chevrier, 2007). Thomas et al. (2009) studied the composition of clathrates formed from a gas phase including methane and the Mars' atmosphere main components CO_2, N_2, Ar and showed that the trapping of CH_4 is efficient only when the initial gas phase is enriched in methane. These results suggest that CH_4-rich clathrate hydrates cannot be formed from the current planet's atmosphere given the very low abundance of methane on Mars. If they are present in the martian crust, CH_4-rich clathrates should have been formed in contact with a subsurface source or an early martian atmosphere, richer in methane (Chastain and Chevrier, 2007; Thomas et al., 2009).

Although climate change due to obliquity variations affects the CSZ and leads to the destabilization of near-surface clathrates (Prieto-Ballesteros et al., 2006; Root and Elwood Madden, 2012; Kite et al., 2017), some of them may have been preserved over geologic time scales as metastable reservoirs due to slow dissociation and diffusion kinetics (Root and Elwood Madden, 2012). These methane reservoirs could thus be located outside their present-day stability zone in the martian subsurface at depths, closer to the surface, corresponding to past stability zones associated with larger obliquities and colder surface temperatures at the equator of the planet. Finally, the reader is referred to section 2.4 where other methane clathrate studies are mentioned, while thermodynamic stability will be discussed in more details in the following chapter.

3.6.3 Outer Solar System

In icy satellites, multicomponent clathrate hydrates could either constitute parts of the satellite's building blocks and trap primordial volatiles from the protosolar nebula or be currently formed from gases generated at depth in these outer Solar System bodies (Mousis et al., 2015). The internal oceans of Enceladus and Europa provide proper thermodynamic conditions for clathrate formation. It has been suggested that the water-rich plumes bursting from the south polar region of Enceladus, as observed by the Cassini spacecraft, could be generated from the decomposition of clathrates exposed to near-vacuum conditions following episodic formation of fractures (Kieffer et al., 2006). On Europa, clathrates of CH_4, CO_2, H_2S and SO_2 could exist in most of the icy crust and the subsurface ocean and would float or sink depending on the salinity (Prieto-Ballesteros et al., 2005). Clathrate hydrates could be present on other moons such as Ganymede and Triton (Mousis et al., 2015). As for comets, Kuiper Belt Objects, including Pluto, might have formed from the agglomeration of clathrates and pure ices in the protosolar nebula. In addition, thermodynamic equilibrium calculations have shown that noble gas-rich clathrates may exist on Pluto's surface (Mousis et al., 2013b).

Titan

Methane clathrates are still considered to play a major role on Saturn's largest moon, Titan, as they could contribute significantly to the replenishment of atmospheric methane. Laboratory experiments have demonstrated that CH_4 clathrates can be formed under the temperature-pressure conditions of Titan (Choukroun et al., 2010b), while a coupled thermal-orbital model has shown that clathrates located within an icy shell above an ammonia-enriched water ocean experience episodic outgassing and represent the most likely source of atmospheric methane (Tobie et al., 2006). Moreover, ammonia being an important thermodynamic inhibitor, its interaction with clathrates in the icy crust is expected to induce methane outgassing as well (Choukroun et al., 2010b). However, there is a lack of experimental data regarding clathrate stability in the presence of ammonia. In this frame and during a 3-month internship at Jet Propulsion Laboratory, we performed low-temperature Raman experiments to study the dissociation temperature of tetrahydrofuran (THF) clathrates (often used as an ambient-pressure proxy for methane clathrates) over a wide range of ammonia concentrations from 0 to 25 wt%. Our results suggest that, similarly to its effect on the melting point of water ice, ammonia lowers the dissociation point of THF

clathrate hydrates, which show a "liquidus-like" behavior with a eutectic temperature of about 203.6 K (Vu et al., 2014). This estimated temperature being smaller than those predicted within Titan's icy layer, the partial dissociation of methane clathrates via interactions with ammonia can thus take place easily and may contribute to outgassing from the interior.

3.7 Summary

There are three main clathrate structures among which cubic structures I and II are the most common. The type of structure that crystallizes depends mainly on the guest size. For example, methane and carbon dioxide form sI clathrate, whereas nitrogen and argon are sII clathrate formers. On the other hand, crystal structure determines equilibrium temperatures and pressures for the clathrate phase.

Because all common clathrate structures consist of at least 85% water, many of clathrate physical properties are similar to those of water ice Ih. However, the differences in mechanical strength, thermal conductivity and density may play an essential role in geologic processes of planetary environments. Regarding clathrate formation, it is achieved via nucleation followed by growth, but these two phenomena are still challenging to measure and model mainly because of their stochastic nature. In contrast, clathrate dissociation can be predicted in most cases and is caused by heating, depressurization and/or thermodynamic inhibitor injection.

The first step in establishing where methane clathrates occur is to determine the clathrate stability zone. However, this area only gives an upper bound to possible clathrate occurrences, methane availability being the most critical parameter controlling the actual presence of clathrate hydrates. In addition to Mars, clathrates have been proposed to exist in other Solar System bodies such as icy satellites, comets and Kuiper Belt Objects.

Chapter 4

Models

Contents

4.1 Methane migration in the martian crust and outgassing scenarios 52
4.2 Thermodynamic modelling of clathrates . . . 53
4.3 Thermal model 65
4.3.1 Determination of surface temperature on slopes 65
4.3.2 Subsurface temperature 68
4.4 Transport of gases in porous media 71
4.4.1 Mass transfer versus mass transport 71
4.4.2 Mechanisms of gas transport 72
4.4.3 Advective flux 73
4.4.4 Molecular diffusive flux 74
4.4.5 Bulk diffusive flux 75
4.4.6 Knudsen diffusive flux 75
4.4.7 Effective diffusion coefficient 76
4.4.8 Adsorption 77
4.4.9 Gas transport models 78
4.5 Summary 83

This chapter focuses on the description of models developed to study the stability of clathrate hydrates and the transport of methane in the martian crust. The thermodynamics of the formation or dissociation of clathrates is most often based on the model of van der Waals and Platteeuw (1959), which includes assumptions similar to those used to establish the adsorption theory of Langmuir. Regarding the methane migration, we focused on diffusive transport although several physical processes can be involved. These processes are reviewed in the following section and are described in more details at the end of this chapter.

4.1 Methane migration in the martian crust and outgassing scenarios

Various possible ways of migration and storage for methane in the martian crust and subsequent discharge into the atmosphere are illustrated in Fig. 4.1. During the whole geological history of Mars, methane formation mechanisms could have taken place in the deep subsurface and could still be active nowadays. After its generation, methane would migrate upwards and be either directly released at the surface or trapped in subsurface reservoirs (clathrates, zeolites or sealed traps) where it could eventually accumulate over long time periods before to be episodically liberated during destabilising events. These phenomena leading to surface degassing imply a change in temperature/pressure conditions of the CH_4 reservoirs and are multiple: faulting and landslide generated by seismicity, impact, climatic changes...

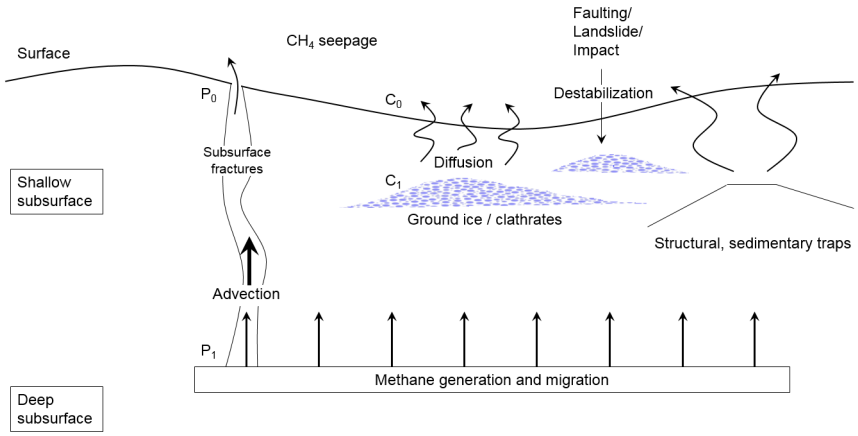

Figure 4.1: Possible scenarios of methane migration and storage in the martian crust and subsequent release into the atmosphere.

When ascending through stratigraphic layers, methane can move via one or several transport mechanisms. Seepage can occur through advection, the main CH_4 transport process on Earth, driven by pressure gradients and permeability and generally associated to fracture networks (Etiope and Oehler, 2019). Therefore, whenever gas pressure increases in subsurface gas pockets or along faults due to decomposition of methane reservoirs for instance or when large variations in pressure above regolith are induced by surface winds, methane may be discharged in the martian atmosphere by advection (Etiope and Oehler, 2019). Another transport mechanism is diffusion, which is mainly controlled by concentration gra-

dients. This process is not efficient on short timescales (Stevens et al., 2017) and short-lived methane plumes related to diffusion should therefore originate from shallow depths.

All the mechanisms of generation, accumulation and migration together control the seepage intensity. In the following, we first describe the storage system modelling.

4.2 Thermodynamic modelling of clathrates

Three main models have been used in the litterature to study clathrate hydrate stability and composition on Mars (Chastain and Chevrier, 2007; Thomas et al., 2009; Herri and Chassefière, 2012) and are all based on the statistical thermodynamic method developed by van der Waals and Platteeuw (1959), which requires the following assumptions (Sloan and Koh, 2007):

1. Each cavity can contain at most one guest molecule.
2. The guest molecules interact only with the nearest neighboring host molecules and guest-guest molecule interactions are neglected. That is, the energy of each trapped gas molecule is independent of the number and nature of other guest molecules.
3. The contribution of water molecules to the free energy is independent of the cavity occupancy. This implies that guest molecules do not distort the cage.
4. The interaction between guest and water molecules can be described by a pair potential function, and the cavity can be treated as perfectly spherical.
5. The ideal gas partition function is applicable to guest molecules. That is the rotational, vibrational, nuclear, and electronic energies are not significantly affected by enclathration. This hypothesis implies that guest molecules can freely rotate in the cavities.
6. The laws of classical statistical mechanics are valid and no quantum effects are needed.

We are interested here in the temperature-pressure conditions of the I-H-V (or L_W-H-V) equilibrium curve presented in Fig. 3.6. Thermodynamic equilibrium implies the minimization of the Gibbs energy and the equality of chemical potentials of water μ_w in the ice phase α (or liquid phase L) and in the clathrate hydrate phase H:

$$\mu_w^H = \mu_w^{L,\alpha} \tag{4.1}$$

For convenience, this equalization can be rewritten in terms of chemical potential differences by introducing a hypothetical phase β that corresponds to a clathrate with empty cavities:

$$\left.\begin{array}{l} \Delta\mu_w^{\beta-H} = \mu_w^{\beta} - \mu_w^{H} \\ \Delta\mu_w^{\beta-L,\alpha} = \mu_w^{\beta} - \mu_w^{L,\alpha} \end{array}\right\} \rightarrow \Delta\mu_w^{\beta-H} = \Delta\mu_w^{\beta-L,\alpha} \tag{4.2}$$

where μ_w^{β} is the chemical potential of water in the empty clathrate. $\Delta\mu_w^{\beta-H}$ is evaluated via statistical thermodynamics, while $\Delta\mu_w^{\beta-L,\alpha}$ is determined from classical thermodynamics.

Modelling $\Delta\mu_w^{\beta-H}$

Following the model of van der Waals and Platteeuw (1959), this term can be written as a function of the occupancy fraction $\theta_{G,i}$ of a species G in a given type i of cage (i = small or large) for a given type of clathrate structure (I or II) as:

$$\Delta\mu_w^{\beta-H} = -RT\sum_i \nu_i \ln(1 - \sum_G \theta_{G,i}) \tag{4.3}$$

where R is the universal gas constant, T is the thermodynamic temperature and ν_i is the number of cavities of type i per water molecule in the clathrate unit cell. The occupancy fraction is comparable to the fractional coverage of the adsorbed monolayer in the Langmuir gas adsorption theory and is defined as:

$$\theta_{G,i} = \frac{C_{G,i}(T) f_G(T,P)}{1 + \sum_J C_{J,i}(T) f_J(T,P)} \tag{4.4}$$

where $f_G(T,P)$ is the fugacity of the guest G in the gas or liquid phase. The Langmuir constant $C_{G,i}(T)$ is analogous to the equilibrium Langmuir adsorption constant and characterizes the attractiveness of the cavity i for a species G. For a given value of the fugacity, the species with the highest Langmuir constant is the most strongly enclathrated guest in a cavity. Therefore, the gas molecules with an optimal guest/cavity size ratio, as mentioned in Section 3.2, have higher values of $C_{G,i}(T)$. The latter is defined by the following equation:

$$C_{G,i}(T) = \frac{1}{k_B T} \int\int \exp\left(\frac{-W_{G,i}(\boldsymbol{r}, \boldsymbol{\Omega})}{k_B T}\right) d\boldsymbol{r} d\boldsymbol{\Omega} \tag{4.5}$$

where k_B is the Boltzmann constant and $W_{G,i}$ is the interaction potential energy experienced by the guest molecule G included in the cavity i. This interaction is function of the position $\boldsymbol{r}$ and orientation $\boldsymbol{\Omega}$ vectors of the guest molecule in the cage. If the cavity is assumed to be perfectly spherical and the guest molecule can freely rotate in the cage, the Langmuir constant can be written as:

$$C_{G,i}(T) = \frac{4\pi}{k_B T} \int_0^{R_c} \exp\left(\frac{-W_{G,i}(r)}{k_B T}\right) r^2 dr \tag{4.6}$$

where R_c is the radius of the spherical cavity and $W_{G,i}(r)$ is the spherically averaged potential energy between the guest molecule and the cavity. The interaction potential used in the original work by van der Waals and Platteeuw (1959) is based on the Lennard-Jones 6-12 pair potential. However, McKoy and Sinanoğlu (1963) suggested to derive the interaction potential of Equation 4.6 from the Kihara potential $\Phi_K(r)$, better adapted for both larger and nonspherical molecules. This potential is commonly used in clathrate hydrate stability calculations and is given by:

$$\Phi_K(r) = 4\epsilon \left(\left(\frac{\sigma}{r-2a}\right)^{12} - \left(\frac{\sigma}{r-2a}\right)^{6} \right) \quad \text{for } r > (a_G + a_w) \tag{4.7a}$$

$$\Phi_K(r) = \infty \quad \text{for } r \leq (a_G + a_w) \tag{4.7b}$$

where σ is the cores distance at zero potential ($\Phi_K = 0$, attractive and repulsive interactions are equal), a is the radius of the spherical core (the subscript G refers to the guest, while w refers to water) and ϵ is the maximum attractive potential (at $r = \sqrt[6]{2}\sigma$). Averaging the pair potentials of Equation 4.7a and b between the guest and each water molecule at the surface of the spherical cage leads to the expression of the cell potential:

$$W_{G,i}(r) = 2z\epsilon \left[\frac{\sigma^{12}}{R_c^{11} r} \left(\delta^{10} + \frac{a}{R_c}\delta^{11} \right) - \frac{\sigma^6}{R_c^5 r} \left(\delta^4 + \frac{a}{R_c}\delta^5 \right) \right] \tag{4.8}$$

with

$$\delta^N = \frac{1}{N} \left[\left(1 - \frac{r}{R_c} - \frac{a}{R_c}\right)^{-N} - \left(1 + \frac{r}{R_c} - \frac{a}{R_c}\right)^{-N} \right] \tag{4.9}$$

where z is the coordination number of the cavity. The parameters R_c and z are specific to the type of cage and the clathrate structure. The

Kihara parameters ϵ, a and σ are specific to the guest molecule and are determined by a linear regression fitted to experimental data. The set of Kihara parameters used in the present work is given in Table 4.1.

It is important to note that the Kihara parameters remain adjustable and depend on the experimental equilibrium data of simple clathrate hydrates. The predicted relative abundances of guest species in clathrates greatly depend on the choice of those parameters. Here, we chose to use parameters that have been optimized by Herri and Chassefière (2012) in a study where they fitted the model of van der Waals and Platteeuw (1959) to compare the deviation from experimental data of pure clathrate hydrates at temperatures relevant to Mars. Indeed, calculations in temperature and pressure conditions outside the range for which the Kihara parameters have been determined can lead to inaccurate clathrate compositions.

Table 4.1: Kihara parameters used in the present study. These parameters are derived from Herri and Chassefière (2012) for CH_4, CO_2, N_2 and Ar and from Strobel et al. (2009) for H_2.

Molecule	ϵ/k_B (K)	σ (Å)	a (Å)
CH_4	166.36	3.0500	0.3834
CO_2	178.21	2.8730	0.6805
N_2	133.13	3.0993	0.3526
Ar	174.14	2.9434	0.1840
H_2	80.424	3.07838	0.1973

Finally, note that the upper limit for the integral in Equation 4.6 is often written R_c but should be presented as $R_c - a_G$ instead (Sloan and Koh, 2007). Indeed, this latter limit does physically make sense and corresponds to the spherical core of the guest molecule in contact with the edge of the water cavity. Moreover, if care is not taken, problems can appear in the numerical integration to calculate the Langmuir constant because of the division by an r term in Equations 4.8 and 4.9 when $r = 0$ and $r = R_c - a_G$ respectively. Following Pratt et al. (2001) and applying L'Hospital's rule, we obtain:

$$\lim_{r\to 0} W_{G,i}(r) = 2z\epsilon \left[\frac{\sigma^{12}}{R_c^{11}} \left(\delta'^{10} + \frac{a}{R_c}\delta'^{11} \right) - \frac{\sigma^6}{R_c^5} \left(\delta'^4 + \frac{a}{R_c}\delta'^5 \right) \right] \quad (4.10)$$

with

$$\delta'^N = \frac{2}{R_c} \left(1 - \frac{a}{R_c} \right)^{-(N+1)} \quad (4.11)$$

This leads to a finite value of the cell potential. At $r = 0$, using Equations 4.10 and 4.11 will thus give a finite number for the exponential term in Equation 4.6, while the integrand will be zero (because of the r^2 term). Applying the same method for $r = R_c - a_G$, we get:

$$\lim_{r \to R_c - a_G} W_{G,i}(r) = +\infty \tag{4.12}$$

At $r = R_c - a_G$, the exponential term in the Langmuir constant expression will thus tend to zero, leading again to an integrand equal to zero. Nevertheless, to be sure to eliminate all possibilities of divergence in the calculations when evaluating the integrand of Equation 4.6 at $r = R_c - a_G$, Pratt et al. (2001) suggested to simply evaluating the integral from 0 to $R_c - a_G - \xi$, where ξ is a very small number (0.0001 Å).

Modelling $\Delta\mu_w^{\beta-L,\alpha}$

Following Holder et al. (1980), the chemical potential difference between water in the hypothetical empty lattice and water in either the ice phase ($T \leq 273.15$ K) or the liquid phase ($T \geq 273.15$ K) can be expressed as:

$$\begin{aligned}\left(\frac{\Delta\mu_w^{\beta-L,\alpha}}{RT}\right)_{(T,P)} = \left(\frac{\Delta\mu_w^{\beta-L,\alpha}}{RT}\right)_{(T_0,P_0)} - \int_{T_0}^{T} \frac{\Delta h_w^{\beta-L,\alpha}}{RT^2} dT \\ + \int_{P_0}^{P} \frac{\Delta v_w^{\beta-L,\alpha}}{RT} dP - \ln(a_w^L)\end{aligned} \tag{4.13}$$

where the reference conditions T_0 and P_0 are generally taken as $T_0 = 273.15$ K and $P_0 = 1$ bar. The temperature dependence of the enthalpy difference is given by:

$$\Delta h_w^{\beta-L,\alpha} = \Delta h_w^{\beta-L,\alpha}(T_0) + \int_{T_0}^{T} \Delta C_p^{\beta-L,\alpha} dT \tag{4.14}$$

where the variation of the heat capacity is approximated by:

$$\Delta C_p^{\beta-L,\alpha} = \Delta C_p^{\beta-L,\alpha}(T_0) + b^{\beta-L,\alpha}(T - T_0) \tag{4.15}$$

where $b^{\beta-L,\alpha}$ is a constant. The volume difference $\Delta v_w^{\beta-L,\alpha}$ is assumed to be independent of pressure. The last term of the second member of Equation 4.13 involves the activity of water a_w^L, which is defined by:

$$a_w^L = \gamma_w \, x_w = \frac{f_w^L}{f_w^0} \tag{4.16}$$

where γ_w is the activity coefficient of water, x_w is the mole fraction of water in the liquid phase and f_w^L and f_w^0 are the water fugacities in the aqueous phase and in pure water, respectively. If we consider the liquid phase as ideal, the activity coefficient γ_w can be set to a fixed value of 1. The mole fraction of water is then estimated by determining the fraction of dissolved gas in the liquid phase: $x_w = 1 - x_G$. The latter is usually small due to the low solubility of clathrate formers in water. For the ice phase, the activity of water is unity, making the term $\ln(a_w^L)$ in Equation 4.13 equal to zero. Thermodynamic reference parameters for sI and sII clathrates when $T \leq 273.15$ K are reported in Table 4.2.

Table 4.2: Thermodynamic reference properties for structure I and II clathrate hydrates: $T_0 = 273.15$ K, $P_0 = 1$ bar.

	Structure I	Structure II	Ref.
$\Delta\mu_w^{\beta-\alpha}$ (T_0,P_0) (J mol^{-1})[a]	1287	1068	Handa and Tse (1986)
$\Delta h_w^{\beta-\alpha}$ (T_0) (J mol^{-1})	1170	1294	Anderson et al. (2005)
$\Delta v_w^{\beta-\alpha}$ (T_0) (m^3 mol^{-1})	3.0×10^{-6}	3.4×10^{-6}	Anderson et al. (2005)
$\Delta C_p^{\beta-\alpha}$ (J mol^{-1} K^{-1})	$0.565 + 0.002\,(T - T_0)$		Holder et al. (1980)

[a] Superscripts/subscripts: w = water, β = empty clathrate lattice, α = ice phase.

Accurate values for the thermodynamic reference properties used in the statistical mechanical model of van der Waals and Platteeuw (1959) are essential. Unfortunately $\Delta\mu_w^0$ and Δh_w^0 have been found to take a wide range of values, due to the difficulties in determining these quantities experimentally, and have been used rather to fit experimental data than to make exact predictions (Cao et al., 2001; Herri and Chassefière, 2012).

Final expression

By combining Equations 4.2, 4.3 and 4.13, we obtain the expression that predicts the equilibrium pressure of clathrates at a given temperature and vice versa:

$$-RT\sum_i \nu_i \ln(1 - \sum_G \theta_{G,i}) = T\,\frac{\Delta\mu_w^{\beta-L,\alpha}}{T_0} - T\int_{T_0}^{T}\frac{\Delta h_w^{\beta-L,\alpha}}{T^2}dT + \int_{P_0}^{P}\Delta v_w^{\beta-L,\alpha}dP - RT\ln\left(a_w^L\right) \tag{4.17}$$

A typical algorithm to find the pressure formation of clathrates from the initial mole fractions of different components in a given gas mixture at

a given temperature is shown in Fig. 4.2. First, the Langmuir constants for each component in all cavities of both clathrate structures I and II are calculated via Equation 4.6. According to the input temperature, a first estimation of the formation pressure is made and used to determine the fugacity of every component in the gaseous phase. The chemical potential differences are then calculated (Equations 4.3 and 4.13) and compared. If their values are close enough, the estimated pressure was the good one. Otherwise, the pressure is adjusted and the fugacity, $\Delta\mu_w^{\beta-H}$ and $\Delta\mu_w^{\beta-L,\alpha}$ are calculated again with this new pressure. This procedure is repeated until the chemical potential differences correspond. Once the formation pressure is found for sI and sII clathrates, the structure that actually crystallizes is considered to have the lowest formation pressure. This algorithm is commonly used in programs predicting the thermodynamics of stable clathrate structures such as CSMHYD (Colorado School of Mines, HYDrates), which has been developed to study clathrate hydrates on Earth (Sloan and Koh, 2007). This program is executable and allows the user to enter the number, nature and mole fractions of the different components in the gas phase. Then, it computes the equilibrium pressure at the temperature specified by the user, with or without inhibitor(s) in the aqueous phase (a salinity increase results in a decrease of water activity). In addition, standard outputs include equilibrium phases and their compositions, crystal structure and fractional occupancy.

Although of great precision, CSMHYD is not suitable to the temperature conditions prevailing at high latitude on Mars because the method does not converge for conditions far from reference conditions (T_0 = 273.15 K, P_0 = 1 bar). Consequently, Chastain and Chevrier (2007), who investigated composition and stability of binary CO_2-CH_4 clathrates in the martian subsurface using this program, were not able to calculate the composition of clathrate hydrates formed below 173K. Moreover, the CSMHYD program has a limited list of available species and does not allow to consider all the components of the martian atmosphere such as argon. Thomas et al. (2009) determined the composition of mixed CO_2-CH_4-N_2-Ar clathrates as a function of temperature and initial gas phase composition using a hybrid model based on the work of van der Waals and Platteeuw (1959) and on available experimental dissociation curves. This approach allows to include minor compounds in the martian atmosphere and does not suffer from low temperature restriction. As mentioned previously, Herri and Chassefière (2012) used the same kind of method fitting the model of van der Waals and Platteeuw (1959) and comparing the deviation from experimental data at low temperature. They implemented in their software called GasHydDyn (Java language)

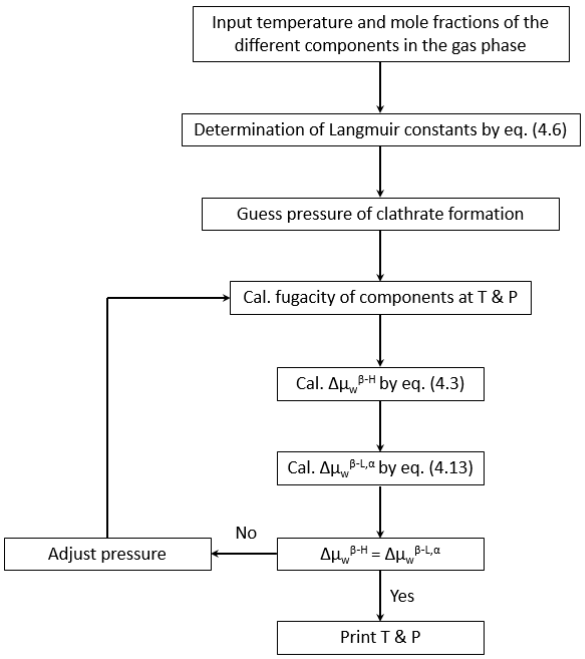

Figure 4.2: Typical algorithm to determine formation conditions of clathrate hydrates with the model of van der Waals and Platteeuw (1959).

a minimization algorithm to determine Kihara and reference parameters from experimental data base (pressure, temperature, gas and clathrate compositions) or inversely. In each case, clathrate compositions have been determined at the dissociation pressure.

In this study, we follow an approach similar to Thomas et al. (2009) where the dissociation pressure P_{mix}^{diss} of a multiple guest clathrate is calculated from the dissociation pressures of simple guest clathrates as (Lipenkov and Istomin, 2001):

$$P_{mix}^{diss} = \left(\sum_G \frac{x_G}{P_G^{diss}} \right)^{-1} \tag{4.18}$$

where x_G is the molar fraction of species G in the initial gas phase. The dissociation pressure P_G^{diss} of a simple clathrate of guest species G follows an Arrhenius law (Miller, 1961):

$$\log(P_G^{diss}) = A + \frac{B}{T} \tag{4.19}$$

where P_G^{diss} is expressed in Pa and T is the temperature in K. The

constants A and B fit to the experimental data presented in Fig. 3.7 and are listed in Table 4.3. Most of these constants are valid below the quadruple point Q_1 of clathrates (I-H-V equilibrium curve) as this is the stability region investigated in this work. For H_2 clathrate, given the lack and considerable dispersion in the experimental data below the quadruple point (T = 263.85 K), we decided to study the influence of H_2 trapping in methane clathrate only over a temperature range from 263.85 K to 273.15 K. Experimental dissociation pressures obtained between Q_1 and 269.15 K for the system H_2 + H_2O (Chapoy et al., 2010) have thus been fitted to obtain A and B. Moreover, as the base of clathrate stability zone is investigated for simple clathrate of methane, A and B above Q_1 have been determined as well for CH_4. Fig. 4.3 compares the dissociation pressure computed with this approach and those obtained with CSMHYD and GasHydDyn for a mixed clathrate formed from an initial gas phase with 50% of CH_4, 30% of CO_2 and 20% of N_2.

Table 4.3: Parameters A and B (K) required in Equation 4.19 to calculate the dissociation pressure of simple clathrates.

Molecule	A	B (K)	T range
CH_4	9.65	-895.9	$\leq Q_1$
CH_4	21.46	-4124.4	$\geq Q_1$
CO_2	10.13	-1116.9	$\leq Q_1$
N_2	9.74	-702.57	$\leq Q_1$
Ar	9.24	-630.86	$\leq Q_1$
H_2	19.70	-3080.7	$\geq Q_1$

Equation 4.18 gives a very good estimation of the dissociation pressure. It can be seen in Fig. 4.3 that this method provides similar results to CSMHYD and GasHydDyn at temperature close to 270 K. At lower temperature, the pressure slightly differs from that predicted by the two stability models, which also deviate from each other. However, P_{mix}^{diss} remains in the region delimited by CSMHYD and GasHydDyn, showing the validity of the method. Once the equilibrium pressure is known, the relative abundance of a species G in a clathrate hydrate is given by:

$$x_G^H = \frac{b_s \theta_{G,s} + b_l \theta_{G,l}}{b_s \sum_J \theta_{J,s} + b_l \sum_J \theta_{J,l}} \tag{4.20}$$

where the sum at the denominator takes into account all the species in the gas phase and b_s and b_l are the number of small and large cavities per unit cell respectively. The occupancy fraction $\theta_{G,i}$ is calculated via Equation 4.4 where the fugacities and Langmuir constants are determined using

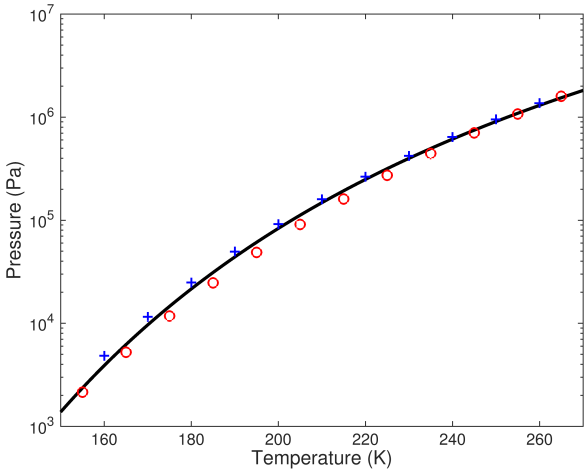

Figure 4.3: Dissociation pressure as a function of temperature for a mixed clathrate formed from an initial gas phase with 50% of CH_4, 30% of CO_2 and 20% of N_2. The calculations were done with the approach described above (black curve), the CSMHYD program (crosses) and the GasHydDyn software (circles).

the Peng-Robinson equation of state and the Equation 4.6, respectively. Although the approach based on Equation 4.18 does not predict which clathrate structure will preferably be formed and makes the composition calculations for both structures I and II necessary for each application, it is quite simple to be implemented in our subsurface model, described in the next section.

Finally, it is important to note that the assumed spherical symmetry of the interaction potential can be questionable and may not accurately describe the interaction between enclathrated and water molecules. As a result, it may lead to the evaluation of erroneous relative abundances of gas species in clathrate hydrates. Some works have thus focused on the evaluation of proper guest-clathrate interaction potentials with parameters directly deduced from ab initio quantum mechanical calculations (Klauda and Sandler, 2002, 2003; Sun and Duan, 2005). Recently, Lakhlifi et al. (2015) proposed a van 't Hoff law expression of Langmuir constants where parameters have been determined using a pairwise atom-atom Lennard-Jones and a site-site electrostatic potentials to calculate the guest-clathrate interaction in an anisotropic environment:

$$C_{G,i}(T) = U_{G,i} \exp\left(\frac{V_{G,i}}{T}\right) \tag{4.21}$$

where U (Pa^{-1}) and V (K) are constant parameters listed in Table 4.4. The model of Lakhlifi et al. (2015) takes into account all the external degrees of freedom of the guest and water molecules and considers explicitly the effect of water molecules beyond the trapping cage: calculations were made over the first four and three hydration shells for sI and sII clathrates, respectively, to ensure a good convergence of the results (Thomas et al., 2010). Equation 4.21 can be applied in the temperature range 50 K - 300 K.

Table 4.4: Parameters $U_{G,i}$ (Pa^{-1}) and $V_{G,i}$ (K) used in Equation 4.21 to calculate the Langmuir constants for simple guest clathrate hydrates. These parameters are derived from Lakhlifi et al. (2015).

Structure type-cage size	sI-small cage	sI-large cage	sII-small cage	sII-large cage
Guest species G	$U_{G,i}$ $V_{G,i}$	$U_{G,i}$ $V_{G,i}$	$U_{G,i}$ $V_{G,i}$	$U_{G,i}$ $V_{G,i}$
CH_4	8.3453×10^{-10} 2901.747	116.6313×10^{-10} 2959.901	5.4792×10^{-10} 2546.660	829.8039×10^{-10} 2629.194
CO_2	7.7765×10^{-12} 2976.629	520.5579×10^{-12} 4674.690	7.9970×10^{-12} 2277.757	$6907.0012 \times 10^{-12}$ 3370.363
N_2	3.9496×10^{-10} 2869.400	25.6897×10^{-10} 2680.372	4.8836×10^{-10} 2679.423	201.3238×10^{-10} 2226.480
Ar	1.5210×10^{-10} 2961.545	7.7829×10^{-10} 2521.758	1.0456×10^{-10} 2977.025	2.4531×10^{-10} 2195.964
H_2	4.7301×10^{-9} 1265.757	16.0695×10^{-9} 1515.721	5.5295×10^{-9} 1203.620	64.0074×10^{-9} 873.259

Langmuir constants computed for sI methane clathrate with both aforementioned methods are presented in Fig. 4.4. Calculations using the Kihara potential show similar Langmuir constants in both types of cage, while the van 't Hoff law expression suggests a more efficient enclathration of CH_4 in the large cage of structure I as its Langmuir constant is higher than in the small cavity at the same temperature.

It is very challenging to discriminate which method (spherically averaged or atom-atom) is the most accurate. While the assumed spherical symmetry of the interaction potential can be uncertain, one may also be suspicious regarding the atom-atom approach, which depends on many parameters such as the number of water shells taken into consideration or the number of chosen interaction sites (Mousis et al., 2010). We compare therefore experimental equilibrium data for simple clathrate hydrates with the dissociation pressure obtained following the algorithm illustrated in Fig. 4.2, in which the second step determining the Langmuir constants is executed for the Kihara potential and atom-atom methods with Equations 4.6 and 4.21, respectively. Results are shown in Fig. 4.5 for CH_4 and N_2 clathrates.

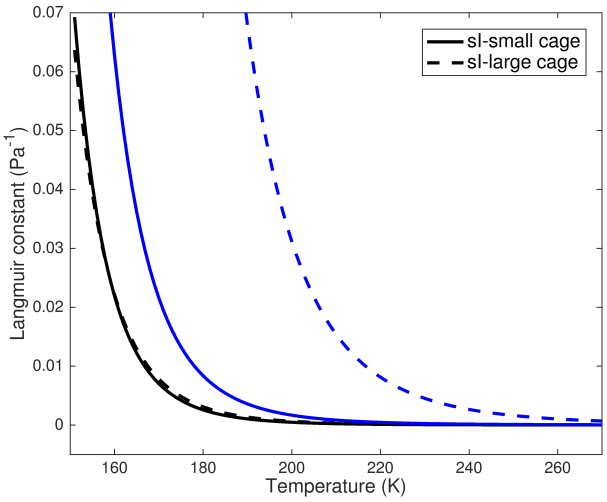

Figure 4.4: Langmuir constants calculated for sI methane clathrate with Equations 4.6 (black curves) and 4.21 (blue curves) as a function of temperature.

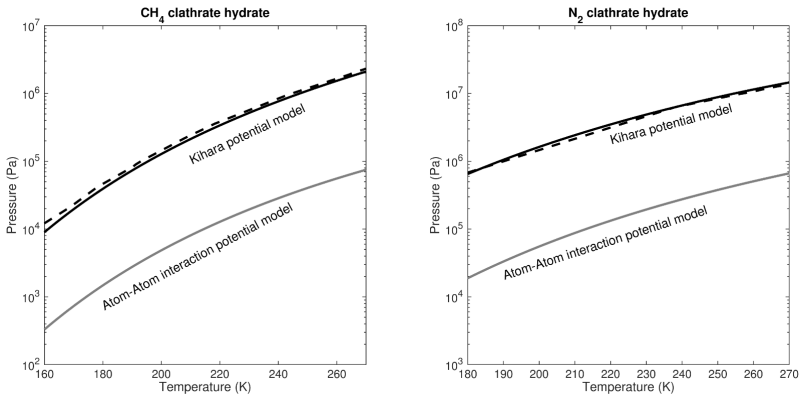

Figure 4.5: Dissociation pressure for CH_4 (left) and N_2 (right) clathrates calculated following the algorithm described in Fig. 4.2, in which the Langmuir constants determination step is done via Equations 4.6 and 4.21 for the Kihara potential model and the atom-atom approach, respectively. The dashed line represents experimental equilibrium data.

We observe that the Kihara potential model gives a dissociation pressure close to the experimental one, while the atom-atom interaction potential method strongly underestimates it by a factor varying from 28 to 35 for methane clathrate and from 20 to 52 for nitrogen clathrate. This last model is thus excluded for future modelling and following predicted

clathrate compositions are based on the Kihara potential model with parameters from Table 4.1.

4.3 Thermal model

4.3.1 Determination of surface temperature on slopes

This section describes the model used to determine surface temperature including implementation of slopes, which is similar to Schorghofer and Edgett (2006). Indeed, local slopes considerably alter surface and subsurface temperatures due to the difference in sunlight incidence and outgoing radiation and can therefore affect water ice and clathrate distribution in the soil. The atmospheric component of the model is pretty simple. However, we are mainly interested here in the impact of slopes on thermal conditions.

The heat balance on the surface includes incoming solar radiation Q, conduction into the soil, black body radiation by the surface and latent heat of CO_2:

$$Q(\alpha) + k\left(\frac{\partial T}{\partial z}\right)_{z=0} = \epsilon\sigma T^4 + L_{CO_2}\frac{\partial m_{CO_2}}{\partial t} \tag{4.22}$$

where α is the slope angle, ϵ the emissivity (assumed to be 1; Kieffer et al. (1977)), σ the Stefan-Boltzmann constant, L_{CO_2} the latent heat of carbon dioxide ($L_{CO_2} = 590$ kJ kg^{-1}) and m_{CO_2} the areal mass density of CO_2. The incoming flux Q is composed of four terms, which are represented in Fig. 4.6:

$$Q(\alpha) = Q_{\text{solar}}(\alpha) + Q_{\text{IR}}(\alpha) + Q_{\text{scat}}(\alpha) + Q_{\text{land}}(\alpha) \tag{4.23}$$

where Q_{solar} is the direct solar insolation, Q_{IR} is the thermal infrared emission from the atmosphere, Q_{scat} is the scattered light and Q_{land} is the thermal radiation received from other surfaces in the field of view of the sloped surface.
The primary effect of a slope is to modify the incidence angle of direct sunlight. The angle θ of the Sun above a sloped surface is given by:

$$\sin\theta = \cos\alpha\sin\beta - \sin\alpha\cos\beta\cos(\Delta a) \tag{4.24}$$

where Δa is the difference between the azimuth of the Sun and the azimuth of the topographic gradient and β the elevation of the Sun, expressed by:

$$\sin\beta = \cos\phi\cos\delta\cos h + \sin\phi\sin\delta \tag{4.25}$$

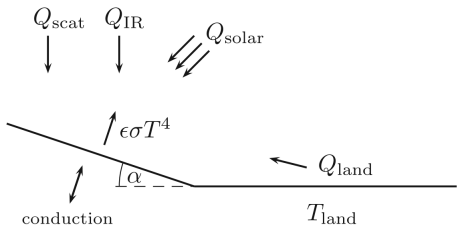

Figure 4.6: Contributions to the heat balance on a frost free surface with a slope angle α and a surface temperature T (Aharonson and Schorghofer, 2006).

where ϕ is the geographic latitude, δ the declination of the Sun and h the hour angle. When $\sin\beta < 0$ or $\sin\theta < 0$, the Sun is assumed to be below the horizon and Q_{solar} is therefore set to 0. Otherwise, its value is given by:

$$Q_{\text{solar}} = \frac{S_0}{R^2}(1-A)(1-f)^{1/\max(\sin\beta,0.04)}\sin\theta \tag{4.26}$$

where S_0 is the solar constant (at 1 AU), A is the albedo and the factor f is due to the extinction of the atmosphere ($f = f_{\text{IR}} + f_{\text{scat}}$). The term $1/\max(\sin\beta, 0.04)$ takes into account the path length through the atmosphere. The distance from the Sun R in AU is calculated following Allison and McEwen (2000):

$$\begin{aligned} R = 1.5236\,(1.00436 &- 0.09309\cos M - 0.00436\cos(2M) \\ &- 0.00031\cos(3M)) \end{aligned} \tag{4.27}$$

where M is the mean anomaly. The thermal infrared emission is evaluated as a fraction $f_{\text{IR}} = 0.04$ (Kieffer et al., 1977) of noontime insolation and is kept constant during the day:

$$Q_{\text{IR}} = f_{\text{IR}}\frac{S_0}{R^2}\cos^2\left(\frac{\alpha}{2}\right)\sin\beta_{\text{noon}} \tag{4.28}$$

In addition, when $\sin\beta > 0$, the scattered light term is approximated by:

$$Q_{\text{scat}} = \frac{1}{2}f_{\text{scat}}\frac{S_0}{R^2}\cos^2\left(\frac{\alpha}{2}\right) \tag{4.29}$$

where half of Q_{scat} is considered to be lost to space and $f_{\text{scat}} = 0.02$ (Schorghofer and Edgett, 2006). Finally, the last contribution to Q is given by:

$$Q_{\text{land}} = \sin^2\left(\frac{\alpha}{2}\right)\epsilon_{\text{land}}\sigma T_{\text{land}}^4 \tag{4.30}$$

A default value of 0.25 (Kieffer et al., 1977) is chosen for albedo when no CO_2 covers the surface. The Equation 4.22 is then solved for the surface temperature using the Newton-Raphson method and when the temperature falls below the sublimation temperature of CO_2 (147 K in the northern hemisphere, 143 K in the southern hemisphere; Aharonson and Schorghofer (2006)), carbon dioxide begins to accumulate on the surface and albedo is changed accordingly ($A = 0.65$). The surface temperature remains at a constant value (147 K or 143 K depending on the location) until all the CO_2 finally sublimates away. During this time, the surface heat balance is solved for m_{CO_2} to determine the mass of carbon dioxide that either sublimates or condenses at each time step. Fig. 4.7 shows examples of surface temperature obtained with slope implementation. As expected, the surface temperature on an equator-facing (resp. pole-facing) slope is higher (resp. lower) than on a flat floor. For the right panel, model inputs have been chosen similar to Aharonson and Schorghofer (2006). Their results for the variation of the mean surface temperature with the slope angle are comparable to ours showing the proper implementation of slopes in our model.

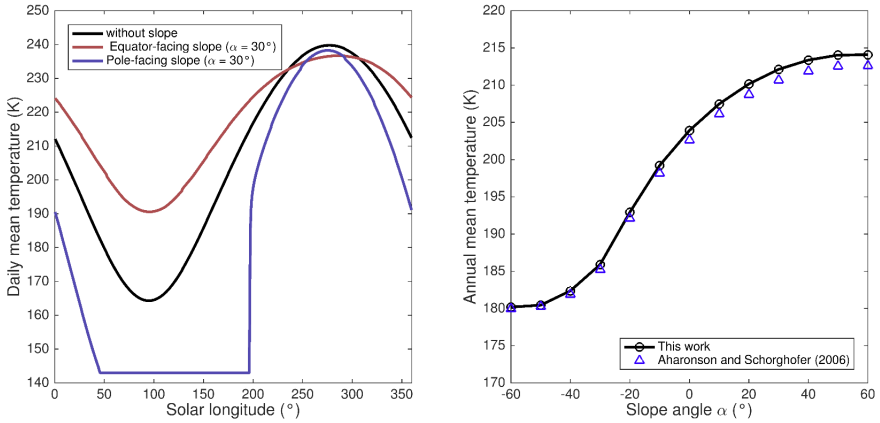

Figure 4.7: (Left) Daily average surface temperature at 40°S as a function of solar longitude. Calculations were made without slope (black curve), with an equator-facing slope of 30°(red curve) and with a pole-facing slope of 30°(blue curve). The albedo of the surface is $A = 0.25$ and the thermal inertia $I = 250$ J m^{-2} K^{-1} s$^{-1/2}$. (Right) Annual mean surface temperature as a function of slope at 35°N. Equator-facing slopes are shown as positive and pole-facing as negative. Albedo and thermal inertia have been taken similar to Aharonson and Schorghofer (2006) ($A = 0.3$ and $I = 150$ J m^{-2} K^{-1} s$^{-1/2}$).

4.3.2 Subsurface temperature

A one-dimensional diffusion equation for subsurface temperature with depth dependent thermal conductivity, density and specific heat is solved with a semi-implicit (unconditionally stable) Crank-Nicolson scheme on a grid with variable spacing:

$$\rho(z)c(z)\frac{\partial T(z,t)}{\partial t} = \frac{\partial}{\partial z}\left(k(z)\frac{\partial T(z,t)}{\partial z}\right) + \rho(z)H \tag{4.31}$$

where ρ is density, c is specific heat capacity, T is temperature, z is vertical coordinate, t is time, k is thermal conductivity and H is radiogenic heat production. The latter is set to a constant value (5×10^{-11} W kg^{-1}) assuming a vertically homogeneous distribution of radiogenic heat-producing elements in the planet's crust (Hahn et al., 2011). Each subsurface layer can have specific thermal properties of density, heat capacity and thermal conductivity assigned to them. Fig. 4.8 shows daily average temperature profiles calculated at regular intervals over a martian year for a homogeneous dry soil and a layered subsurface. For the latter, thermal properties are changed below 50 cm deep to correspond to those of ice-cemented soil. It can be seen that the amplitude of temperature oscillations is greater in dry soil than in ice-cemented soil. However, these oscillations reach a more important depth in the soil saturated with ice.

In our simulations to determine global maps of the top of the clathrate stability zone (TCSZ), the subsurface model is divided in two layers. The thermal properties of the upper layer are set to fit with the thermal inertia derived from Mars Global Surveyor Thermal Emission Spectrometer observations (Putzig and Mellon, 2007). Accordingly, the regolith bulk density ρ_b (kg m^{-3}) of this layer is determined as a function of thermal inertia I (J m^{-2} K^{-1} s$^{-1/2}$) following the empirical relation from Mellon and Jakosky (1993):

$$\rho_b = 150 + 100\sqrt{34.2 + 0.714I} \tag{4.32}$$

with a maximum value assumed to be 2500 kg m^{-3}. The specific heat capacity c is set to 800 J kg^{-1} K^{-1} and the thermal conductivity k is then determined using $k = I^2/(\rho_b c)$. The properties of the lower layer depend on the latitude of the studied area. Between 50°N and 50°S, the top of the lower layer is set to 1 m deep and its thermal properties are representative of dry basalt. Northward of 50°N and southward of 50°S, the lower layer starts at 50 cm deep and has thermal properties representative of ice-saturated soil. This choice is based on the subsurface water ice stability predicted by equilibrium models (Mellon et al., 2004;

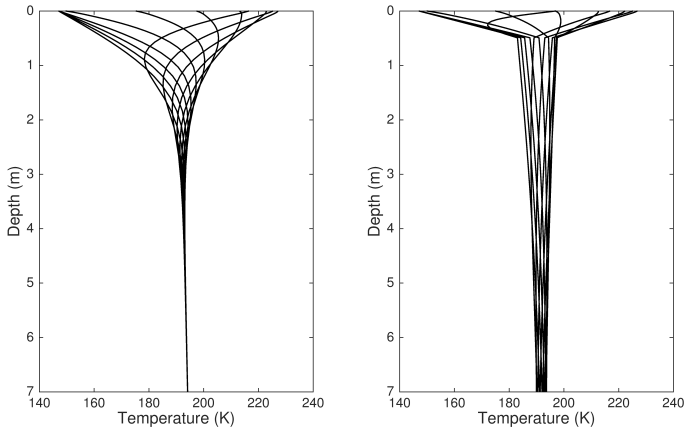

Figure 4.8: Example subsurface temperature profiles for a homogeneous dry soil (I = 250 J m^{-2} K^{-1} s$^{-1/2}$)(left) and a layered subsurface (right) at a latitude of 55°N. Each curve is a diurnal average temperature profile calculated at regular intervals for a full martian year. For the layered case, thermal properties are changed below 50 cm deep to correspond to those of ice-cemented soil (I = 2290 J m^{-2} K^{-1} s$^{-1/2}$). The heat flow is assumed equal to 19 mW m^{-2}.

Schorghofer and Aharonson, 2005). The compression of pore spaces with depth is modelled following Clifford (1993):

$$\Phi(z) = \Phi_0 \exp(-z/K_0) \tag{4.33}$$

where Φ_0 is the surface porosity (40%), z is the depth and K_0 is the porosity decay constant ($\sim$ 2.82 km). The variation of the volumetric heat capacity and thermal conductivity with depth is then given by:

$$\rho c(z) = (1 - \Phi(z))\rho_{\mathrm{dry}} c_{\mathrm{dry}} + \Phi(z)\rho_{\mathrm{ice}} c_{\mathrm{ice}} \tag{4.34}$$

$$k(z) = k_{\mathrm{dry}}^{(1-\Phi(z))} k_{\mathrm{ice}}^{(\Phi(z))} \tag{4.35}$$

where properties of water ice and basalt are referred to in Table 4.5. As mentioned above, we consider a basaltic mineralogy for the second layer of our subsurface model, wether in the presence of water ice or not. A basalt composition is quite representative of the martian crust. However, local variations in the soil material could strongly affect the methane clathrate distribution in the martian subsurface. Therefore, in the following chapter, a sensitivity study is firstly performed to evaluate the impact of the soil properties, among others, on the stability field of clathrates.

Table 4.5: Typical thermophysical properties of geological materials used in this study.

	k (W m^{-1} K^{-1})	ρ (kg m^{-3})	c (J kg^{-1} K^{-1})	I (J m^{-2} K^{-1} s$^{-1/2}$)
Water ice	2.8	920	1960	2247
Basalt	2	3000	800	2190
Ice-saturated soil	2.5	2018	1040	2290
Dry unconsolidated soil	0.045	1650	800	244

The changes in surface temperature and pressure in latitude and longitude over the martian year are given by the Mars Climate Database v5.2 ("Climatology" scenario, average solar EUV conditions) (Forget et al., 1999; Millour et al., 2015). The present-day heat flow variations across the martian surface are taken from the model of Parro et al. (2017) that provides a surface heat flow varying between 14 and 25 mW m^{-2} with an average value of 19 mW m^{-2}.

Finally, the pressure in pore spaces that controls stability of methane clathrate hydrates in subsurface has two limiting cases: lithostatic and atmospheric pressure. Assuming isolated porosity, the local confining pressure is equal to the lithostatic pressure:

$$P(z) = P_s + \rho g z \tag{4.36}$$

where P is lithostatic pressure at depth z, P_s is surface pressure, ρ is density of overburden and g is average gravity on Mars surface (3.72 m s^{-2}). Alternatively, if the pore spaces are open, the gas phase pressure in subsurface is much smaller than previously and is given by the barometric equation:

$$P(z) = P_s \exp\left(\frac{gM}{RT_s} z\right) \tag{4.37}$$

where P is gas phase pressure at depth z, M is molecular weight of the atmosphere (44 g/mol), R is ideal gas constant and T_s is surface temperature. However, the real pore pressure profile is generally more complex with an intermediate value between the lithostatic and the depth-ajusted barometric pressure depending on how pores are connected and their saturation state (Max and Clifford, 2000).

Scenarios for Early Mars

These scenarios are used in the next chapter when investigating the evolution of the martian cryosphere with time. The mean surface temperature of Early Mars remains uncertain and two different scenarios are

therefore adopted. In the first one, the mean surface temperature at the equator 4 Gyr ago is set to 273.15 K, which assumes a warmer early Mars with some periods of the year where temperatures regularly exceed the freezing point of water. In this scenario represented in Fig. 4.9a (Haberle, 1998), the mean surface temperature decreases rapidly during the first billion years to a value about 235 K. Then, it declines smoothly until present time to reach 220 K, the current mean equatorial temperature. In the second scenario, the mean surface temperature is set to a constant value equal to 220 K. The evolution of the surface heat flow is determined by curve fitting to the model of Grott and Breuer (2010) and is represented in Fig. 4.9b. Grott and Breuer (2010) obtained similar results to Hauck and Phillips (2002) with values of the surface heat flow around 60 mW m^{-2} at 3.5 Gyr and about 20 mW m^{-2} today. The latter number is consistent with the present average value of 19 mW m^{-2} found by Parro et al. (2017). Surface abundances of K and Th have been measured by the Gamma Ray Spectrometer on board the 2001 Mars Odyssey spacecraft (Taylor et al., 2006) while U abundances have been determined assuming a Th/U ratio of 3.8 (Hahn et al., 2011). Using the surface average heat-producing elements abundances (0.18, 0.69 and 3652 ppm for U, Th, and K respectively (Ruiz et al., 2011)), the crustal heat production is determined and its evolution through time is shown in Fig. 4.9c. Its average value varies between 20×10^{-11} W kg^{-1} at 4 Gyr and 5×10^{-11} W kg^{-1} at present day (Hahn et al., 2011).

4.4 Transport of gases in porous media

The second part of this chapter describes the diffusive-adsorptive model used to study methane and water vapor transport from shallow sources through the porous subsurface of Mars. Advection is also briefly discussed although we did not investigate this process.

4.4.1 Mass transfer versus mass transport

During CH_4 and H_2O gases transport through the martian soil, some of the moving gases will adsorb onto rock surfaces and H_2O vapor will also condense into ice. Mass transfer refers to transfer of mass or partitioning of soil gases between the solid and gas phases and therefore slows up their migration through the subsurface. For water vapor transport, it is described as:

$$\sigma = \phi \left(1 - f_i\right) \rho_G + \phi \rho_i + \rho_a \tag{4.38}$$

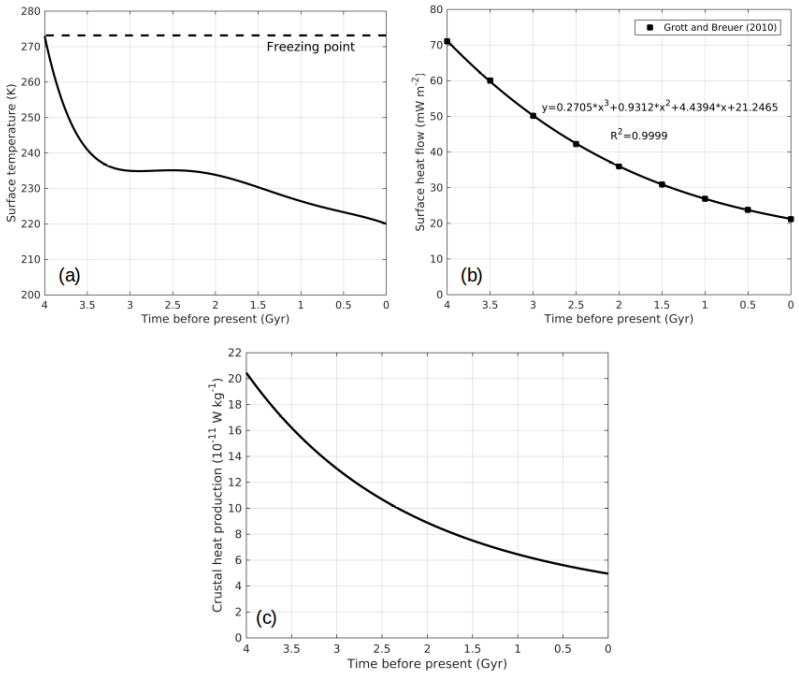

Figure 4.9: Scenarios for the evolution of (a) martian surface temperature at the equator (warm scenario) (Haberle, 1998), (b) martian surface heat flow (Grott and Breuer, 2010) and (c) crustal heat production used in the present study.

where σ is the total water content (kg m^{-3}), ϕ is the regolith porosity, f_i is the volumetric fraction to which pore spaces are filled with ice, ρ_G is the vapor density in the void space (not occupied by regolith or water ice), ρ_i is the ice density in pore space and ρ_a is the density of adsorbed water. For methane transport, Equation 4.38 is reduced to:

$$\sigma = \phi\rho_G + \rho_a \tag{4.39}$$

4.4.2 Mechanisms of gas transport

The important parameters determining which gas transport regime is dominant include the mean free path (the average distance a gas molecule travels before colliding with another), the pore size and the particle size. Following this, gas transport through porous media can be divided in different mechanisms (Mason and Malinauskas, 1983):

- Free molecule or Knudsen flow occurs when the pore radius is less

than one tenth of the gas mean free path, and molecule-wall collisions dominate.

- Viscous or advective flow, in which the gas acts as a continuum fluid under the influence of a pressure gradient. Advection is dominant when the gas mean free path is much smaller than the pore radius and the particule radius resulting in molecule-molecule collisions being dominant.

- Ordinary or molecular diffusion refers to the relative motion of the different gas species under the influence of concentration gradients, temperature gradients (thermal diffusion), pressure gradients (pressure diffusion) or external forces such as electric or magnetic field (forced diffusion). In this regime, the pore radius is larger than 10 times the gas mean free path and collisions between gas molecules dominate.

- Surface flow or diffusion in which molecules move along a solid surface in an adsorbed layer.

Surface diffusion is generally not significant (Scanlon et al., 2002) and is thus not taken into account in this work. Pressure diffusion and thermal diffusion are also neglected as their contribution is rather small compared to molecular diffusion (concentration gradients) and Knudsen diffusion, which are normally considered to be the most important diffusive processes in soils (Thorstenson and Pollock, 1989a,b). Moreover, the diffusive model is applied with near-surface sources and pressure diffusion is usually negligible at depths of less than 100 m (Amali and Rolston, 1993).

The total molar flux N^T of a gas mixture in a porous medium is given by the sum of the flux resulting from diffusion N^D and the advective flux N^V. For the ith species, it is written as:

$$N_i^T = N_i^D + N_i^V \tag{4.40}$$

4.4.3 Advective flux

If a total pressure gradient exists in the subsurface, gases will be transported from regions of higher pressure to those of lower pressure. Advective flow does not lead to the separation of the different species in the gas mixture, which are thus all transported at the same rate. The molar viscous flux of gas component i satisfies the relationship:

$$N_i^V = y_i N^V \tag{4.41}$$

where y_i is the mole fraction of component i and N^V is represented by Darcy's law:

$$N^V = -c_T \frac{k_G}{\mu_G} (\frac{\partial P}{\partial z} - \rho_G g) \tag{4.42}$$

where c_T is the total molar concentration, k_G is the gas permeability of the porous medium, μ_G is the gas-phase viscosity, ρ_G is the gas density, g is the gravitational acceleration and z is the vertical coordinate increasing downward. The first term in parentheses is the driving force due to pressure and the second term is the driving force due to gravity. From Equation 4.42, it can be seen that the main driving force for advective flow is the pressure gradient, while the resistance to flow is caused by the gas viscosity.

When the pore size reduces as a result of decreasing grain size, the flow regime changes from advective flux to viscous slip flux (Klinkenberg effect) and then to Knudsen diffusive flux. Klinkenberg effect occurs in the transition flow regime when the mean free path of the gas molecules becomes approximately the same as the pore radius and results in a nonzero gas velocity at the pore wall and in underestimation of gas flux by Darcy's law. Indeed, according to Equation 4.42, the molar flux should decrease as the average pressure is reduced. However, the flux reaches a minimum value at low pressures and then increases with decreasing pressure due to slip flow (Ho and Webb, 2006). The permeability k_G actually depends on the pressure and has been evaluated by Klinkenberg et al. (1941) that derived the following expression:

$$k_G = k_l \left(1 + \frac{b_i}{\bar{P}}\right) \tag{4.43}$$

where k_l is the permeability at infinite pressure when the gas behaves as a liquid, b_i is a constant function of the porous medium and the gas i and $\bar{P}$ is the mean pressure. At large mean pressure, liquid and gas permeabilities are similar. As the average pressure decreases, the two permeabilities differ from each other and gas slippage is enhanced.

4.4.4 Molecular diffusive flux

Molecular diffusion occurs when a concentration or mole fraction gradient exists and implies the counterdiffusion of equimolar pairs of gases in pores whose size is much larger than that of the mean free path of the gas species. This mechanism therefore takes place even under isothermal and isobaric conditions and is considered to be "segregative" because it

results in separation of the different component gases. Fick's first law is commonly used to describe the molar diffusive flux of gas i in gas j:

$$N_i^F = -D_{ij} c_T \frac{\partial y_i}{\partial z} \tag{4.44}$$

where $D_{ij} = D_{ji}$ (Bird et al., 2007) is the molecular diffusion coefficient that depends on temperature, pressure and the properties of the two gases. Note that Fick's law excludes the effects of Knudsen diffusion and nonequimolar diffusion and its adaptation for use in porous media will be discussed later.

4.4.5 Bulk diffusive flux

In general, equimolar counterdiffusion is rare in porous media. Bulk diffusion includes molecular and nonequimolar diffusion, for which gas components have different molecular weights. Lighter molecules diffuse faster than heavier gas molecules, which gives rise to a pressure gradient that will move the gas phase in the direction opposite to the flow of lighter molecules. The resulting flux (nonsegregative) is diffusive and is called nonequimolar flux or diffusive slip flux (Cunningham and Williams, 1980). The molar bulk diffusive flux of gas component i can be written as:

$$N_i^D = N_i^F + y_i \sum_{j=1}^{n} N_j^D \tag{4.45}$$

where n is the number of gas components and $y_i \sum_{j=1}^{n} N_j^D$ is the nonequimolar flux.

4.4.6 Knudsen diffusive flux

As explained earlier, the Knudsen diffusion becomes important when the gas mean free path is much larger than the pore radius. In the Knudsen region, the molar flux of component i is given by:

$$N_i^D = -D_{iK} c_T \frac{\partial y_i}{\partial z} \tag{4.46}$$

The Knudsen diffusion coefficient D_{iK} depends on pore geometry and is defined as:

$$D_{iK} = \frac{2}{3} r \sqrt{\frac{8 k_B T}{\pi m_i}} \tag{4.47}$$

where r is the pore radius and m_i the molecular mass of the gas component i. It is important to note that the presence of water ice in pore spaces will affect the diffusion by reducing the pore size. In a regolith with an initial large pore diameter, a transition will take place in the flow regime from molecular-dominated to Knudsen-dominated diffusion as the open pores become smaller.

4.4.7 Effective diffusion coefficient

In the transition region, when the gas mean free path is about the same order of magnitude as the pore size, both molecular and Knudsen diffusion have to be taken into account. In this flow regime, an effective diffusion coefficient D_{eff} is commonly defined according to the Bosanquet interpolation formula:

$$\frac{1}{D_{\text{eff}}} = \frac{1}{D_{12}} + \frac{1}{D_{1K}} \tag{4.48}$$

Fig. 4.10 represents the evolution of the effective diffusion coefficient for water vapour as a function of pore radius. The Knudsen diffusion coefficient has been calculated with Equation 4.47, while the molecular diffusion coefficient has been determined following the expression given by Wallace and Sagan (1979) for H_2O diffusing through an atmosphere of CO_2 in martian conditions:

$$D_{H_2O-CO_2} = (0.1654\text{cm}^2\ \text{s}^{-1}) \left(\frac{T}{273.15\text{K}}\right)^{3/2} \left(\frac{1013\text{mbar}}{P}\right) \tag{4.49}$$

At martian pressures, the mean free path of CH_4 and H_2O molecules is ~ 10 μm (Meslin et al., 2011) and 7-9 μm (Hudson, 2008), respectively. These values are probably of the same order of magnitude as the mean pore size, which we assumed equal to 10 μm in the rest of this work.

Finally, the change in diffusion coefficient from free-gas to porous-media conditions is described by the ratio between the porosity Φ and the tortuosity τ, often called the obstruction factor:

$$D_{\text{porous media}} = \frac{\Phi}{\tau} D_{\text{eff}} \tag{4.50}$$

where the porosity ($\Phi < 1$) takes into account the limited pore cross section, while the tortuosity ($\tau > 1$) accounts for increased path length and dead ends in the porous subsurface.

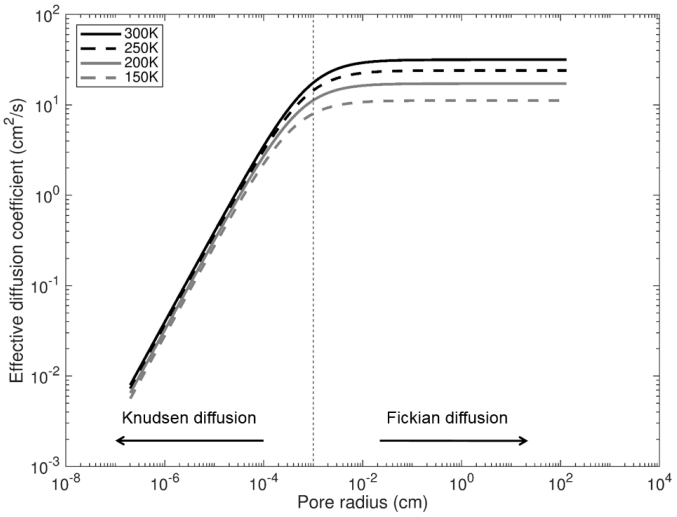

Figure 4.10: The effective diffusion coefficient for water vapour as a function of pore radius. Transport ranges from Knudsen to normal diffusion.

4.4.8 Adsorption

The main parameters that control adsorption are the partial pressure of gas, temperature and nature of the soil material. Adsorption of water in the martian subsurface retards the ice formation since it separates water in a supplementary phase. The Langmuir isotherm that is usually used to describe adsorption of gases onto surfaces is given by:

$$\theta_{\mathrm{eq}} = \frac{k_{\mathrm{eq}} P}{1 + k_{\mathrm{eq}} P} \tag{4.51}$$

where θ_{eq} is the fractional coverage of the monolayer at equilibrium, P is the partial pressure of gas and k_{eq} is the equilibrium rate constant, which describes the ratio between the adsorption rate constant and the desorption rate constant. Equation 4.51 is analogous to Equation 4.4 that determines the occupancy fraction in clathrate hydrates as a function of the Langmuir constant. The mass of adsorbed gas m_a (in kg kg^{-1}) is then expressed as:

$$m_a = \theta A_s m_{\mathrm{ML}} \tag{4.52}$$

where A_s is the specific surface area of the regolith and m_{ML} is the mass per unit surface area of a single adsorbed monolayer of gas. By multiplying m_a by the bulk density of the regolith, we can obtain the value for ρ_a in Equation 4.38.

In Equation 4.51, adsorption is supposed to be instantaneous but a time lag exists to reach equilibrium, as represented in Fig. 4.11 for water vapor, due to the intrinsic kinetics of the adsorption process. The variation of the surface coverage θ as a function of time is given by (Zent et al., 2001):

$$\frac{d\theta}{dt} = k_a(1-\theta) - k_d\theta \tag{4.53}$$

where k_a and k_d are the adsorption and desorption rate constants respectively. Solving this equation with the initial condition $\theta_{t=0} = 0$ gives:

$$\theta = \frac{k_a}{k_a + k_d}(1 - e^{-(k_a+k_d)t}) \tag{4.54}$$

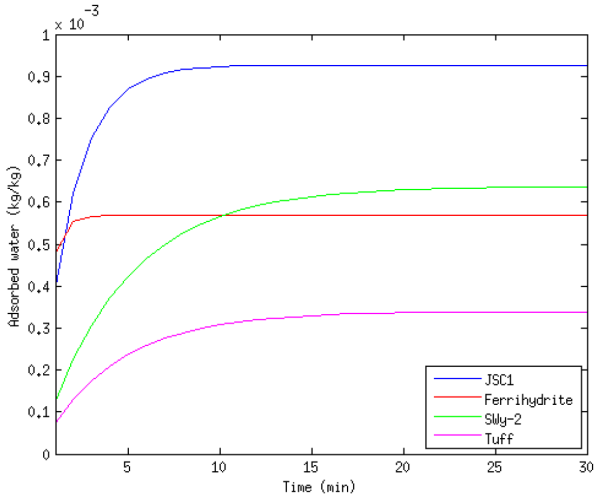

Figure 4.11: The amount of adsorbed water as a function of time for different samples at 243 K and 0.1 Pa. Kinetic constants and specific surface areas are taken from Beck et al. (2010) and Pommerol et al. (2009) respectively.

4.4.9 Gas transport models

Stefan-Maxwell equations

The Stefan-Maxwell equations are an extension of Fick's law for multicomponent gas mixtures and are given by:

$$\sum_{j=1,j\neq i}^{n} \frac{y_j N_i^D - y_i N_j^D}{D_{ij}} = -c_T \frac{dy_i}{dz} \tag{4.55}$$

These equations are available for diffusion in the bulk region only as they exclude Knudsen diffusion. The description of combined (diffusion and advection) transport of multicomponent gas mixtures is given by two models: the Dusty Gas Model (Mason and Malinauskas, 1983) and the Mean Transport Pore Model (see e.g. Arnošt and Schneider (1995)).

Dusty Gas Model (DGM)

The Dusty Gas Model (Mason and Malinauskas, 1983) is based on the full Chapman Enskog kinetic theory of gases. In this model, the porous medium is considered as one component of the mixture and is treated as a collection of giant spherical molecules (dust particles) kept in space by an external force. The total flux of a gas mixture is represented as the sum of the diffusive flux (molecular and Knudsen diffusion) and the viscous flux. The DGM in terms of total molar flux can be written as (Thorstenson and Pollock, 1989a):

$$\sum_{j=1,j\neq i}^{n} \frac{y_j N_i^T - y_i N_j^T}{D_{ij}} + \frac{N_i^T}{D_{iK}} = -c_T \frac{dy_i}{dz} - \left(1 + \frac{k_G P}{D_{iK}\mu_G}\right) y_i \frac{dc_T}{dz} \quad (4.56)$$

The first term on the left-hand side of Equation 4.56 considers molecular diffusion, while the second term accounts for Knudsen diffusion. The first and second terms on the right-hand side take into account the driving forces for diffusion (concentration gradient) and advection (total pressure gradient). If the Kudsen diffusion is negligible and there is no total pressure gradient, the DGM is reduced to Stefan-Maxwell equations.

Mean Transport Pore Model (MTPM)

As the DGM, the Mean Transport Pore Model is based on the Stefan-Maxwell equation modified to include Knudsen diffusion and the Darcy's law. The MTPM visualizes pores as cylindrical capillaries with radii distributed around a mean value r. Both models, DGM and MTPM, represent the mass transport due to concentration gradients (pure diffusion) with the same set of differential equations, that is to say:

$$\sum_{j=1,j\neq i}^{n} \frac{y_j N_i^D - y_i N_j^D}{D_{ij}} + \frac{N_i^D}{D_{iK}} = -c_T \frac{dy_i}{dz} \quad (4.57)$$

The adopted model

The diffusive model used in this work is based on Equation 4.57 that we apply to a binary gas mixture:

$$\frac{y_2 N_1^D - y_1 N_2^D}{D_{12}} + \frac{N_1^D}{D_{1K}} = -c_T \frac{dy_1}{dz} \tag{4.58}$$

where the subscript 1 is for CH_4 or H_2O and the subscript 2 refers to CO_2. Using $y_2 = 1 - y_1$ and Graham's law of diffusion ($-\frac{N_1^D}{N_2^D} = \left(\frac{m_2}{m_1}\right)^{1/2}$; Graham (1833)), Equation 4.58 can be rewritten as:

$$N_1^D = -D c_T \frac{dy_1}{dz} \tag{4.59}$$

where

$$\frac{1}{D} = \frac{1}{D_{1K}} + \frac{1 - y_1(1 - \sqrt{\frac{m_1}{m_2}})}{D_{12}} \tag{4.60}$$

Rewritting Equation 4.59 in terms of mass flux J gives:

$$J_1^D = -D \frac{d\rho_1}{dz} \tag{4.61}$$

Finally, the mass conservation equation is given by:

$$\frac{\partial \sigma}{\partial t} = \frac{\partial}{\partial z}\left(\frac{\Phi}{\tau} D \frac{\partial \rho_1}{\partial z}\right) \tag{4.62}$$

where σ is determined as described in section 4.4.1 and the obstruction factor has been added to take into account the change in the diffusion coefficient due to the porous medium.

Application to water vapor transport

The determination of the molecular diffusion coefficient $D_{H_2O-CO_2}$ is made using Equation 4.49, while the Knudsen diffusion coefficient D_{H_2OK} is calculated with Equation 4.47. The variation of the pore radius r with water ice content is computed with the following expression (Mellon and Jakosky, 1993):

$$r = r_0 \sqrt{1 - \frac{\rho_i}{\rho_{ice}}} \tag{4.63}$$

where r_0 is the mean pore radius ($\sim 10\mu$m) and $\rho_{ice} = 926$ kg m^{-3}.

Adsorption in thermodynamic equilibrium is determined using adsorption isotherms for palagonite (Zent and Quinn, 1997):

$$\rho_a = \rho_b A_s m_{\mathrm{ML}} \left(\frac{K_0 P}{e^{-\epsilon/T} + K_0 P} \right)^{\nu} \tag{4.64}$$

where ρ_b is the bulk density of the regolith, the specific surface area A_s for palagonite is 17,000 $\mathrm{m}^2\ \mathrm{kg}^{-1}$, the mass per unit surface area of a single adsorbed monolayer of water $m_{\mathrm{ML}} = 3 \times 10^{-7}\ \mathrm{kg\ m}^{-2}$, $K_0 = 7.54 \times 10^{-9}\ \mathrm{Pa}^{-1}$, $\epsilon = 2697.2$ K and $\nu = 0.4734$. These adsorption isotherms are represented in Fig. 4.12.

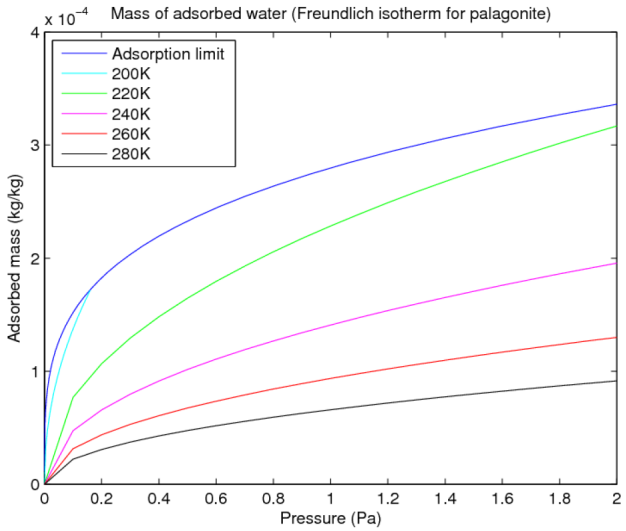

Figure 4.12: Mass of adsorbed water as a function of H_2O partial pressure.

Combining Equations 4.38, 4.62 and the ideal gas law, leads to:

$$\begin{aligned} &\Phi \frac{\partial}{\partial t} \left(\left(1 - \frac{\rho_i}{\rho_{ice}} \right) \frac{P}{T} + \frac{R}{M} \rho_i \right) + \frac{R}{M} \left(\frac{\partial \rho_a}{\partial P} \frac{\partial P}{\partial t} + \frac{\partial \rho_a}{\partial T} \frac{\partial T}{\partial t} \right) \\ &= \frac{\partial}{\partial z} \left(\frac{\Phi}{\tau} \left(1 - \frac{\rho_i}{\rho_{ice}} \right)^2 D \frac{\partial}{\partial z} \frac{P}{T} \right) \end{aligned} \tag{4.65}$$

where M is the molar mass of H_2O and the term $(1 - \frac{\rho_i}{\rho_{ice}})^2$ takes into account the changes in porosity and tortuosity with ice content (Hudson, 2008). If no ice is present in the subsurface, ρ_i is set to zero and Equation 4.65 determines the partial pressure of water. If ice is present, then the equation is solved for ρ_i using the saturation vapor pressure P_{sat} value for P:

$$P_{\text{sat}} = 611.0 \exp\left(22.5\left(1 - \frac{273.16}{T}\right)\right) \tag{4.66}$$

The upper boundary condition at the martian surface is given by the partial pressure of water and $\rho_i = 0$, while for the lower boundary condition, we assume zero vapor flux (Schorghofer and Aharonson, 2005). Therefore, H_2O is not allowed to diffuse further down in the soil than our spatial range allows.

Application to methane transport

Combining Equations 4.39 and 4.62, we obtain:

$$\frac{\partial \Phi \rho_G}{\partial t} + \frac{\partial \rho_a}{\partial t} = \frac{\partial}{\partial z}\left(\frac{\Phi}{\tau} D \frac{\partial \rho_G}{\partial z}\right) \tag{4.67}$$

As for water vapor, the Knudsen diffusion coefficient D_{CH_4K} is determined with Equation 4.47 and the molecular diffusion coefficient is calculated similarly to Meslin et al. (2011):

$$D_{CH_4-CO_2} = \frac{3}{8}\sqrt{\frac{\pi}{2\mu_{12}}}\frac{(k_B T)^{3/2}}{P}\frac{1}{\pi \sigma_{12}^2 \Omega(T)} \tag{4.68}$$

where μ_{12} is the reduced mass of the CH_4-CO_2 mixture, σ_{12} is the collision diameter (3.745×10^{-10} m; Boushehri et al. (1987)) and Ω is the diffusion collision integral given by:

$$\begin{aligned}\Omega(T^*) = &\exp(0.295402 - 0510069(\ln T^*) + 0.189395(\ln T^*)^2 \\ &- 0.045427(\ln T^*)^3 + 0.0037928(\ln T^*)^4)\end{aligned} \tag{4.69}$$

where $T^* = \frac{T}{198.5K}$ (Boushehri et al., 1987).

At equilibrium, ρ_G and ρ_a are linked by the equilibrium rate constant k_{eq} as (Meslin et al., 2011):

$$\left(\frac{\rho_a}{\rho_G}\right)_{eq} = k_{eq}(T) = \frac{\rho_b A_s \bar{v}}{4}\frac{h}{k_B T}\exp\left(\frac{\mid \Delta H \mid}{RT}\right) \tag{4.70}$$

where $\bar{v}$ is the mean thermal speed of CH_4 molecules at temperature T, h is the Planck constant and ΔH = -18.08 kJ mol^{-1} (Gough et al., 2010). Equation 4.67 can therefore be rewritten as:

$$\frac{\partial(\Phi + k_{eq})\rho_G}{\partial t} = \frac{\partial}{\partial z}\left(\frac{\Phi}{\tau} D \frac{\partial \rho_G}{\partial z}\right) \tag{4.71}$$

The lower boundary condition is defined as a given mass of CH_4 injected at time $t = 0$ or a constant mass flux. At the surface, we assume a zero constant value for methane concentration, which implies that atmosphere is well mixed and removes away methane faster than the diffusion timescale (Stevens et al., 2015).

4.5 Summary

A diagram of the different models introduced in this chapter and their relationships is presented in Fig. 4.13. The clathrate stability model gives the dissociation pressure P_{diss} at a given temperature T of multiple guest clathrates by specifying the various gas species G and their molar fraction x in the initial gas phase. It is coupled to our subsurface thermal model to obtain the clathrate stability zone in the martian crust. The description of the subsurface is made in two different ways. In the first one, all the parameters are kept constant except one in order to investigate the sensitivity of the methane clathrate stability field to the soil properties: pressure in pore spaces P, thermal conductivity k, density ρ, specific heat capacity c, heat flow q. The upper boundary conditions are given by the mean surface temperature and pressure at the considered latitude for a flat or sloped surface. In the second description used for the determination of our global maps, the subsurface is divided in two layers. The thermal properties of the upper layer are set to fit with the thermal inertia derived from MGS TES observations (Putzig and Mellon, 2007), while the lower layer has a basaltic mineralogy with the presence of water ice in pore spaces depending on the latitude. The changes in surface temperature and pressure in latitude and longitude over the martian year are taken from the Mars Climate Database (Forget et al., 1999) and the heat flow variations across the martian surface from Parro et al. (2017).

The relative abundances of guest species trapped in clathrates are simulated based on the Kihara potential model with parameters, listed in Table 4.1, that have been optimized by Herri and Chassefière (2012) at martian temperature conditions. The calculated depths and compositions of methane clathrates can then constrain our CH_4 sources in our gas transport model. The latter takes into account molecular and Knudsen diffusion as well as adsorption and is applied to study the diffusion of water vapor and methane. Its parameters include porosity Φ, tortuosity τ, diffusion coefficients D_{eff}, specific surface area SSA and methane enthalpy ΔH.

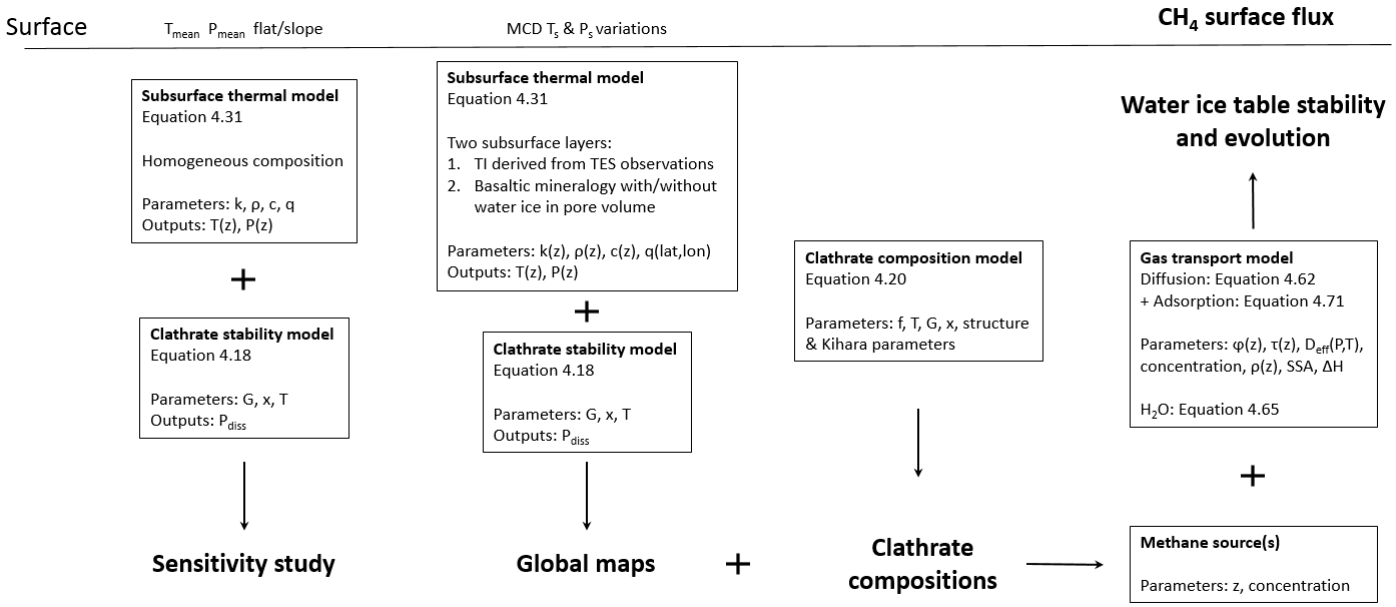

Figure 4.13: Summary of developed models, their inputs / outputs and the connections between them.

Chapter 5

Methane clathrate stability and composition on Mars

Contents

5.1 Methane clathrate stability zone: a sensitivity study 86
5.1.1 Subsurface pressure 86
5.1.2 Subsurface composition 87
5.1.3 Heat flow 89
5.1.4 Presence of magnesium perchlorate 89
5.1.5 Initial gas phase 92
5.1.6 Sloping surface 92
5.2 Methane clathrate stability zone: Global maps 96
5.3 Variability of methane trapping 100
5.4 Variation of clathrate stability zone in the past 103
5.5 Summary 107

This chapter is dedicated to the study of stability depth and composition of CH_4 clathrates on Mars and most of the results presented here have been described in Gloesener et al. (submitted). In the first part, a sensitivity study is performed to determine variations of methane clathrate stability zone as a function of pressure in pore spaces, thermal properties of the subsurface, heat flow, presence of salts in the system and fraction of CH_4 in the initial gas phase used to form clathrates. In addition, the change in stability depth of methane clathrate is investigated by varying the orientation and angle of the slope at the surface. In the second part of the chapter, global maps of the top of clathrate stability zone

are obtained following the approach described in section 4.3.2. Then, we examine the effect of gas phase composition and formation pressure on guest abundance by considering the CO_2-CH_4-N_2 and CO_2-CH_4-H_2 mixtures. The latter is considered since most of the methane generation mechanisms imply H_2 production (see section 2.3). Finally, methane clathrate formation in the past is discussed at the end of this chapter.

5.1 Methane clathrate stability zone: a sensitivity study

5.1.1 Subsurface pressure

The temperature and pressure conditions prevailing on Mars do not allow CH_4 clathrates to be stable at the surface. However assuming that pores are closed, they are stable in the subsurface as shown in Fig. 5.1. In ice-cemented soil, the top of methane clathrate stability zone (CSZ) is about 0.4 m deep in the south polar region when surface temperature reaches 150 K during winter. For a higher surface temperature of 180 K, CH_4 clathrate hydrates need to be buried deeper than $\sim$ 5.25 m to remain stable. In the same temperature conditions, the addition of carbon dioxide in methane clathrate reduces the dissociation pressure (Chastain and Chevrier, 2007). Hence CO_2-rich clathrates form at shallower depth than methane clathrate hydrates and are even stable at the surface in polar regions. If the pressure profile is calculated assuming an open porosity in the subsurface, the pressure is then too low and CH_4-rich clathrate stability conditions are never met at any depth and latitude.

Clathrate hydrate destabilization can occur either by an increase of the subsurface temperature or a decrease of the local pressure. In order to explain reported observations of martian methane, consideration should be given to subsurface processes, such as seismic activity or impacts (Mousis et al., 2013a), which could dissociate clathrates locally and sporadically. Indeed, these processes could release overburden pressure, increase local soil temperatures or open cracks and fractures that would therefore connect the clathrate reservoir to the surface leading to its destabilization and the methane release in the atmosphere. On the other hand, landslides can also occur following clathrate dissociation (Komatsu et al., 2011). Moreover, clathrate hydrate destabilization could be initiated by shallow ground ice evaporation during warmer time periods, for instance.

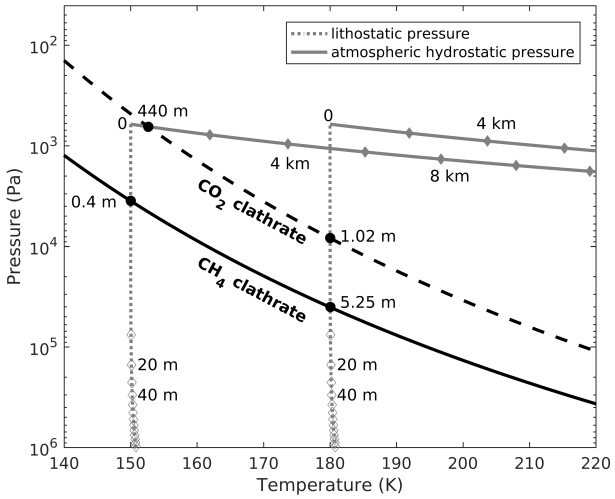

Figure 5.1: Dissociation pressure of CH_4 clathrate (black curve) and CO_2 clathrate (dashed black curve), lithostatic pressure (dotted grey line) and atmospheric hydrostatic pressure in a porous subsurface (grey line) as a function of temperature. The pressure profiles have been calculated using thermal properties corresponding to an ice-cemented soil ($k = 2.5$ W m^{-1} K^{-1}, $\rho = 2018$ kg m^{-3}), the heat flow and the heat production have been assumed equal to 15 mW m^{-2} and $5{\times}10^{-11}$ W kg^{-1} respectively and the two considered surface temperatures are 150K and 180K.

5.1.2 Subsurface composition

Regarding the subsurface composition, the type of soil directly controls the geothermal conditions and therefore the depth of clathrate formation. In Fig. 5.2, the methane clathrate stability zone is determined using different thermal properties in the subsurface model corresponding to thermal inertia ranging from 250 to 2000 J m^{-2} K^{-1} s$^{-1/2}$. The volumetric heat capacity ρc is kept constant (1.6×10^6 J K^{-1} m^{-3}) while the thermal conductivity k is changed for each panel (A, B, C and D). The different tested soil compositions are representative for martian materials ranging from ice-cemented soil (A) to dry unconsolidated soil (D). The stability depths are calculated based on the present-day mean annual surface temperatures (Clifford and Parker, 2001), while the surface heat flow and the surface pressure are constant and assumed equal to their average value, 19 mW m^{-2} (Parro et al., 2017) and 610 Pa respectively.

Similarly to previous studies (Chastain and Chevrier, 2007; Root and Elwood Madden, 2012), methane clathrate hydrates are expected to

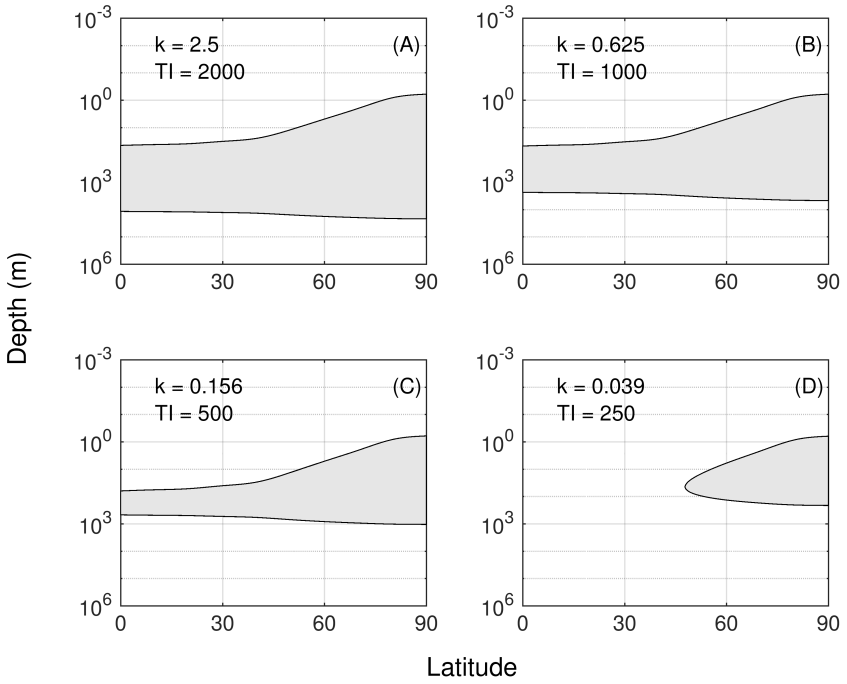

Figure 5.2: Stability zone of simple CH_4 clathrates in the martian subsurface for different thermal properties in the subsurface model corresponding to thermal inertia (TI) ranging from 250 to 2000 J m^{-2} K^{-1} s$^{-1/2}$. The volumetric heat capacity ρc is kept constant (1.6×10^6 J K^{-1} m^{-3}) while the thermal conductivity k is changed to 2.5 (A), 0.625 (B), 0.156 (C) and 0.039 W m^{-1} K^{-1} (D) respectively.

form at shallower depth with increasing latitude and their stability zone is thicker at high latitude. The thermal conductivity of the soil is a key parameter in the determination of the clathrate stability zone. Materials with high thermal conductivity such as sandstone or ice-cemented soil evacuate heat more efficiently and thus maintain lower temperatures, which allows clathrate formation with a stability zone of several kilometers thick. In Fig. 5.2a, CH_4 clathrate stability zone extends from about 45 m deep to 11.8 km deep at the equator and from 0.6 m deep to about 22 km deep at the pole. On the contrary, if thermal conductivity is not high enough to maintain the low temperature required for clathrate formation, clathrate stability conditions are never met in equatorial regions or only on a small subterranean layer a few hundred meters thick as shown in Fig. 5.2.

The stability field of clathrates is calculated using mean annual surface temperatures. However, oscillations of temperature due to seasonal variations can propagate over several meters deep and so reach the clathrate stability zone at locations where it is close to the surface. Consequently, at high latitude, the shallow stability zone will be shifted downwards during warm seasons when the soil temperatures are too high to maintain stable clathrates and inversely during the colder time periods. The depth at which temperature fluctuation is reduced by 63% (and thus equals $1/e$ (~ 0.37) of the surface temperature oscillation) is given by the skin depth δ:

$$\delta = \sqrt{\frac{kP}{\rho c \pi}} \tag{5.1}$$

where P is the time period of variations (for seasonal changes, $P = 1$ martian year), k the thermal conductivity, ρ the density and c the specific heat capacity of the considered soil type. With thermal properties similar to those of Fig. 5.2a, $\delta = 5.4$ m. At latitudes higher than 60°, methane clathrate stability zone is shallower than this annual skin depth and will therefore be influenced by seasonal variations. For Fig. 5.2c, δ is 3 times smaller, which makes the seasonal changes in the clathrate stability zone significant beyond a latitude of 75°.

5.1.3 Heat flow

The base of methane CSZ being located several kilometers deep in the martian subsurface, its variations in depth are highly affected by the local heat flow as shown in Fig. 5.3, where calculations have been made for an ice-cemented soil. As expected, the depth up to which the stability zone extends decreases with increasing heat flow. For instance, the methane clathrate stability zone extends until 15 km deep at the equator when the heat flow is 14 mW m^{-2}, while its base is 2 times shallower with a heat flow of 25 mW m^{-2}. This behavior has significant implications for clathrate formation on Early Mars where surface heat flows were quite high compared to present day values and will be discussed later.

5.1.4 Presence of magnesium perchlorate

Salts are thermodynamic clathrate inhibitors (Sloan and Koh, 2007) and several ones such as chlorides and perchlorates have been identified in the southern highlands of Mars where recurring slope lineae are present (Osterloo et al., 2008; Ojha et al., 2015). Perchlorates have been identified as well by the Phoenix lander (Hecht et al., 2009). The presence of salts

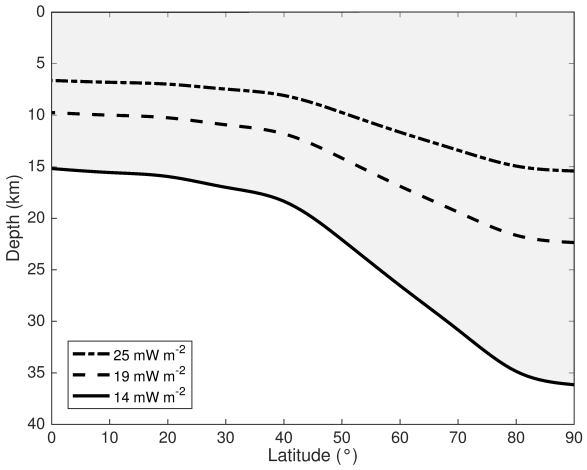

Figure 5.3: Depth of the base of methane clathrate stability zone as a function of latitude for different values of the heat flow q (14, 19 and 25 mW m^{-2}).

in the system is important in the determination of CSZ as it affects the activity of water which affects both the freezing point of pure water and the clathrate stability conditions. As seen in section 3.4, when salinity increases resulting in a decrease of water activity, the dissociation curve of clathrate hydrates is shifted to lower temperature and higher pressure. The change in both CH_4 and CO_2 CSZ in martian subsurface in the presence of high salinity brines, including NaCl and $CaCl_2$ eutectic brines, has been investigated by Elwood Madden et al. (2007). Increasing salinity induces an upward shift of the base of the stability zone and therefore reduces its thickness. For example, CH_4 CSZ at the equator is reduced compared to the predicted one in presence of pure water by about 33% in the presence of eutectic NaCl brine and about 69% in the presence of eutectic $CaCl_2$ brine (Elwood Madden et al., 2007). The decrease of CO_2 CSZ, whose the base is located shallower than the one of methane clathrate, is slightly less pronounced (Elwood Madden et al., 2007).

Here, we investigate the effect of perchlorates on the methane clathrate stability zone, especially magnesium perchlorate ($Mg(ClO_4)_2$) that exhibits one of the lowest eutectic temperature of all salts, 206 K (Chevrier et al., 2009). Given the lack of experimental equilibrium data for CH_4 clathrate hydrates in the presence of perchlorates, the dissociation pressure corresponding to a temperature larger than the eutectic temperature has been estimated assuming slopes comparable to the pure water

system, similarly to the approach of Elwood Madden et al. (2007) for systems with eutectic NaCl and $CaCl_2$ brines. As shown in Fig. 5.4, the presence of magnesium perchlorate brines, in addition to shifting the base, significantly affects the top of the stability zone at low latitudes. At the equator, CH_4 clathrates are stable deeper than 300 m in the presence of eutectic $Mg(ClO_4)_2$ brine and their stability zone has a thickness of a few hundred meters.

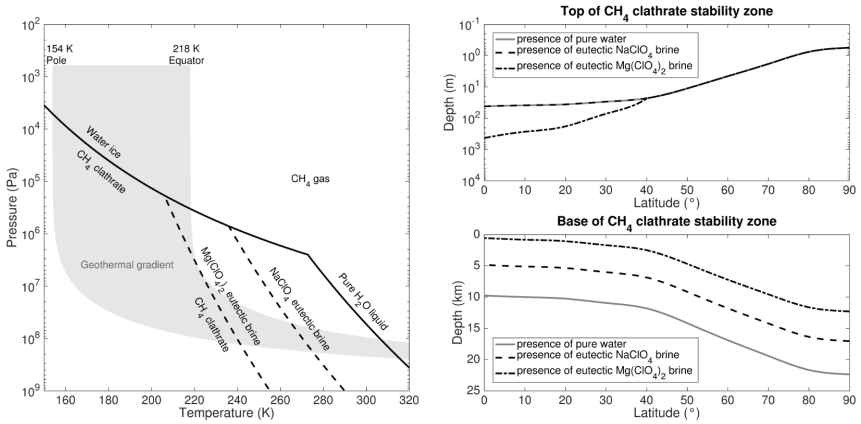

Figure 5.4: (Left) Methane clathrate stability fields in the presence of pure water, eutectic $NaClO_4$ brine and eutectic $Mg(ClO_4)_2$ brine. The shaded area represents an example of martian geothermal gradients over all latitudes calculated assuming a basaltic mineralogy with water ice filling the pore spaces. The heat flow is taken equal to 19 mW m^{-2} (Right) The corresponding depth of the top and the base of the CH_4 clathrate stability zone in the martian crust.

Elwood Madden et al. (2007) proposed that the interactions with high salinity brines could dissociate methane clathrates at depth, as the base of their stability zone experiences an upward shift in the presence of salts. Once released, CH_4 free gas would diffuse through fracture zones to reach the surface. Here, we showed that the presence of magnesium perchlorate affects not only the base of CSZ but also the near-surface stability of methane clathrates at low latitude and in particular in equatorial regions. When the concentration of this salt increases in the system, due to water-rock interactions or evaporation, leading thereby to a decrease of water activity, it could result in destabilization of equatorial methane clathrates located in the first few hundred meters below the surface. However, in order to study this process in more details, experimental equilibrium data of methane clathrates in the presence of perchlorates would be necessary.

5.1.5 Initial gas phase

The stability conditions of clathrate hydrates depend also on the relative abundance of the different guests. For example, increasing the CO_2 content in binary CH_4-CO_2 clathrates decreases the formation pressure, allowing clathrates to be stable at shallower depth (Chastain and Chevrier, 2007). This behavior is expected to be similar in mixed CO_2-CH_4-N_2-Ar clathrates when amounts of nitrogen and argon available for clathrate formation are very small compared to the CO_2 content. Indeed, this can be seen in Fig. 5.5 where the dissociation pressure of mixed CO_2-CH_4-N_2-Ar clathrates has been calculated for different abundances of methane in the initial gas phase and assuming that the ratios between CO_2, N_2 and Ar are similar to those measured in the present martian atmosphere. The addition of methane in these clathrates increases well the dissociation pressure in the same temperature conditions.

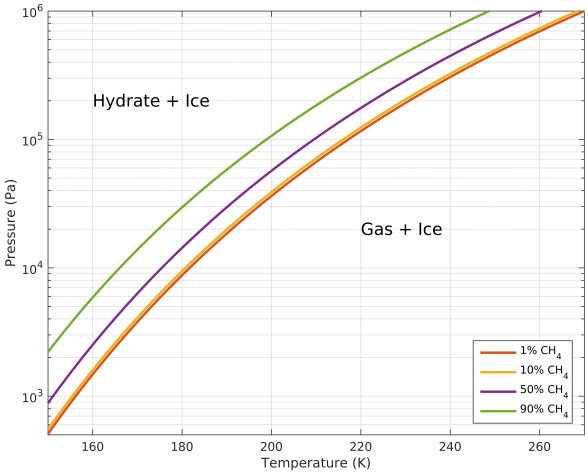

Figure 5.5: Phase diagram of mixed CO_2-CH_4-N_2-Ar clathrates for different abundances of methane in the initial gas phase. The ratios between CO_2, N_2 and Ar are similar to those measured in the present martian atmosphere.

5.1.6 Sloping surface

As mentioned previously, slopes considerably affect surface and subsurface temperatures and thus clathrate stability. In Fig. 5.6 and 5.7, the stability depth of methane clathrate has been calculated as a function of latitude considering pole-facing and equator-facing slopes respectively.

For these simulations, daily average surface temperatures over the martian year have been computed using the model of section 4.3.1 for a flat surface and slopes of 30°and 60°, and the corresponding stability depths for CH_4 clathrate have been determined. When clathrates are stable from several tens of meters under the surface, as is the case at low latitude, their stability field will not be reshaped with time by seasonal changes in surface temperature. However, this is not the case for shallow stability zone, which will be closer to the surface in winter and deeper during summer. The depth reported in Fig. 5.6 and 5.7 is the maximum depth reached during the martian year by the top of the stability zone.

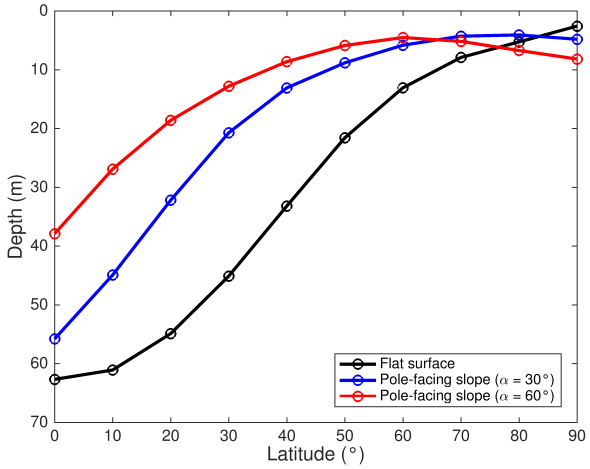

Figure 5.6: Depth of methane clathrate stability zone as a function of latitude in an ice-cemented soil. Calculations have been made for a flat surface (black curve) and pole-facing slopes of 30°(blue curve) and 60°(red curve).

As shown in section 4.3.1 for 40°S and 35°N, pole-facing slopes present a lower annual mean surface temperature compared to a flat surface, which implies that the methane clathrate stability zone will be shallower under a sloping surface oriented towards north in the northern hemisphere or towards south in the southern hemisphere. Indeed, this behavior can be observed in Fig. 5.6, where below 60° of latitude the stability field of CH_4 clathrate is found deeper under a flat surface than the one below a pole-facing slope of 30°, which is itself deeper than the calculated one with a 60° slope. At 70° and 80° of latitude, the annual average surface temperature estimated with a slope angle of 60° becomes more important than that predicted with a 30° slope and a flat surface, respectively, and the stability zone is moved accordingly as seen

in Fig. 5.6. A similar shift happens at the pole for the stability field determined with a 30° slope. When investigating the behavior of the CH_4 clathrate stability zone under equator-facing slopes, we expect to observe a trend opposite to that noted above since the annual mean temperature on these slopes is usually greater than on a flat floor. Indeed, this can be seen in Fig. 5.7, where the stability zone of methane clathrate is shallower under horizontal floor than below equator-facing slopes, except at low latitude where annual mean temperature is smaller on sloping surface. This last behavior is interesting when studying clathrate stability in equatorial regions, especially below crater walls.

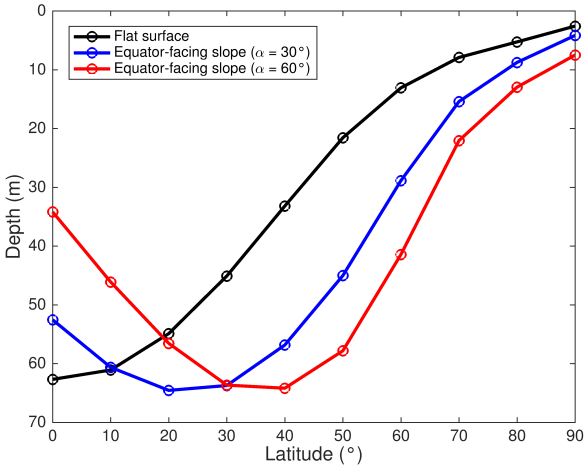

Figure 5.7: Depth of methane clathrate stability zone as a function of latitude in an ice-cemented soil. Calculations have been made for a flat surface (black curve) and equator-facing slopes of 30°(blue curve) and 60°(red curve).

We showed that at the equator the CH_4 stability field is closer to the surface when the surface is tilted either to the north or to the south. In the following, we thus apply our model to areas where local detections of methane have been reported, that is to say Gale crater (Webster et al., 2018) and the source region centered near 30°N (Mumma et al., 2009), to determine which slope angle brings the stability zone closest to the martian surface. For these simulations, the subsurface is divided in two layers. The upper soil layer extends over one meter and has thermal properties consistent with observations (Vasavada et al., 2017; Putzig and Mellon, 2007) and heat flow models (Parro et al., 2017) (Gale crater: $\rho = 1600$ kg m^{-3}, $c = 630$ J kg^{-1} K^{-1}, thermal inertia $I = 300$, albedo $= 0.2$, surface heat flow $q = 18.5$ mW m^{-2}; 30°N: $\rho = 1600$ kg m^{-3},

c = 800 J kg^{-1} K^{-1}, thermal inertia I = 250, surface heat flow q = 16 mW m^{-2}). The second layer has thermal properties representative of dry basalt. The variations of stability depth for CH_4 clathrate as a function of the slope angle at Gale crater and at 30°N are represented in Fig. 5.8 and 5.9 respectively. As a reminder, this depth is the deepest one reached by the stability zone over a martian year.

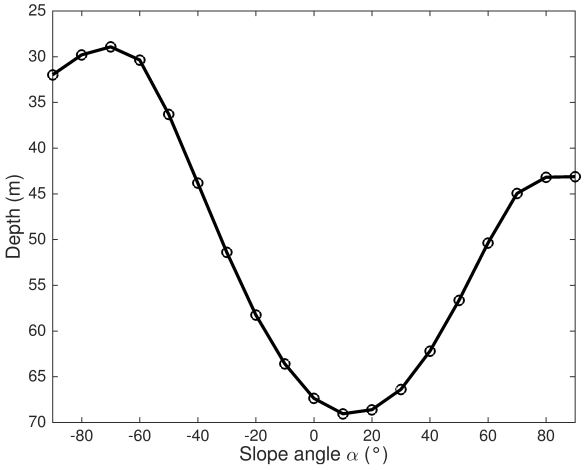

Figure 5.8: Depth of methane clathrate stability zone as a function of slope at Gale crater (-4.6°N). Equator-facing slopes are shown as positive and pole-facing as negative.

In accordance with the results obtained above, pole-facing slopes allow methane clathrate to be stable nearer to the surface than with a flat ground, the closest stability zone at -4.6°N and 30°N occurring with a slope angle of 70° and 60° respectively. At Gale crater latitude, equator-facing slopes tilted of 30° or more also bring the clathrate stability zone closer to the surface with a maximum efficiency for almost vertical slopes, although the shallowest stability depth reached is still 1.5 larger than that estimated with pole-facing slopes. At 30°N, an equator-facing slope, whatever its inclination angle, always leads to deeper stability depths compared to a flat surface.

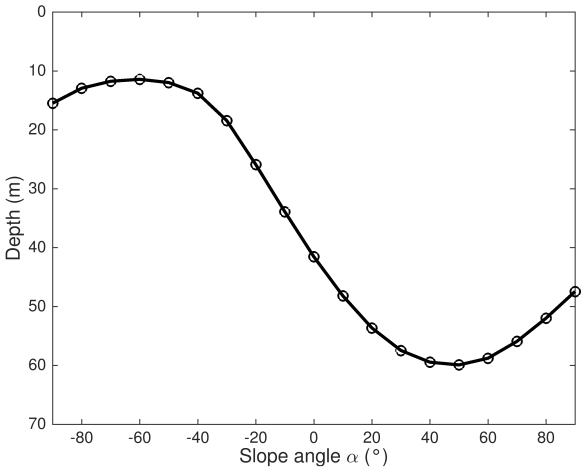

Figure 5.9: Depth of methane clathrate stability zone as a function of slope at 30°N. Equator-facing slopes are shown as positive and pole-facing as negative.

5.2 Methane clathrate stability zone: Global maps

Previously, the stability zone of methane clathrate hydrates in the martian subsurface has been determined using present-day mean annual surface temperatures, except in section 5.1.6. However, seasonal variations in temperature can affect the CSZ, especially at high latitude. Here, fluctuations of the clathrate stability depth over the martian year are studied and global maps of the maximum depth reached by the top of CSZ are obtained. The latter represents therefore the depth from which clathrate hydrates remain unaffected by seasonal cycles. For these simulations, the subsurface model extends to 100 m deep and mixed CO_2-CH_4-N_2-Ar clathrates are considered with ratios between CO_2, N_2 and Ar comparable to those measured on Mars.

At first, in order to have an idea of the kind of variations experienced by the stability zone, we present in Fig. 5.10 the evolution over time of the top of CSZ for clathrates formed from a gas phase with 90% of methane, at Phoenix landing site. At the beginning of the year, around $L_S = 25°$, the CSZ is the closest to the surface with a depth of ∼2 m. Then the top of the stability zone is shifted downwards with time due to increasing surface temperature and reaches its maximum depth (∼5 m) around $L_S = 198°$. Then, the top of the clathrate stability zone approaches again the surface due to the decrease of surface temperature.

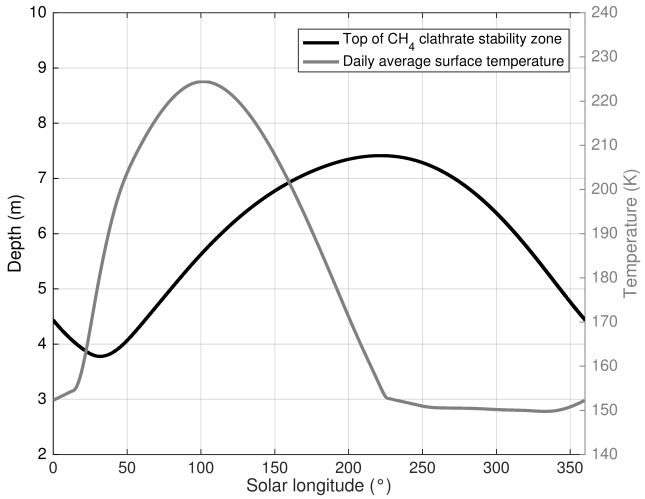

Figure 5.10: Variation over the year of the top of methane CSZ in the subsurface for clathrates formed from a gas phase with 90% CH_4 and daily average surface temperature at Phoenix landing site. Temperature variation is taken from MCD5.2.

The depth from which CH_4-rich clathrates (90% CH_4 in the initial gas phase) remain unaffected by seasonal variations in surface temperature within the martian subsurface at present-day is represented in Fig. 5.11. The top of CSZ has been calculated, following the model described in section 4.3.2, every 5 degrees and then interpolated every degree. Local detections of methane are reported in black: Gale crater (Webster et al., 2015, 2018) is represented as a black star, while Syrtis Major, Terra Sabae and Nili Fossae (Mumma et al., 2009) are included in the black rectangle.

At present-day, as stability conditions of methane clathrates are met in the near subsurface of Mars, the spatial variation of the top of their stability zone is strongly dependent of mean annual surface temperature. Consequently, CH_4-rich clathrate hydrates are stable closer to the surface at high latitude (few meters deep) and deeper in equatorial areas (few tens of meters deep) due to the larger surface temperature in these regions. By taking into account the thermal inertia observed by MGS TES (Putzig and Mellon, 2007) to set the thermal properties of the upper layer in our subsurface model and then increasing the thermal conductivity of the second layer to correspond to dry basalt, we found that the stability zone of CH_4-rich clathrates is the deepest in regions where

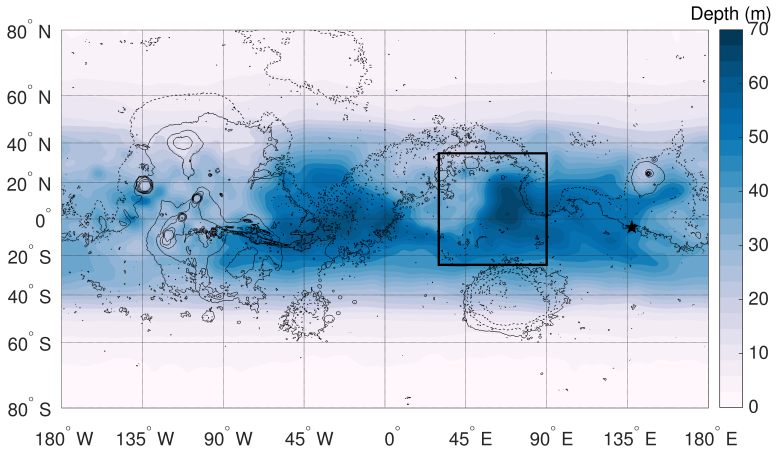

Figure 5.11: Depth (m) of the top of clathrate stability zone in present-day martian subsurface for CH_4-rich clathrates formed from a gas phase with 90% of methane. The first layer of the thermal model has properties that fit with the thermal inertia derived from MGS TES observations (Putzig and Mellon, 2007), while the second layer has properties representative of dry basalt or ice-cemented soil depending on the latitude. Local detections of methane are reported in black: Gale crater (Webster et al., 2015, 2018) is represented as a black star, while Syrtis Major, Terra Sabae and Nili Fossae (Mumma et al., 2009) are included in the black rectangle.

methane has been locally reported, especially in the area observed by Mumma et al. (2009) where it is located ∼68 m deep and it extends over several kilometers in the martian subsurface. At this depth, clathrates can not be affected by seasonal changes in temperature. However, the addition of other gas species in clathrates can shift their stability zone closer or further away from the martian surface depending on the guest composition. As mentioned previously and modeled by Chastain and Chevrier (2007) and Root and Elwood Madden (2012), the addition of CO_2 in CH_4 clathrate hydrates decreases the dissociation pressure in the same temperature conditions, allowing them to be stable at shallower depths. The spatial variation of the top of CSZ for clathrates formed from a gas phase containing 1% CH_4 (the main component is therefore CO_2) is shown in Fig. 5.12. We observe the same pattern as in Fig. 5.11 but with less important depths, the largest stability depth being 28 m. Note that if the thermal properties of the martian soil are kept identical to those derived from TES MGS observations in the second layer

of the subsurface model, the conditions for CH_4-rich clathrate stability are never met between 50°N and 50°S, as it can be deduced from Fig. 5.2d. Moreover, we found that methane clathrates located at any depth of their stability zone in the dark blue areas in Fig. 5.11 are necessarily destabilized in the presence of eutectic $Mg(ClO_4)_2$ brine, the mean surface temperature of these regions resulting in a temperature profile too warm to cross the modified stability boundary of CH_4 clathrates. In other low latitude regions, the top of CSZ is shifted downwards, as shown in section 5.1.4, with a maximum shift between 300 and 400 m.

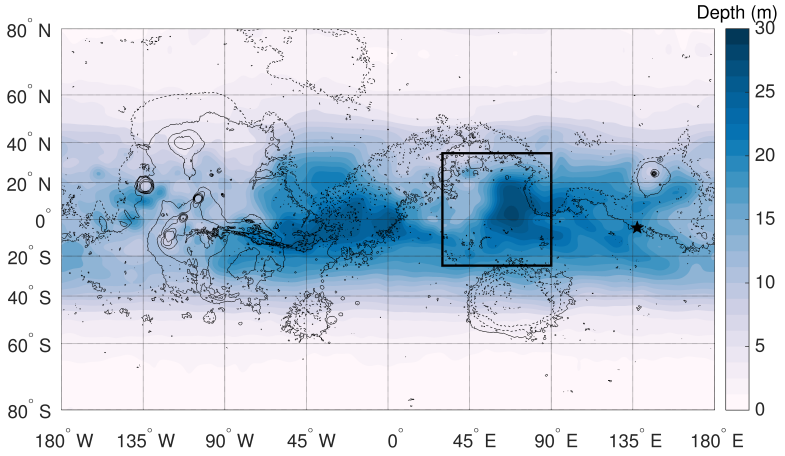

Figure 5.12: Depth (m) of the top of hydrate stability zone in present-day martian subsurface for clathrates formed from a gas phase with 1% of methane. The first layer of the thermal model has properties that fit with the thermal inertia derived from MGS TES observations (Putzig and Mellon, 2007), while the second layer has properties representative of dry basalt or ice-cemented soil depending on the latitude. Local detections of methane are reported in black: Gale Crater (Webster et al., 2015, 2018) is represented as a black star, while Syrtis Major, Terra Sabae and Nili Fossae (Mumma et al., 2009) are included in the black rectangle.

If methane is produced at depth in the martian crust, CH_4 clathrates should be formed preferentially at the base of the cryosphere (see section 3.5), although methane would gradually diffuse through the overlying ice and could thus be trapped in shallower clathrate reservoirs. Accordingly, the depth of cryosphere's base has been investigated using our subsurface model where thermal properties are representative of ice-cemented soil to determine at which depth a temperature of 273.15 K is reached.

The result is shown in Fig. 5.13. It can be seen that the depth at which the transition between pure liquid water and water ice occurs is the shallowest (∼5 km) where Mumma et al. (2009) reported observations of local methane plume. Therefore, methane that would be emitted by clathrates located at the base of the cryosphere, would have to be transported through the crust along a shorter pathway in the Nili Fossae, Terra Sabae and Syrtis Major regions before to be released in the martian atmosphere. If high salinity fluids are present, the transition between brines and ice is even closer to the surface depending on the salt composition.

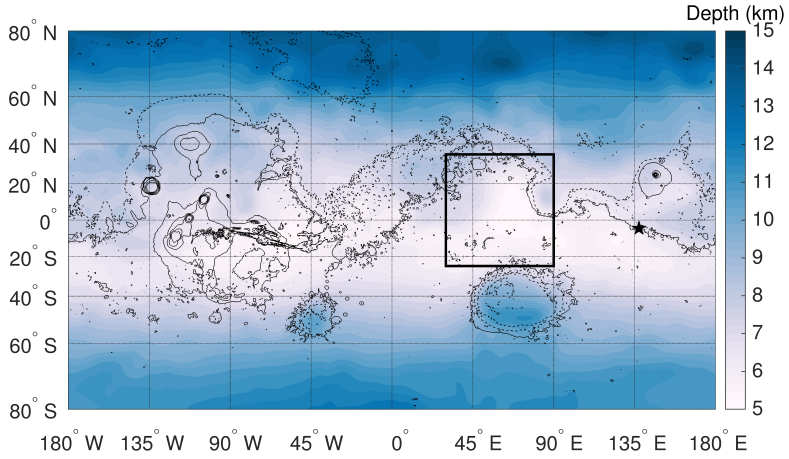

Figure 5.13: Depth (km) of the base of the cryosphere in present-day martian subsurface. Local detections of methane are reported in black: Gale Crater (Webster et al., 2015, 2018) is represented as a black star, while Syrtis Major, Terra Sabae and Nili Fossae (Mumma et al., 2009) are included in the black rectangle.

5.3 Variability of methane trapping

The trapping in clathrates of the different species present in the initial gas phase depends on the interactions between the guest molecules and the clathrate cages, as well as the partial pressures of the gases present during and after formation. Fig. 5.14 shows the fraction of methane in mixed CO_2-CH_4-N_2-Ar clathrates as a function of the CH_4 initial abundance in the gas phase for structures I and II. In the presence of CO_2, the formation of CH_4-rich clathrate hydrates is possible only if the initial gas

phase is enriched in methane (Thomas et al., 2009). Moreover, methane trapping is slightly enhanced when formation temperature increases. At 270 K, to form clathrates trapping 50 % of methane in their cavities, the initial gas phase must contain about 68 % CH_4 and 57 % CH_4 for structures I and II respectively.

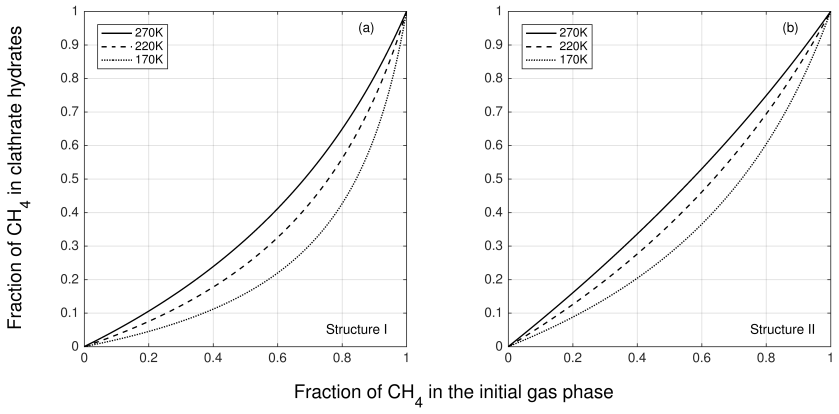

Figure 5.14: Fraction of CH_4 incorporated in mixed CO_2-CH_4-N_2-Ar clathrate hydrates as a function of the CH_4 fraction in the initial gas phase for different temperatures. The ratios between CO_2, N_2 and Ar are similar to those measured in the present martian atmosphere. Calculations have been made at the dissociation pressure of clathrates.

Here, we investigate the effect of gas phase composition on clathrate stability and on guests abundance by considering the CO_2-CH_4-N_2 and CO_2-CH_4-H_2 mixtures. Fig. 5.15 to 5.16 represent the formation pressure and the evolution of guests abundance, as a function of CH_4 mole fraction in the gas phase, in binary CO_2-CH_4 and ternary CO_2-CH_4-N_2 and CO_2-CH_4-H_2 sI clathrates at 270 K, respectively. The ratio between CO_2 and N_2/H_2 in the system is assumed to be 1. Firstly, it can be seen that the incorporation of nitrogen or hydrogen in mixed CO_2-CH_4 clathrates increases the formation pressure. For low CH_4 fraction (<0.1) in the gaseous phase, the formation pressure is multiplied by about 1.9 and 2 due to the presence of N_2 and H_2 respectively. Therefore these ternary clathrate hydrates, if present in the martian subsurface, should be more difficult to destabilize by surface processes. It can also be seen that nitrogen and hydrogen are weakly trapped in mixed CO_2-CH_4 sI clathrates, their maximum relative abundance reaching 0.07 and 3.45 10^{-3}, respectively, when no methane is present in the gas phase. However, their incorporation in clathrate hydrates allows a slightly better trapping of

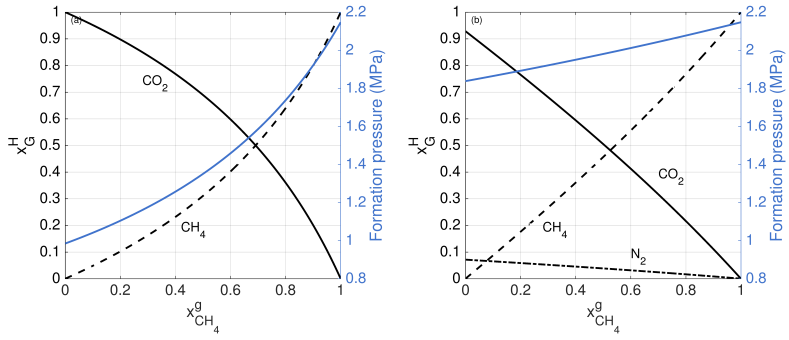

Figure 5.15: Formation pressure and fraction of the different guests x_G^H in (a) binary CO_2-CH_4 and (b) ternary CO_2-CH_4-N_2 sI clathrates at 270 K and as a function of CH_4 mole fraction in the gas phase. The ratio between CO_2 and N_2 in the gas phase is assumed to be 1.

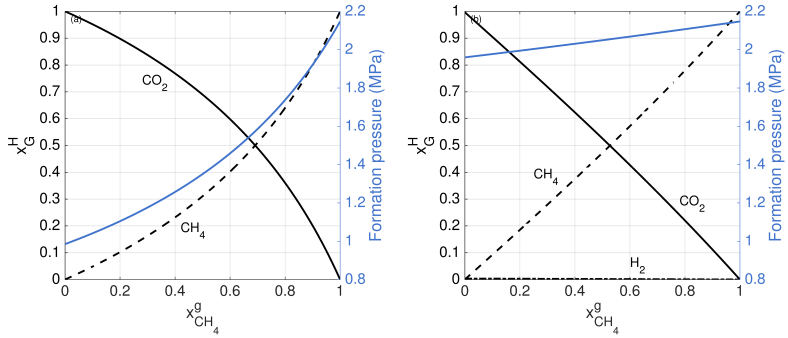

Figure 5.16: Formation pressure and fraction of the different guests x_G^H in (a) binary CO_2-CH_4 and (b) ternary CO_2-CH_4-H_2 sI clathrates at 270 K and as a function of CH_4 mole fraction in the gas phase. The ratio between CO_2 and H_2 in the gas phase is assumed to be 1.

methane. For example, in Fig. 5.16, CO_2-CH_4-H_2 sI clathrates trapping 50% of methane in their cavities are formed from a gas phase consisting of 53% CH_4. On the other hand, if the structure II is the one that crystallises, clathrate will trap a greater fraction of methane, similarly to what is observed in Fig. 5.14.

The guest abundance in clathrates as a function of the pressure at which they form is also investigated. Fig. 5.17 presents the CH_4 and CO_2 mole fractions in binary sI clathrate for a pressure range varying from their dissociation pressure to 10 MPa. Calculations were made at 270 K for an initial gas phase including 50% CH_4 and 50% CO_2. The intrigu-

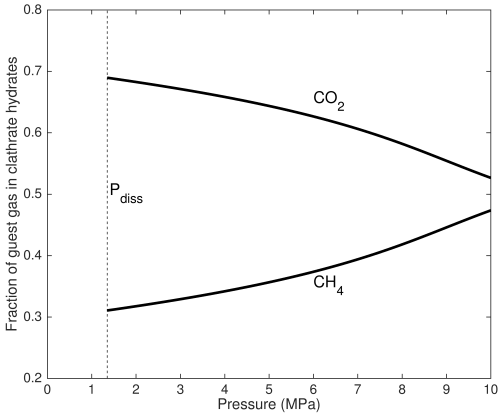

Figure 5.17: Mole fraction of CO_2 and CH_4 in binary sI clathrates at T = 270 K as a function of pressure. The gas phase consists of 50% CO_2 and 50% CH_4.

ing result is that with growth of pressure, the carbon dioxide fraction in clathrate decreases, while the methane content increases consequently. This rise in CH_4 mole fraction is quite pronounced with an increase by 53% between 1.35 and 10 MPa. Considering this, binary CH_4-CO_2 clathrates that would form at depth in the martian crust would contain a larger fraction of methane than shallow clathrates formed from a similar gas phase. Fig. 5.18 and 5.19 show the guest mole fraction at 270 K as a function of pressure for ternary CO_2-CH_4-N_2 and CO_2-CH_4-H_2 clathrates respectively. The trend observed previously where the CO_2 content in clathrate decreases and the CH_4 fraction increases with pressure is also present with the incorporation of N_2 and H_2 in clathrates.

5.4 Variation of clathrate stability zone in the past

On Early Mars, surface heat flows were quite high, with mean values between 60 and 70 mW m^{-2} 3.5 to 4 Gyr ago (see Fig. 4.9b), compared to a present day value of 19 mW m^{-2} (Parro et al., 2017). As shown in section 5.1.3, the clathrate stability zone strongly depends on the heat flow values and, as the cryosphere, has therefore spread deeper in the subsurface with the cooling of the planet. Methane was probably more abundant on Early Mars due to volcanism and hydrothermal activity and could have been trapped in the growing layer of permafrost with time (Pellenbarg

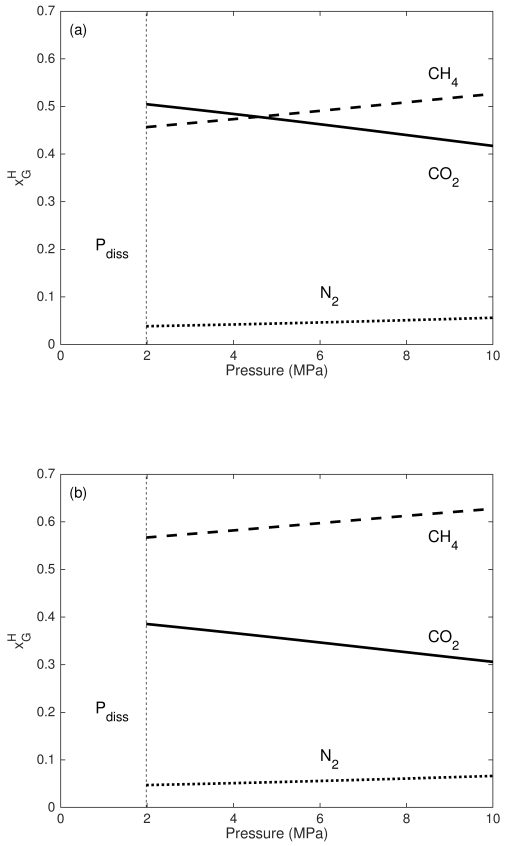

Figure 5.18: Mole fraction of CO_2, CH_4 and N_2 in ternary clathrates at $T = 270$ K as a function of pressure. The gas phase consists of 50% CH_4, 25% CO_2 and 25% N_2. Calculations are made for structures I (a) and II (b).

et al., 2003). The growth of the CSZ and cryosphere throughout the martian history cannot be expected to be monotonic or spatially uniform and is challenging to determine given the many poor constrained parameters like obliquity and solar luminosity variations, volcanic activity or impacts. However, we are interested here in the general trend adopted by the base of the clathrate stability zone following the decrease of the heat flow over time in order to better constrain its evolution and the depth of potential ancient clathrate reservoirs. Fig. 5.20 shows the estimated depth of the base of the cryosphere and the methane stability

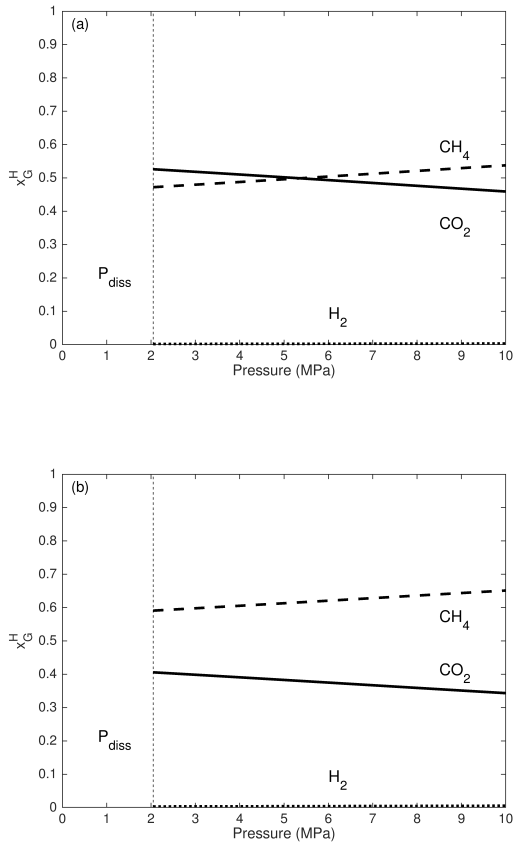

Figure 5.19: Mole fraction of CO_2, CH_4 and H_2 in ternary clathrates at $T = 270$ K as a function of pressure. The gas phase consists of 50% CH_4, 25% CO_2 and 25% H_2. Calculations are made for structures I (a) and II (b).

zone at the equator of Mars as a function of time for the two scenarios of the surface temperature presented in section 4.3.2. With the warm scenario, the mean surface temperature 4 Gyr ago is set to 273.15 K and the corresponding subsurface temperature profile is too warm to cross the stability boundary of CH_4 clathrates. Stability conditions for clathrates are met in the soil at around 3.8 Gyr, where mean surface temperature and heat flow dropped to 257 K and 67 mW m^{-2}, respectively. At that time period, the base of the stability field is found at about one kilometer deep and extends downwards with time. For the cold scenario, the

mean surface temperature is kept constant at 220 K. The base of CSZ is therefore located deeper in the crust reaching $\sim$ 2.3 km deep at 4 Gyr.

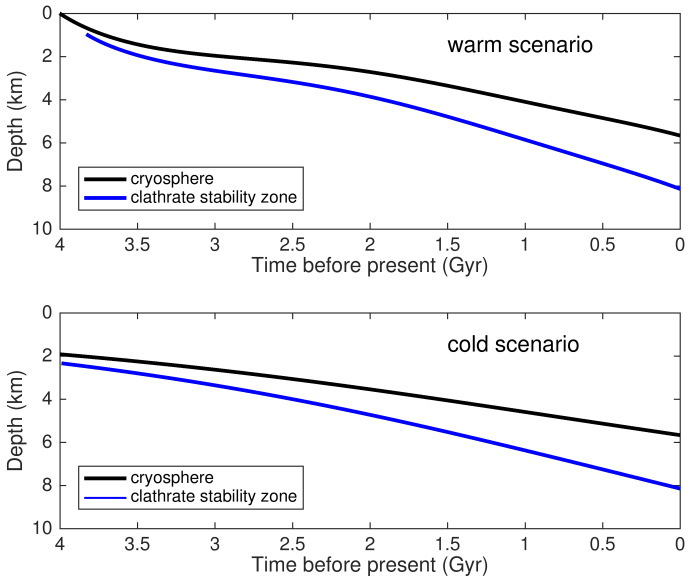

Figure 5.20: Evolution of the base of the martian cryosphere and the methane clathrate stability zone with time at the equator of Mars.

If the methane production has stopped early in the martian history, then formation of CH_4 clathrate reservoirs would have been limited to the stability zone associated to this time period. Thereafter, although the stability field of methane clathrate would have continued to expand with time, new clathrate formations would not have occurred without the addition of methane in the system. Moreover, obliquity changes should have dissociated a large part of near-surface methane clathrates, reducing the layer of clathrates entrapping methane from the Early Mars atmosphere. The obliquity of Mars varies chaotically with a pseudo-period of $\sim$120,000 Earth years and extreme values ranging from 0° to over 60° (Laskar et al., 2004) and the resulting temperature oscillations penetrate into the crust at a depth $\sim$250 times higher ($\delta \sim$ 1350 m) than that up to which the seasonal oscillations propagate. Nevertheless, Root and Elwood Madden (2012) have shown that some of near-surface methane clathrates may be preserved as metastable reservoirs over geologic time scales due to slow dissociation and diffusion rates.

5.5 Summary

On present-day Mars, the stability conditions of CH_4-rich clathrates are met in the shallow subsurface. These crystalline compounds can be stable very near the surface at high latitudes, and can be as close as 20 m to the surface in the tropics. However, the top of their stability zone is the deepest ($\sim$68 m) in regions where methane has been locally reported, especially in the area observed by Mumma et al. (2009). This depth is too important for clathrates to be affected by seasonal changes in temperature but we showed that the stability field is shifted upwards with tilted surfaces oriented towards the pole as these slopes experience colder surface temperature. The shallowest stability zone at -4.6°N and 30°N has been found to occur with a slope angle of 70° and 60° respectively. Moreover, at very low latitude, some equator-facing slopes can also bring the clathrate stability zone closer to the surface. At Gale crater latitude, this is the case for slope angles $\geq 30°$. In equatorial regions, the destabilization of methane clathrates by surface processes could thus be easier on crater walls, especially as sloped surfaces are more prone to landslides.

Based only on temperature determination, cryosphere should be less extended in the CH_4 source regions reported by Mumma et al. (2009). Methane released by clathrate dissociation at its base would thus be transported through the crust along a shorter pathway to be either trapped again in subsurface reservoirs or discharged in the martian atmosphere. In the presence of eutectic $Mg(ClO_4)_2$ brine, the base of methane CSZ is shifted upwards at depths of only a few hundred meters in equatorial regions with mean surface temperature of 218 K. In areas where this temperature is larger, such as methane detection regions, the subsurface temperature profile is too warm to cross the stability boundary of CH_4 clathrates. Migration events of high salinity fluids into clathrate-bearing rocks could thus trigger clathrate decomposition already at a few hundred meters deep and nearer to the surface in regions where CH_4 plumes have been observed.

Finally, we investigated the guest abundance in clathrates as a function of the pressure at which they form. In binary CO_2-CH_4 clathrates, it has been found that the carbon dioxide fraction in clathrate decreases while the methane content increases with the growth of pressure. Clathrates that would form at depth in the martian crust would thus contain a larger fraction of methane than shallow clathrates formed from a similar gas phase. If hydrogen, which is often involved in methane production mechanisms, is incorporated in clathrates, the trapping of methane is even enhanced.

Chapter 6

Transport of CH_4 and H_2O gases in the martian soil

Contents

6.1 Water vapor diffusion and ice stability 111

6.1.1 Ice stability key parameters 112

6.1.2 Ice stability at selected locations 119

6.2 Methane outgassing scenarios 124

6.2.1 Coupling with atmospheric models 129

6.3 Summary 133

This chapter is dedicated to the modelling of water ice stability and methane transport from shallow sources via the diffusive-adsorptive model presented in chapter 4.

On Earth, in regions where methane can accumulate within or below the permafrost layer, seasonal increases in the CH_4 flux have been recorded during warmer periods in areas of thawing permafrost (Christensen et al., 2004). Similarly, on Mars, when water ice evaporates during summer, it could enhance the diffusion of CH_4 located below the sublimating ice layer. Moreover, the loss of shallow ground ice removes confining pressure and puts buried clathrate hydrates in contact with the martian atmosphere, which could thus initiate their destabilization and the methane release. On the other hand, recondensation of water in pore spaces could significantly slow methane diffusion and seal the subsurface reservoir. Based on an experimental diffusion rate determined at 273 K, Elwood Madden et al. (2011) estimated the diffusion coefficient of methane through water ice under martian conditions using the Arrhenius equation and found a value of 2.1×10^{-14} m^2 s^{-1} at 220 K. Applying

the same method, we find a coefficient diffusion of 7.3×10^{-15} m^2 s^{-1} at 200 K. The maximum diffusion path length (see Fig. 6.1) for methane through an overlying ice layer has then been evaluated as a function of reservoir footprint using Fick's law and assuming that a total methane concentration as observed by Mumma et al. (2009) was released over a 120 day period. The methane concentration at the top of the clathrate stability zone is assumed to be 7700 mol m^{-3} (pure methane clathrate).

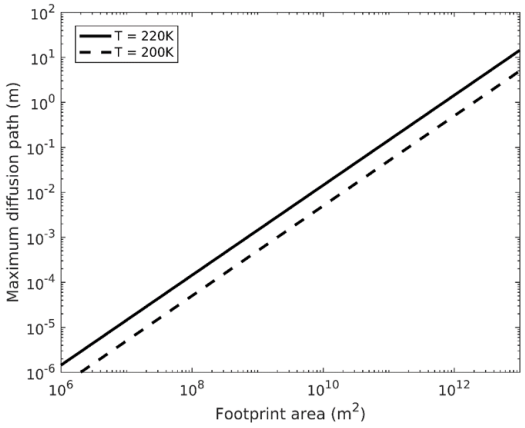

Figure 6.1: Maximum diffusion path length for methane through ice layer at 220 K and 200 K assuming total methane abundance as measured by Mumma et al. (2009). (Adapted from Elwood Madden et al. (2011).)

Results show that the maximum path length increases with the footprint area. For a total release surface as reported by Mumma et al. (2009) ($\sim 10^{13}$ m^2), the maximum distance over which methane can diffuse is 15 m at 220 K (representative of the average surface temperature in equatorial regions) and 5 m at 200 K (representative of the mean surface temperature in mid-latitude regions). These path lengths are smaller than the depth of the methane clathrate stability zone estimated in the previous chapter. In addition, the actual methane concentrations in the martian subsurface are likely much lower than the one assumed above with pure methane clathrates, which further reduces the diffusion path lengths. The seasonal or permanent presence of water ice in the regolith pores is thus a major parameter to take into account when studying possible methane release scenarios.

6.1 Water vapor diffusion and ice stability

Significant quantities of subsurface hydrogen have been observed in the close vicinity of the martian subsurface by the Gamma Ray Spectrometer onboard Mars Odyssey (Feldman et al., 2004). In equatorial/mid-latitude deposits, H_2O abundance is between 2% and 10% by mass. These hydrogen-rich areas may be due to hydrated minerals or adsorbed water (Jakosky et al., 2005). In mid- to high-latitude regions, observed hydrogen abundances reveal quantities up to 50% water by mass in some areas. This hydrogen may probably be in the form of buried ice deposits.

Data analysis and models suggest that ongoing atmosphere-regolith diffusive exchange plays an important role for the presence of ground ice. In addition to the formation of water frost, the atmosphere-subsurface interactions could involve the adsorption of water onto mineral surfaces and the hydration or deliquescence of salts. However, the details of water vapor exchange are still poorly known, partly because of the lack of experimental data concerning the diffusion coefficient. Indeed, this last parameter is essential to determine the survival time of ground ice in contact with a drier atmosphere or the rate at which the regolith can be refilled with subsurface ice from atmospherically derived vapor (Mellon and Jakosky, 1993).

Models based on vapor equilibrium between the atmosphere and the subsurface predict stable subsurface ice poleward of 55° latitude in both hemispheres (Mellon et al., 2004; Schorghofer and Aharonson, 2005). A key result of those models is that the ice table is located at a depth where the annual mean vapor density (in equilibrium with water ice) is equal to the annual mean vapor density at the surface (Mellon et al., 2004). Comparison with the observations suggests that ground ice has adjusted to the atmospheric humidity due to vapor diffusion across the regolith (Schorghofer and Aharonson, 2005). In Fig. 6.2, we calculated the equilibrium ice table at Phoenix landing site with parameters corresponding to the site-specific properties (Zent et al., 2010). First, the surface and subsurface temperatures are determined as a function of the ice table depth. It can be seen on Fig. 6.2 that the annual mean surface temperature increases slightly when water ice is very close to the surface. This is due to the enhancement of the thermal inertia with ice. Then, the vapor densities in the subsurface are computed using the saturattion vapor pressure $P_{\rm sat}$ (Equation 4.66), while the annual mean vapor density at the surface is calculated with MCD5.2 (Forget et al., 1999). The equilibrium ice table is found at a depth where the annual mean vapor densities at the surface and at the ice table are equal, that is to say $\sim$4 cm.

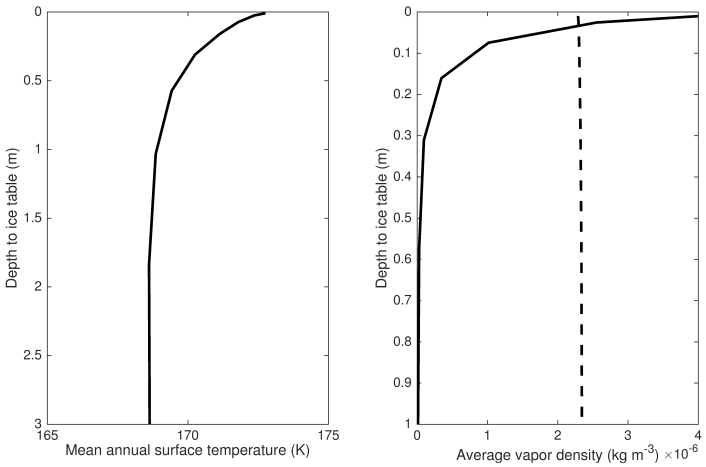

Figure 6.2: Mean annual surface temperature as a function of ice table depth (left) and mean vapor density at the ice table (solid line) and on the surface (dashed line) as a function of ice table depth (right) at Phoenix landing site.

As mentionned previously, slopes alter subsurface temperatures and thus the global equilibrium ice distribution. Taking them into account in the equilibrium models allows water ice to exist at locations where other models show it is unstable (Aharonson and Schorghofer, 2006). Finally, in order to study the evolution of near-surface ice with time, a dynamic (i.e. non-equilibrium) model, such as the one presented in chapter 4, has to be used. In the following, the atmosphere-subsurface water vapor exchange has been modelled to study the temporal evolution of the downward transport, ice redistribution and porosity changes. The evolution of near-surface ice is provided for different landing sites and regions of trace gas observations. When water ice turns out to be instable in the considered locations, the equilibrium model is then applied with slopes.

6.1.1 Ice stability key parameters

In this section, thermal conduction and water vapor transport in the martian subsurface are simulated using simplified conditions to demonstrate the influence of different parameters separately. In the next section, the most realistic conditions will be used to determine ice stability at selected locations.

An example for the accumulation of ice layer from atmospherically

derived water vapor during an annual temperature cycle (see Fig. 6.4) and under simplified conditions is represented in Fig. 6.3. The model calculation assumes similar inputs to Schorghofer and Aharonson (2005): a sinusoidal surface temperature variation with a period of one martian year (T_{mean} = 190 K), a constant daytime H_2O partial pressure P_0 = 0.1 Pa and no heat flow. As discussed in chapter 4, the effective diffusion coefficient is dependent on the soil pore geometry and thus on the presence of ice in pore spaces. Here, the diffusion coefficient is not ice dependent and is assumed to be $D_{eff} = 0.1(T/200\ K)^{3/2}\ cm^2\ s^{-1}$, the coupling between the different diffusion regimes (molecular and Knudsen diffusion) is therefore not taken into account. The thermal inertia I = 277 J m^{-2} K^{-1} $s^{-1/2}$, the volumetric heat capacity $\rho c = 1.28 \times 10^6$ J m^{-3} K^{-1}, the porosity Φ = 0.4 and the process of adsorption is not included. The results are shown for the eleventh year after starting with an ice-free regolith. A layer of frost migrates inward during the warming part of the cycle and fills the subsurface with ice.
The results of this section will be compared with Fig. 6.3, therefore the following model simulations use the same inputs as mentioned above, unless otherwise is indicated.

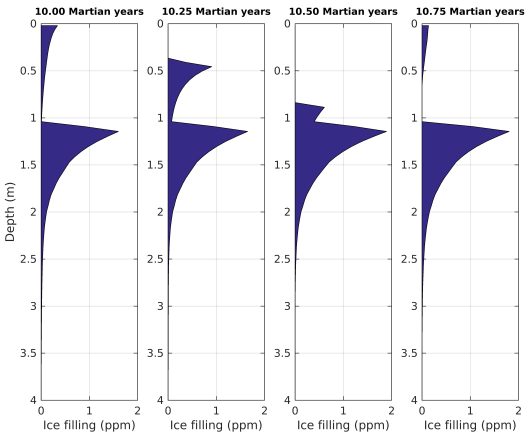

Figure 6.3: Instantaneous vertical profiles of the fraction of pore space filled with ice during the eleventh year after starting with an ice-free regolith. The corresponding vertical temperature profiles are shown in Fig. 6.4.

Thermal inertia

The thermal inertia depends on the soil density, the heat capacity and the thermal conductivity that control the temperature wave in the sub-

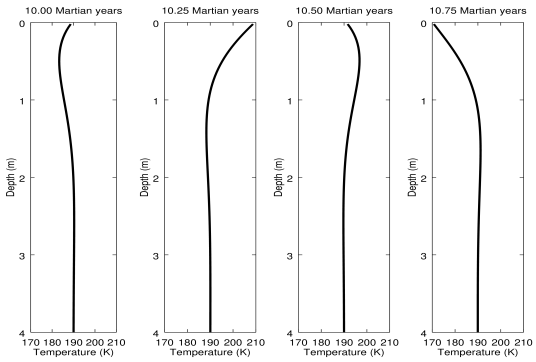

Figure 6.4: Instantaneous vertical profiles of the temperature associated to Fig. 6.3.

surface. Fig. 6.5 shows the ice filling profiles after ten martian years for different thermal inertias: 200, 500 and 800 J m^{-2} K^{-1} s$^{-1/2}$. For these simulations, the volumetric heat capacity has been kept constant and the thermal conductivity has been varied to correspond to the chosen thermal inertia. For higher values of the thermal conductivity the regolith conducts heat more efficiently and the temperature oscillations reach a greater depth. These temperature variations affect the amount of ice and the ice table depth. In the case of the thermal inertia equal to 800 J m^{-2} K^{-1} s$^{-1/2}$, the ice table depth is located around 3.5 m deep while it is at 0.75 m deep for a thermal inertia of 200 J m^{-2} K^{-1} s$^{-1/2}$. Most of the sites studied in this work have a thermal inertia around 280 J m^{-2} K^{-1} s$^{-1/2}$, the left panel in Fig. 6.5 is therefore the most representative.

Effective diffusion coefficient

The effective diffusion coefficient is dependent on the soil pore geometry as well as the properties of the diffusive gases. Its range starts in $\sim 10^{-3}$ m^2 s^{-1} and decreases strongly with the pore size of the subsurface. Note that the presence of ice in the pores affects the diffusion by reducing the pore space. Fig. 6.6 represents the ice filling fraction in pore space after ten martian years for different values of the effective diffusion coefficient. The left panel shows the ice filling for a diffusion coefficient of 10^{-4} m^2 s^{-1} which represents a pore size around 1 μm. The results of the mid and the right panels have been obtained with an effective diffusion coefficient of 10^{-5} m^2 s^{-1} and 10^{-6} m^2 s^{-1}, which corresponds to a pore size of 0.01 μm and 0.001 μm respectively. The amount of ice in the subsurface is ten times larger for a diffusion coefficient ten times larger. The ice table

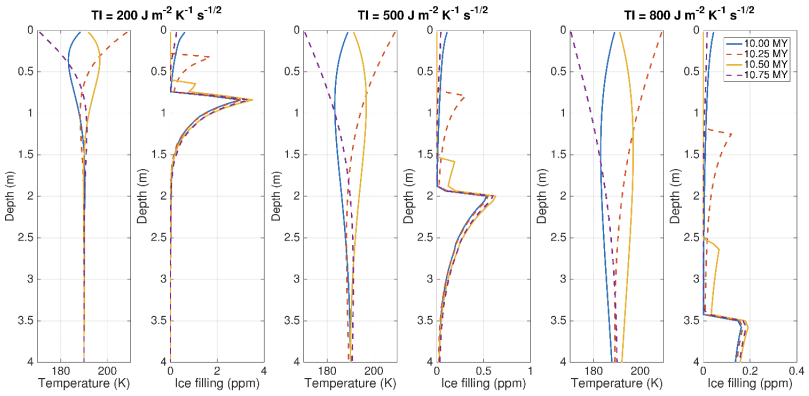

Figure 6.5: Subsurface temperatures and fraction of pore space filled with ice after 10 martian years for different thermal inertia.

builds up faster for higher values of the diffusion coefficient because of the larger vapor fluxes. However, the ice table depth is not affected by changes in the diffusion coefficient and the distribution pattern is similar in all cases.

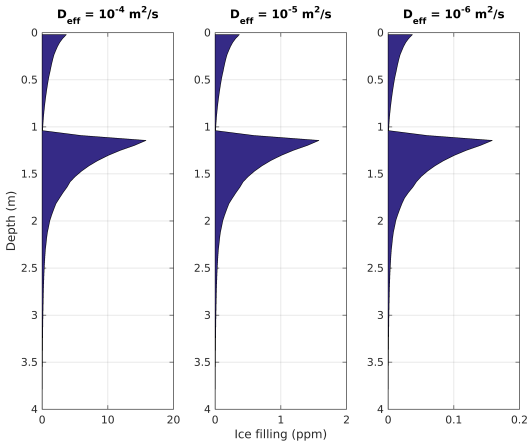

Figure 6.6: Ice filling after 10 martian years for different values of the effective diffusion coefficient D_{eff}.

Temperature

In Fig. 6.3, results have been obtained for a mean temperature of 190 K varying sinusoidally with an amplitude of 20 K. Here, we evaluate the

influence of two other mean temperatures: 180 K which is representative of Phoenix landing site and 200 K which is more characteristic of mid-latitude regions. Fig. 6.7 represents the annual evolution of ice filling fraction during the 11th martian year with the two selected temperatures. It can be seen that for a mean temperature of 180 K, there is a permanent ice table close to the surface, while for a mean temperature of 200 K, ice is only seasonally stable.

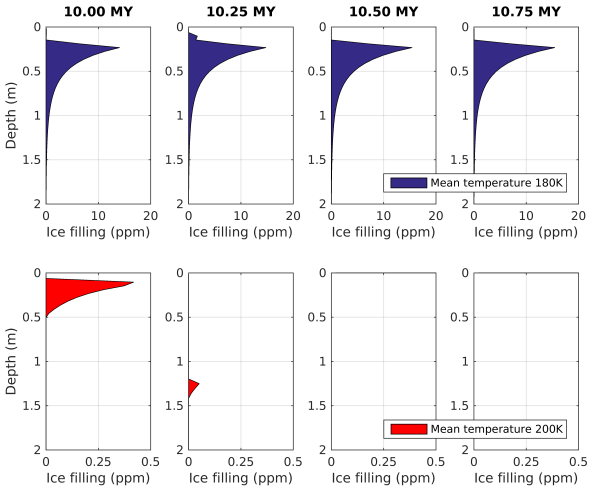

Figure 6.7: Ice filling after 10 martian years for a mean surface temperature of 180 K (top) and 200 K (bottom).

Atmospheric H_2O partial pressure

Here, the atmospheric H_2O partial pressure is changed compared to our reference results where the partial pressure was $P_0 = 0.1$ Pa.
Fig. 6.8 represents the evolution of the amount of ice in pore space for a constant daytime partial pressure of 0.02 Pa and 0.5 Pa. The results differ from the reference in the amount of ice, the distribution pattern and the ice table depth. It can be seen that for $P_0 = 0.02$ Pa, the ice is only seasonally stable with a maximum ice filling of 0.1 ppm at 10.00 Mars years while there is no ice during the second half of the year. When $P_0 = 0.5$ Pa, the ice is stable near the surface with an ice fraction in pore space reaching 75 ppm at 10.00 Mars years. Then the amount of ice slightly increases at 10.25 Mars years to 80 ppm and stays constant during the rest of the year.

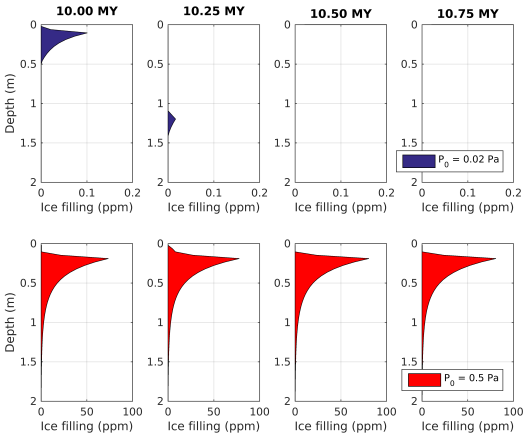

Figure 6.8: Ice filling after 10 martian years for a constant daytime H_2O partial pressure of 0.02 Pa (top) and 0.5 Pa (bottom).

Heat flow

The influence of the heat flow on ice stability is investigated by comparing ice filling showed in Fig. 6.3 with a model simulation using a heat flow of 0.025 W/m^2, the likely maximum value, according to Parro et al. (2017). Fig. 6.9 compares the results obtained at the beginning of the 11th martian year. The ice distribution is affected by the heat flow due to the increase of the temperature. Indeed, the average temperature increases with depth and is around 191.7 K at 4 meters deep. Going down from the ice table, the ice filling does not decrease smoothly like the distribution without heat flow and is close to zero around 1.65 m deep.

Adsorption

Here, we investigate the effects of adsorption that were not taken into account in the previous simulations. Fig. 6.10 presents an example of the evolution of the ice filling during the 11th Mars year with and without adsorption. The right panel shows much larger variations in the amount of ice compared to the case without adsorption. In addition, there is no direct pattern of the downward migration of ice but a slight trace can be seen around 1.2 m which can be interpreted as the ice table. It can also be seen that much more ice is located in the upper meter of the regolith compared to the left panel. The density of adsorbed water depends on the specific surface area of the soil. Simulations including adsorption

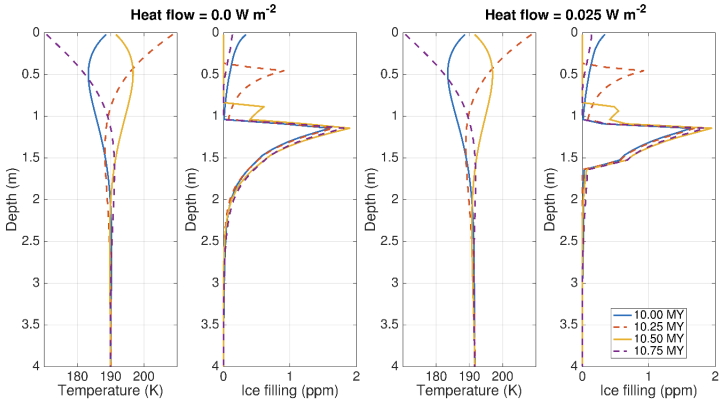

Figure 6.9: Subsurface temperatures and fraction of ice in pore space after 10 martian years, calculated with a heat flow of 0.0 W/m^2 (left) and 0.025 W/m^2 (right).

showed that the amount of ice increases with the specific surface area. Moreover, as seen in Fig. 6.11, the temporal change in the total mass of ice in the subsurface has a larger amplitude with adsorption than without. The period and the slope of this variation are identical for both situations which indicates the same net accumulation. However, the vertical profile of water vapor density and the quantity of water exchanged periodically are strongly affected by adsorption.

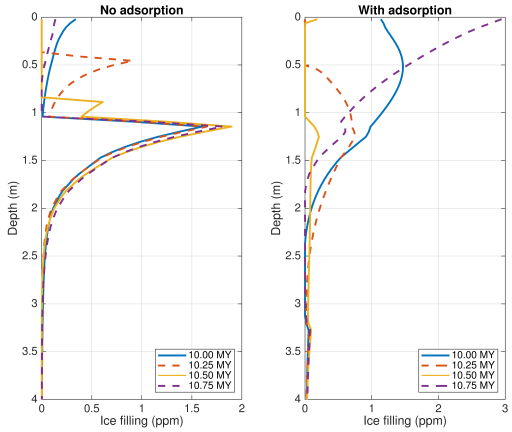

Figure 6.10: Ice filling profiles after 10 martian years calculated without adsorption (left) and with adsorption (right).

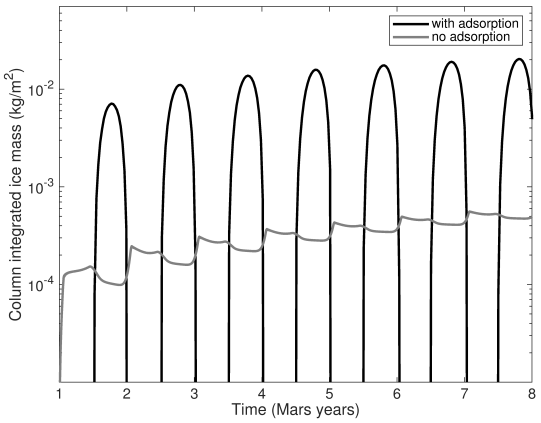

Figure 6.11: Ice accumulation as a function of time with a mean temperature of 190 K.

Results presented in this section show that the loss of ground ice overlying a clathrate deposit could occur by a rise in temperature or a decrease in water partial pressure.

6.1.2 Ice stability at selected locations

This section is dedicated to the study of the evolution of near-surface ice and the water vapor exchange between the subsurface and the atmosphere at Phoenix and Curiosity landing sites as well as one of the regions where methane has been detected centered in 30°N, 100°E (Mumma et al., 2009). The following simulations take into account the different diffusion regimes (Knudsen and molecular diffusion), adsorption and the influence of ice redistribution on the effective diffusion coefficient.

Trace gas observations region

For the investigation of the water vapor exchange between the subsurface and the atmosphere in the areas where trace gases have been observed, we chose to study one of the source regions observed by Mumma et al. (2009) centered near 30°N, 100°E. The evolution of the atmospheric water partial pressure, used as a boundary condition in the subsurface transport model, has been calculated using TES MGS observations (Smith, 2002) whenever available, otherwise using MCD5.2 (Forget et al., 1999). The water vapor column abundance and the water condensation level observed by TES as a function of solar longitude L_S and latitude were

provided by M.D. Smith. Fig. 6.12 shows the good match between H_2O partial pressure from MCD5.2 and retrieved from TES MGS observations at 30°N, 100°E. The thermal inertia used in the model is 250 J m^{-2} K^{-1} $s^{-1/2}$, which is representative of a dry unconsolidated soil. The volumetric heat capacity is the same as in previous simulations and the thermal conductivity equals 0.05 W m^{-1} K^{-1}. For this region, a mean surface heat flux of 0.016 W m^{-2} has been chosen (Parro et al., 2017).

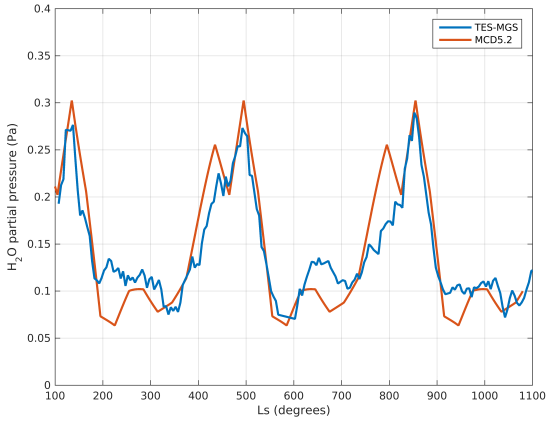

Figure 6.12: H_2O partial pressure at 2pm observed by TES MGS (blue) and simulated by MCD5.2 (orange) at 30°N, 100°E during three martian years.

The simulations showed that near-surface ice is not stable anytime at 30°N, 100°E at present-day Mars. Nevertheless, water vapor exchange between the atmosphere and the subsurface occurs on diurnal and seasonal scales. The variations of the surface water vapor flux have been calculated over the year and are shown at Fig. 6.13 for different solar longitudes. A flux less than zero represents H_2O passing from the atmosphere into the ground. During the night, the atmosphere is very stable near the surface and the regolith is slowly depleting the atmosphere of water vapor. In the morning there is a sudden pulse of water vapor in the subsurface. At this time, the atmosphere begins to become convective and there is an enrichment of water vapor in the lower atmosphere. As the temperature increases, desorption of water occurs causing soil vapor concentrations to increase. Around 10am, H_2O concentrations become higher than those of the atmosphere and the flow is reversed. This process continues throughout the day until the temperatures decrease. As expected, the flux is more important during warmer seasons.

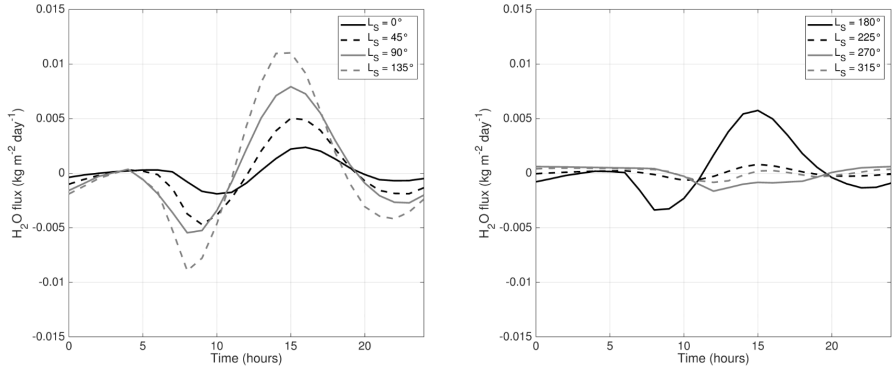

Figure 6.13: Seasonal variations of H_2O flux between the subsurface and the atmosphere at 30°N, 100°E between $0°<L_S<135°$ (left) and $180°<L_S<315°$ (right).

The equilibrium ice table depth as a function of slope at 30°N is represented in Fig. 6.14. Pole-facing slopes are colder than equator-facing slopes and allow the existence of subsurface ice for slopes $\geq 28°$, for which the mean surface temperature is smaller than the frost point $T_f = 198$ K.

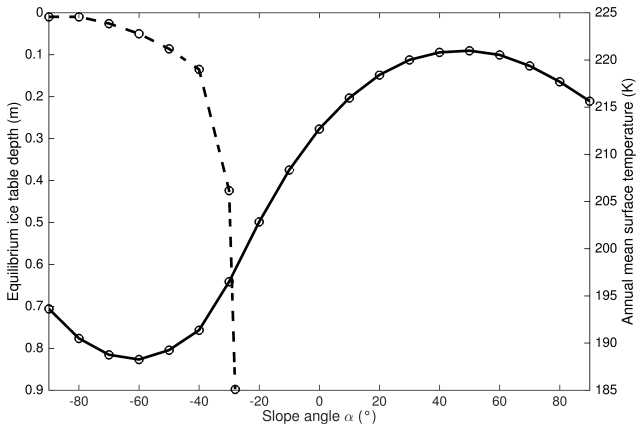

Figure 6.14: Mean surface temperatures (solid line) and equilibrium ice table depth (dashed line) as a function of slope at a latitude of 30°N. Equator-facing slopes are shown as positive and pole-facing as negative.

Curiosity landing site

Curiosity rover landed in Gale crater, an impact crater about 154 km in diameter, centered on -4.6°N, 137.4°E, a region where present-day subsurface ice was predicted to be non-existent by our simulation, even when accounting for surface slopes. MSL Rover Environmental Monitoring Station (REMS) performed high-resolution measurements of temperature and relative humidity during more than one martian year. Hourly REMS products and REMS-inferred quantities with the highest confidence for the first 1000 sols of the mission were provided by G. M. Martinez. The variation of the relative humidity (RH) during this period is shown in Fig. 6.15 (left). The simulations used a value of 280 J m^{-2} K^{-1} $s^{-1/2}$ for the thermal inertia and a heat flow of 0.019 W m^{-2}. The calculated variations of the water vapor flux over one day for different seasons are shown in Fig. 6.15 (right). The amplitude and temporal variation of the flux is similar to the ones for the trace gas observations region at 30°N. As previously, the water flux is more important during warmer seasons.

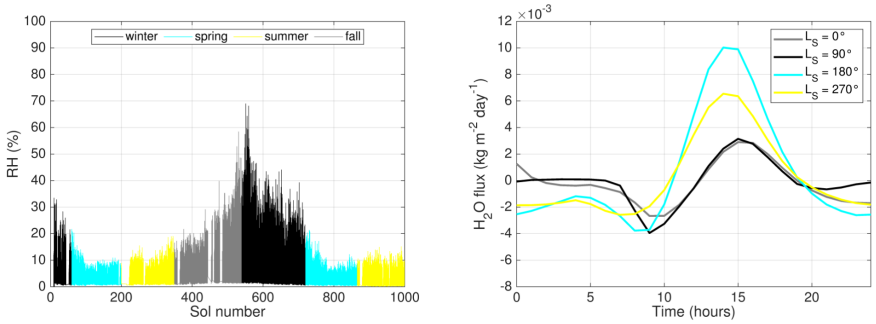

Figure 6.15: Relative humidity measured by REMS during the first 1000 sols of the mission (left) and water vapor flux at MSL landing site over one day for different seasons (right).

Phoenix landing site

Phoenix landed at latitude 68.22°N and identified water ice buried beneath ∼5 cm of dry soil (Smith et al., 2009) with most of the ice being pore ice. The model parameters for the Phoenix landing site are set to correspond to the site-specific properties: the thermal conductivity is 0.085 W m^{-1} K^{-1}, the volumetric heat capacity is 1.05×10^6 J m^{-3} K^{-1}, the porosity is 48% (Zent et al., 2010) and the heat flux is chosen equal to 0.018 W/m^2 (Parro et al., 2017). The variations of the atmo-

spheric water partial pressure during the year are taken from MCD5.2 (Forget et al., 1999). The ice table growth as a function of time for simulations starting with 0% and 10% volume fraction of ice in pores, respectively, is shown in Fig. 6.16. On the left panel, the ice filling grows faster in the top of the ice table while it grows much slower in the lower part. The ice filling reaches zero around 1.3 m deep. On the right panel, the top of the ice table is growing with time and is much closer to the surface, at a depth of 0.23 m. When pore spaces are filled with ice at depth where it is stable, the ice table depth becomes shallower than for a free-ice regolith. To have an ice table depth around 5 cm deep, simulations showed that pores filled with 70% volume fraction of ice were needed. The steady state was not reached in these simulations, hence the ice table could vary further since the ice will change the subsurface thermal inertia.

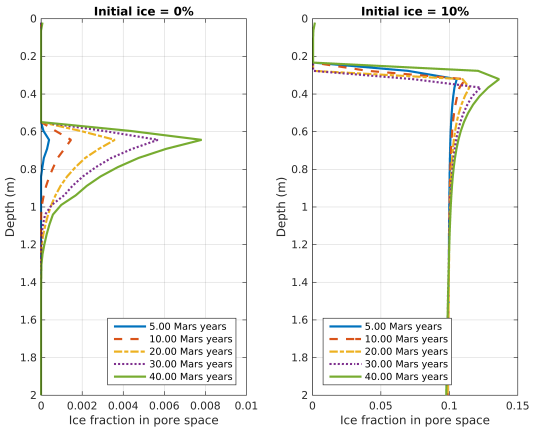

Figure 6.16: Ground ice filling as a function of time at Phoenix landing site after starting with 0% (left) and 10% (right) of initial ice in pores.

We showed that water ice is not stable in martian regions where methane has been reported, except at 30°N where pole-facing slopes greater than 28°allow ice accumulation. At Gale crater, methane diffusion through the regolith should thus not be hindered by water ice. However, clathrate hydrates that would dissociate would be decomposed in methane gas and water ice. This ice deposit, being in an unstable region, would then slowly sublimate with higher rate during warmer periods. Methane release into the martian atmosphere could therefore be controlled by the sublimation rate of this unstable water ice deposit.

6.2 Methane outgassing scenarios

Stevens et al. (2017) showed that diffusive transport (without adsorption) is not able to explain CH_4 short-lived plumes as the one reported by Mumma et al. (2009). However, the shallowest source depth they examined is 200 m, while methane sources considered here are clathrate hydrates located at the top of their stability zone in CH_4 detection regions on Mars, that is to say a few tens of meters. Moreover, diffusive transport could play a role in the variations of the CH_4 background levels and their observed seasonality (Webster et al., 2018). Indeed, Moores et al. (2019) recently showed that methane seasonal cycle at Gale crater is consistent with adsorption and diffusion processes provided that regolith is already impregnated with methane or a continuous microseepage rate (2.8×10^{-16} kg m^{-2} s^{-1} at 30 m deep) is applied.

We investigated the effect of the source depth on CH_4 surface flux with and without the adsorption process. For these simulations, a given total concentration of methane of 2 mg m^{-3} was injected at time $t = 0$ at the base of the model, which is run until all the methane is released into the atmosphere. This CH_4 amount has been chosen by considering that the total mass of methane observed by Mumma et al. (2009) ($\sim 1.86 \times 10^7$ kg) is homogeneously released over the CH_4 plume footprint area (9.7×10^6 km^2). The other model parameters are: latitude = 30°N, $\Phi = 0.45$, $\tau = 1.5$, $\rho c = 1.28 \times 10^6$ J m^{-3} K^{-1}, $I = 250$ J m^{-2} K^{-1} s$^{-1/2}$, A_s = 17,000 m^2 kg^{-1}, q = 16 mW m^{-2}, $L_S = 285°$. Results are shown in Fig. 6.17 and 6.18 for source depths of 50, 100 and 200 m. The peak outgassing flux is shifted in time, occurring later after the initial subsurface release, and has a lower magnitude for a deeper source depth. Including adsorption reduces the methane flux, in this case by a factor of ∼80, and increases the emission time by the same amount. In addition, when adsorption is taken into account, small variations in the CH_4 surface flux following the daily cycle of temperature are observed. Indeed, the transport equation depends on the adsorption and desorption rate constants, and the resulting rate constant can be estimated following the Arrhenius equation. Accordingly, the amount of methane that will be adsorbed or desorbed will change following temperature. When temperature increases, the adsorption process is less important and the surface flux of methane is slightly larger. When temperature decreases, more methane is adsorbed and the surface flux declines in response. Considering this, adsorption process will be therefore more efficient in places with colder mean temperature.

Mumma et al. (2009) calculated that a methane release rate larger or equal to 0.63 kg s^{-1} over the entire plume footprint area is required to

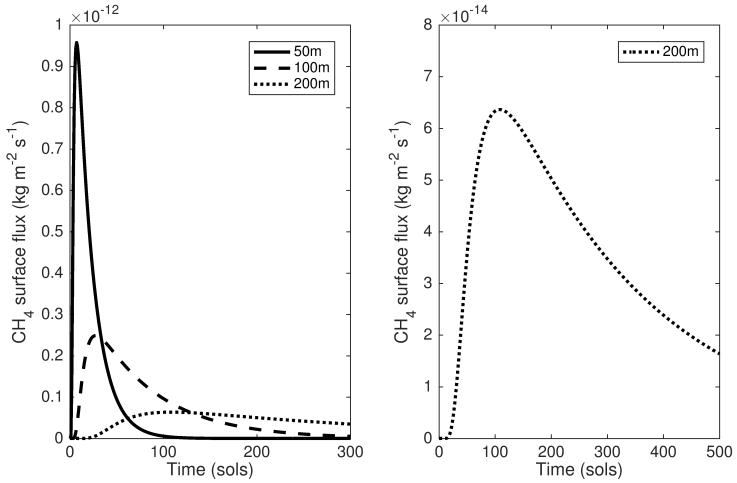

Figure 6.17: Methane outgassing surface flux over time as a function of source depth (adsorption is not taken into account).

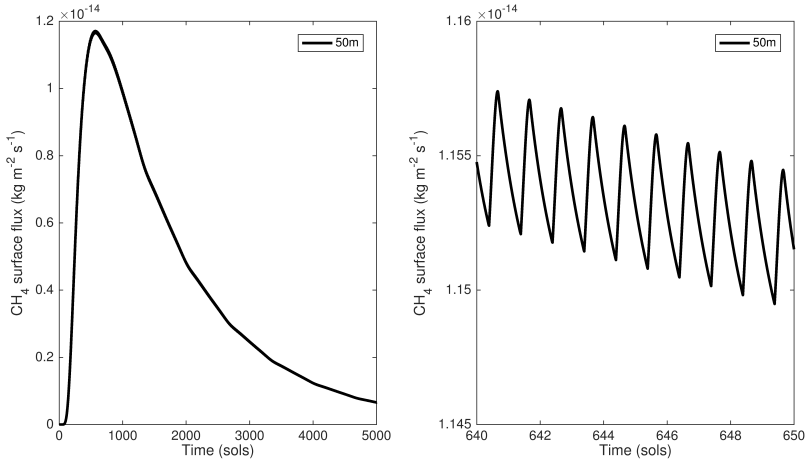

Figure 6.18: Methane outgassing surface flux over time for a source located at 50 m deep (adsorption is taken into account).

match their observations assuming that all the methane is released over a period substantially shorter than a half martian year (< 334 sols). For a homogeneous release throughout the discharge area, the CH_4 flux thus equals 6.5×10^{-14} kg m^{-2} s^{-1}. It can be seen in Fig. 6.17 that this limit value is exceeded with source depths of 50 and 100 m, for which all

the methane is realeased during the time period estimated by Mumma et al. (2009). Regarding the 200 m source depth, methane does not have time to be released in less than half a year and the peak outgassing surface flux barely reaches the limit value of 6.5×10^{-14} kg m^{-2} s^{-1}, which is consistent with results obtained by Stevens et al. (2017). When adsorption is taken into account (Fig. 6.18), the time needed for all the methane to be released is much more longer than 334 sols, even for a shallow source depth of 50 m. Consequently, the CH_4 surface flux is much smaller during the whole release period than the limit value defined above. If we increase the total methane concentration injected in the model, the surface flux is enhanced correspondingly but the release period remains unaffected. So even if we define a total concentration of methane for which the surface flux is above 6.5×10^{-14} kg m^{-2} s^{-1} during the first 334 sols, the flux would continue to increase after that, which is inconsistent with the observations of short-lived methane plumes (Mumma et al., 2009). The source depth should therefore be closer to the surface, which would bring it outside the clathrate stability zone defined in the global maps showed in the previous chapter. We showed that, at 30°N, near-surface ice can be retained on pole-facing slopes ($\geq 28°$). This water ice could prevent further diffusion of methane emitted from deeper source, allowing CH_4 to accumulate in near-surface gas pockets and be discharged during a destabilising event. However, near-surface ice being unstable at very low latitude regions, this scenario is not likely at the equator. Short-lived methane plumes reported by Mumma et al. (2009) can not be explained by diffusive transport, even from shallow sources, when adsorption is taken into account and another process such as advection has to be considered.

Fig. 6.19 shows the CH_4 outgassing surface flux simulated at different latitudes: 30°N, -4.6°N (Curiosity landing site), 68.22°N (Phoenix landing site). Model parameters are the same as previously mentioned for these specific sites and only Knudsen and molecular diffusions are taken into account. It can be seen that in areas where the annual mean temperature is higher, the peak outgassing flux is higher as well. This is explained by the temperature dependence of the diffusion coefficient. This behavior was also found for adsorption due to the variation of the rate constant with temperature. Therefore, for a given amount of methane emitted at a given depth, the surface flux will be higher in equatorial regions where surface and subsurface temperatures are larger and during warmer seasons.

Gainey and Elwood Madden (2012) conducted experiments where the dissociation rates of methane clathrate hydrates have been measured in martian conditions. The highest rate observed is 9.92×10^{-5} mol m^{-2}

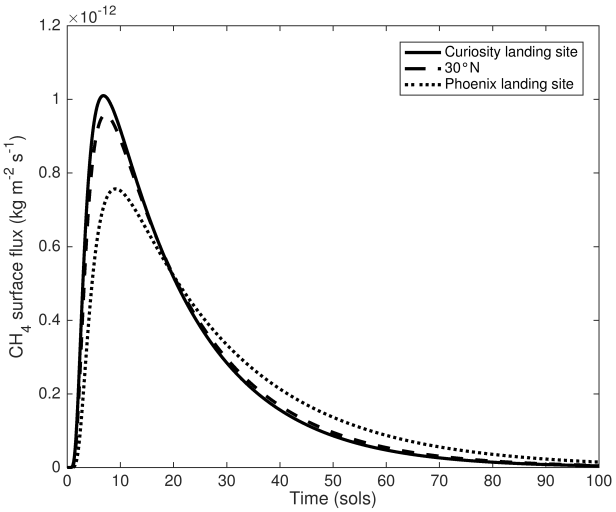

Figure 6.19: Methane outgassing surface flux over time for a source located at 50 m deep at different latitudes (adsorption is not taken into account).

s^{-1}, which corresponds to $\sim 1.6 \times 10^{-6}$ kg m^{-2} s^{-1}. This seepage rate has been applied in our model at 30°N for a source depth of 50 m. The corresponding surface fluxes are represented in Fig. 6.20 with and without the adsorption process. A constant surface flux is reached quite fast (< 100 sols) in the left panel, unlike the case with adsorption where the surface flux still rises after 5000 sols. Higher fluxes are obtained than in the previous simulations, showing well that clathrate hydrates are a possible source for martian methane. However, the considered dissociation rate has been measured for CH_4-rich clathrates. If only a small fraction of methane is trapped in clathrates, this dissociation rate should be lower. In addition, as the clathrate reservoir gradually dissociates, a covering ice layer will start to form and slow down the diffusion of methane and thus the dissociation rate.

When adsorption is taken into account, oscillations in the CH_4 flux following the annual cycle of temperature are superposed to daily variations. We applied our diffusive-adsorptive model at Gale crater with a constant seepage rate of 10^{-15} kg m^{-2} s^{-1}. Results are shown in Fig. 6.21 for source depths of 30 m (methane clathrate stability zone at this depth is found for pole-facing slope with an angle ∼70°) and 50 m. Results at 50°N are also represented for comparison.

When comparing methane fluxes at Gale crater for different subsurface emission depths, it can be seen that the mean surface flux is higher

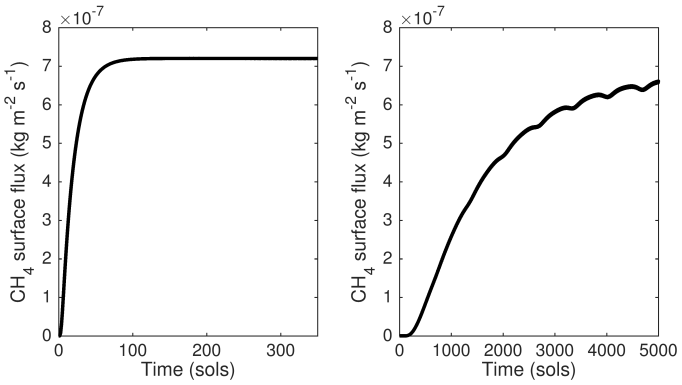

Figure 6.20: Methane outgassing surface flux over time for a source located at 50 m deep and a continuous release rate of 1.6×10^{-6} kg m^{-2} s^{-1}, derived from experimental CH_4 clathrate dissociation rates, without adsorption (left) and with adsorption (right).

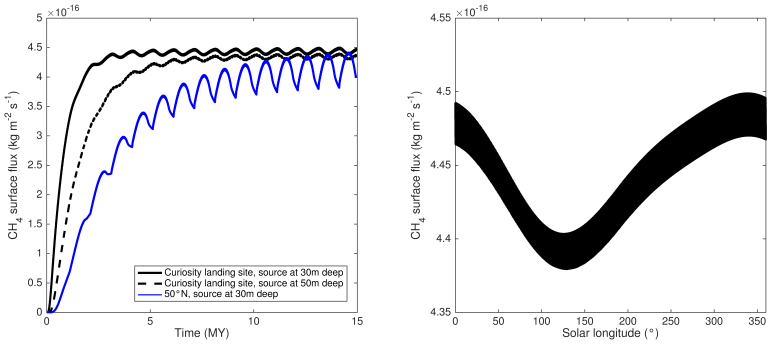

Figure 6.21: Methane outgassing surface flux at Gale crater for a constant seepage rate of 10^{-15} kg m^{-2} s^{-1}.

for a shallower source depth. At 50°N, the mean surface flux is smaller because of the colder surface temperature, as discussed previously. However the amplitude of annual variations is larger because seasonal changes are more pronounced at this higher latitude. The right panel of Fig. 6.21 shows the CH_4 surface flux variations over the martian year. The maximum surface flux occurs at the end of winter in the northern hemisphere. The outgassing peak is thus shifted towards higher L_S compared to Curiosity observations (Webster et al., 2018). In order to have a peak at the end of the northern summer and considering just the subsurface CH_4 diffusion through the soil (without atmospheric transport), methane should

have been emitted at a latitude northward of Gale crater. However, we have assumed thermodynamic equilibrium, that is to say that adsorption is instantaneous at each time step but a time lag should exist to reach equilibrium. The introduction of this time lag in our model would shift the outgassing peak and will be investigated in the future.

6.2.1 Coupling with atmospheric models

In this section, we present the results obtained with two atmospheric models using our CH_4 surface fluxes as inputs.

Region observed by Mumma et al. (2009)

Here, the methane transport in the Mars atmosphere is simulated using time variable CH_4 surface fluxes in a general circulation model, MarsWRF, in order to reproduce the substantial concentrations of methane (up to 50 ppb) observed by Mumma et al. (2009). Previous studies (Lefèvre and Forget, 2009; Mischna et al., 2011; Holmes et al., 2015; Viscardy et al., 2016) have assumed instantaneous or sustained surface emissions with a constant release rate. Here, we use methane emission scenarios consistent with the destabilization of shallow subsurface reservoirs and subsequent methane diffusion through the soil which results in time variable source strength as presented above. All the GCM simulations and their implications have been discussed in details in Temel et al. (2019).

Following the analysis made by Mumma et al. (2009), we use different local source regions near the equator and we determine four surface release scenarios occurring over a period of 15 to 60 sols (see Fig. 6.22) around solar longitude $L_S = 155°$. The strength of the considered methane surface fluxes varies with time, based on our 1-D diffusive transport model, where adsorption was not taken into account. The deeper the methane source is located, the longer it takes for the gas to be transported through the soil into the atmosphere. Considering emission durations of 15, 30, 45 and 60 sols, the sources must be located at 15, 22, 27, 31 m below the surface, respectively. These depths are outside the stability zone of CH_4-rich clathrates but CO_2-rich clathrates trapping small amounts of methane could be located as close to the surface.

In each scenario, the surface emission is initiated at a specific solar longitude such that more than 98% of the total amount of methane is emitted by $L_S = 155°$, when the methane plume observations were made (Mumma et al., 2009). Moreover, the total amount of methane injected into the atmosphere during these periods is adjusted to match the important local maximum of up to 50 ppb observed by Mumma et al. (2009)

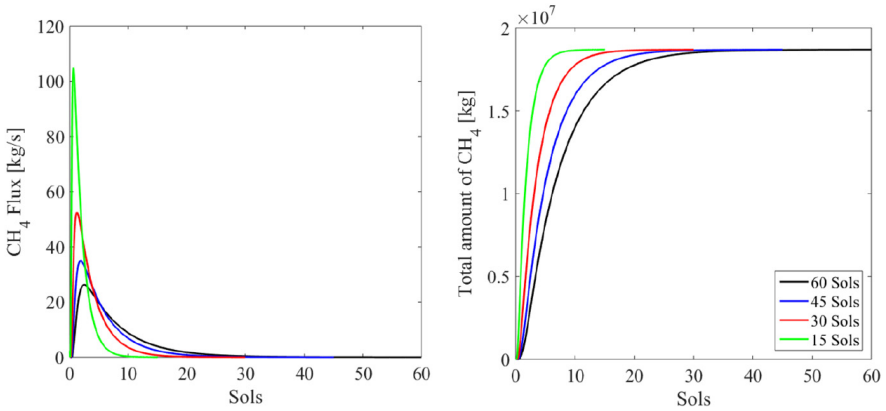

Figure 6.22: Temporal evolution of methane flux and cumulative mass for different release durations. The total amount of methane release is 1.86×10^7 kg corresponding to the local methane plumes observed by Mumma et al. (2009).

by modifying the rates shown in Fig. 6.22. The latitudinal methane concentrations obtained for the different emission scenarios are compared with the observations of Mumma et al. (2009) at $L_S = 155°$. Results obtained by Mischna et al. (2011) with the same GCM but assuming an instantaneous methane emission is included for comparison.

The results, represented in Fig. 6.23, show that methane surface releases determined by our subsurface transport model can reproduce the observations of Mumma et al. (2009) to a better degree of accuracy than previous studies (Mischna et al., 2011). Among the emission locations and durations tested, we found that an emission scenario of 45 sols, during which a total amount of about 90,000 metric tons of methane is released, initiated from (50°E, 10°S), provided the best agreement with the reported observations, in terms of producing the latitudinal mixing of the methane plume with a slightly larger amount of methane than the one estimated by Mumma et al. (2009).

Gale crater

Here, our diffusive gas transport model has been used to estimate an upper limit to the CH_4 steady-state release rate considered in the Mars Regional Atmospheric Modeling System (MRAMS) to simulate the transport and mixing of methane in Gale crater and to test whether the results are consistent with in situ observations made by the Mars Curiosity rover (Pla-García et al., 2019).

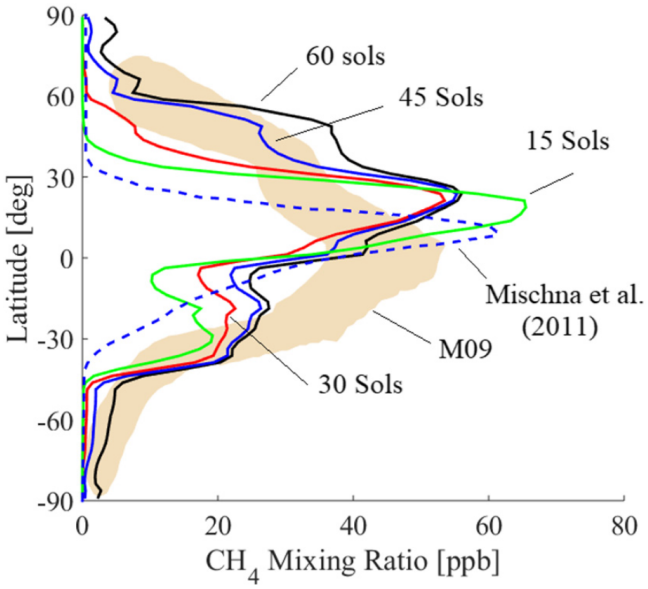

Figure 6.23: Comparison of latitudinal methane concentrations for different emission scenarios from (0°N, 50°E), with observations of Mumma et al. (2009) (M09) at $L_S = 155°$and instantaneous release scenario (Mischna et al., 2011).

As shown in Fig. 5.11, CH_4-rich clathrates in the Gale crater region are stable from a depth of 45 m, which thus defines our source location. Assuming a structure I, clathrates that form from an initial gas phase including 90% CH_4 at 220 K contain ∼75% of methane (see Fig. 5.14). A reservoir of 1 m^3 of those clathrates is therefore composed of ∼80 kg of methane. Assuming a soil porosity of 50% and that 6 to 7% of the pore volume are occupied by clathrates, the total volume of the subsurface reservoir containing 80 kg of methane is 30 m^3. Using the aforementioned parameters in our gas transport model simulating molecular and Knudsen diffusion results in the CH_4 surface flux presented in Fig. 6.24.

A surface flux of up to $\sim 1.8 \times 10^{-6}$ kg m^{-2} s^{-1} is obtained during the first few sols and this value is used as a constant release rate over a period of twelve sols in the MRAMS experiments. The different scenarios consist of a steady-state methane release within an area of 6400 km^2 ∼100 km north-west, north-east, south-west and south-east outside Gale crater and within a region of 150 km^2 inside Gale crater.

In the steady state release experiment inside Gale crater, we found that the methane values at the source location fluctuate from 0.1 to ∼1 ppbv, as shown in Fig. 6.25. This is comparable with the TLS-SAM low

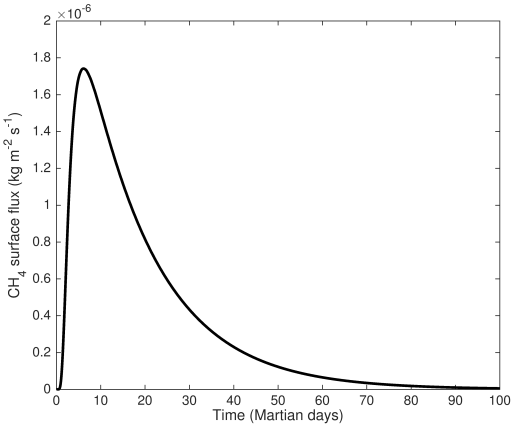

Figure 6.24: Methane outgassing flux used to determine the continuous release rate of methane in MRAMS simulations.

background methane abundances but still ∼1 order of magnitude lower than the methane spikes (∼7 ppb). For the steady-state methane release scenarios outside of Gale crater, our modeled abundances at MSL are ∼100 times lower compared to TLS-SAM spikes during all seasons. Thus, to match the observations, the steady state fluxes would need to be increased by two orders of magnitude. However, a few scenarios that can produce peaks are problematic, because they would result in background methane values above what is observed. In addition, high methane microseepage fluxes on Earth are generally on the order of 10^{-9} to 10^{-6} kg m^{-2} s^{-1}. Increasing our surface flux by two orders of magnitudes would place it well outside the range of terrestrial microseepage observations.

The surface flux above has been determined with "ideal" parameters and already presents an upper value for diffusive methane surface flux from shallow sources. If the adsorption process and the dissociation rate are taken into account or if the source depth is increased and the CH_4 amount in clathrates and the porosity are decreased, the resulting surface flux will be reduced correspondingly. In view of the results given by the MRAMS experiments, clathrate dissociation and subsequent methane diffusion through the regolith cannot be responsible for CH_4 spikes observed by MSL (Webster et al., 2015, 2018). Other potential subsurface methane sources that would imply gas diffusion through the regolith, and thus are subject to the same physics, are also unlikely. In order to explain these high and sporadic CH_4 levels, other gas transport processes such as advection should be investigated. Nevertheless, diffusive

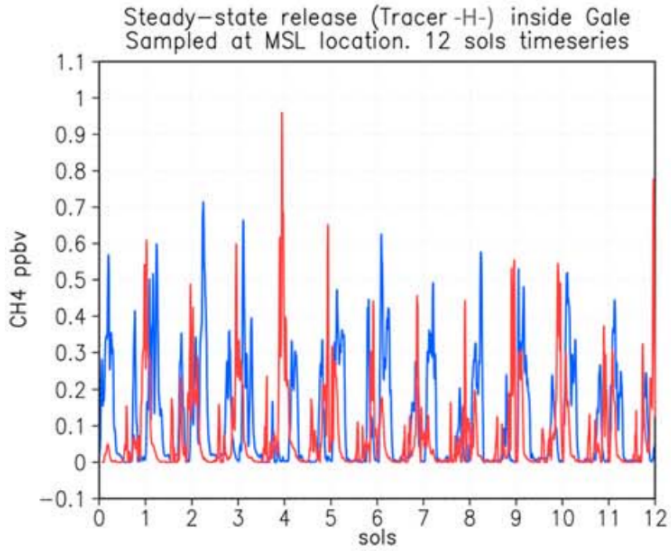

Figure 6.25: Twelve-sols time series of MRAMS methane abundances sampled at the MSL location for a steady state release location inside Gale crater. Blue is L_S 90° and red is L_S 270°. The abundance of tracers is shown shortly after the flux is turned on.

transport is consistent with low background levels of methane at Gale crater.

6.3 Summary

In the simulations for present-day Mars, near-surface ice is not stable at MSL landing site. At Gale crater, methane diffusion from shallow subsurface sources should thus not be hindered by water ice. At 30°N, pole-facing slopes greater than 28°allow ice accumulation, which could slow down diffusion of methane emitted from deeper source. At Phoenix landing site, a permanent ice table close to the surface can be observed but its location depends on the initial ice content of the subsurface. When pore spaces are filled with ice at depth where it is stable, the ice table depth becomes shallower. To match the observed water ice depth of ∼5 cm (Smith et al., 2009), simulations showed that pores must be filled with 70% volume fraction of ice. These results are consistent with the Shallow Radar (SHARAD) observations on the Mars Reconnaissance Orbiter which has been searching for subsurface interfaces at the landing sites and found only clear evidence of subsurface radar returns at the

Phoenix site (Putzig et al., 2014). The obtained results are also consistent with the observations of Gamma Ray Spectrometer onboard Mars Odyssey (Feldman et al., 2004) as well as other models (Schorghofer and Aharonson, 2005 ; Mellon et al., 2004).

When adsorption is taken into account in the simulations, short-lived methane plumes reported by Mumma et al. (2009) can not be explained by diffusive transport, even from shallow sources, and another process such as advection has to be considered. However, methane surface release patterns determined by a diffusive transport model can reproduce the observations of Mumma et al. (2009) to a better degree of accuracy than with an instantaneous surface release. Regarding Gale crater, methane diffusion from shallow sources is consistent with low background levels of methane and adsorption is causing seasonal variations in the surface flux. However, CH_4 spikes observed by Curiosity are hardly explained by diffusive gas transport and would require a surface flux of the order of 10^{-4} kg m^{-2} s^{-1}.

Finally, for a given source depth and a given methane concentration, surface flux is higher in warmer regions due to the temperature dependence of the diffusion coefficient and the adsorption rate constant. Furthermore, near-surface ice being unstable and not slowing or preventing methane diffusion in low latitude areas, diffuse microseepage of methane would be more likely to be detected in equatorial regions of Mars.

Chapter 7

Conclusions and perspectives

For years scientists have been studying the origin and fate of methane on Solar System bodies in order to understand their formation and evolution as well as the habitability of terrestrial worlds. On Earth, methane is mainly produced by biological activity, while its presence on the giant planets - Jupiter, Saturn, Uranus and Neptune - results from chemical processes in the primordial solar nebula. Methane also strangely persists in Titan's atmosphere, intriguing scientists about the life-hosting potential of this moon. In addition, Titan is sometimes believed to be very similar to early Earth. Therefore, Saturn's largest moon remains a main target for future space missions as the detailed characterization of its atmospheric chemistry may shed light on prebiotic processes that could have occurred on our planet.

Among the planets, Mars is undoubtedly the right place for the search of extraterrestrial life, either extinct or extant, especially since small amounts of methane have been detected in its atmosphere. Methane's lifetime on Mars, predicted by standard photochemical models, is relatively long enough to enable a quite uniform mixing of the gas by winds. However, both remote-sensing and in-situ observations have evidenced substantial variations of the CH_4 mixing ratio suggesting that methane release in the planet's atmosphere is a sporadic and/or localized process. The martian CH_4 source is still unknown and discovering it would constitute a scientific breakthrough. Existing hypotheses for methane formation mechanisms on Mars include microbial activity and gas-water-rock chemistry. Either origin would be exciting: one would mean the discovery of life elsewhere than on Earth, while the other assumption would imply the existence of subterranean water environments with chemical sources of energy.

Once generated at depth, martian methane could be stored in subsurface clathrate hydrate reservoirs. Some may be preserved over time, while others would decompose and gradually or abruptly release methane depending on the destabilising event. Clathrate deposits could be very localized and occupy only a small part of the martian cryosphere, which would be consistent with the observed spatial heterogeneity of methane. In this thesis work, the methane clathrate stability zone and its variations in the martian crust have been investigated in order to establish where methane clathrates could occur while evaluating them as a potential source for martian methane. For this reason, we have also developed a diffusive-adsorptive model of gas transport, for which the CH_4 source depths are constrained by the estimated stability zone of clathrate hydrates on Mars.

Our results showed that the stability conditions of CH_4-rich clathrates (formed from a gas phase with 90% CH_4) are met in the shallow martian subsurface. These crystalline compounds can be stable very near the surface at high latitudes, and can be as close as 20 m to the surface in the tropics. In the equatorial region where Mumma et al. (2009) reported methane plume detection during the northern summer 2003, the clathrate stability zone has been found to be the deepest (∼68 m). By taking into account only molecular and Knudsen diffusion in our gas transport model, methane that would be emitted from this depth would give a surface flux duration consistent with observations (Mumma et al., 2009). Using this surface flux pattern as an input in a general circulation model allows us to obtain a better match with observations for the latitudinal distribution of methane than the one simulated with an instantaneous surface release (Temel et al., 2019). Among the different tested scenarios, the best agreement is found for a surface emission of 45 sols during which a total amount of about 90,000 metric tons of methane are released over an area of 22,000 km^2 centered on (0°N, 50°E). Longer surface emissions would also be consistent but would require to increase the total amount of emitted methane in order to reproduce the equatorial CH_4 peak of 50 ppbv (Mumma et al., 2009). In our subsurface model, a 45-sol emission duration corresponds to a source depth of ∼27 m, which places it outside the stability field of CH_4-rich clathrates showed in our global map, but remains consistent with CO_2-rich clathrates (including small CH_4 fraction) stability zone.

Including adsorption in the model considerably slows down the transport process and increases the surface release duration making the simulations unable to produce short-lived methane plumes, even from shallow depth. As a result, diffusive transport is likely not the dominant process that generated the CH_4 plumes observed by Mumma et al. (2009)

and advection will thus be considered in future studies. Taking into account this last process should allow the methane source corresponding to the best GCM scenario, defined above, to be deeper than the 27 m estimated with the diffusive model. Moreover, we showed that with the growth of the pressure formation, and thus the increase of the depth formation, methane content in binary CO_2-CH_4 clathrate increases. Therefore, CH_4-rich clathrates that would presently form from a source in the martian crust, would be more likely to occur at a large depth. Short surface releases implying methane liberated from those deep clathrates cannot be explained by our diffusive transport of methane, even if adsorption is neglected, which is consistent with results obtained by Stevens et al. (2017).

Regarding Gale crater, methane diffusion from shallow sources is consistent with low background levels of methane but CH_4 spikes observed by Curiosity require a surface flux larger by two orders of magnitude than our upper estimated flux (Pla-García et al., 2019). Although adsorption is causing seasonal variations in the surface flux, a release area northward of the crater is needed in order to have a peak in the surface flux at the end of the northern summer, which is in conflict with Moores et al. (2019) who reproduced properly the seasonality of the background CH_4 levels with a diffusive-adsorptive model applied in Gale. This difference between the models could be explained by the fact that we did not consider the time lag needed to reach thermodynamic equilibrium in adsorption modelling. This time lag (Equation 4.53) will be introduced in the future developments of our gas transport model.

We showed that the stability field of methane clathrate in the subsurface is shifted upwards with tilted surfaces oriented towards the pole as these slopes experience colder surface temperature. Moreover, at Gale crater latitude, equator-facing slopes larger than 30° can also bring the clathrate stability zone closer to the surface. Methane released by clathrates dissociating below crater walls could experience a shorter diffusive path length in the horizontal direction. Upgrading the gas transport model from 1D to 2D would therefore be useful, in particular with crater-related topography or for specific sites with a particular geometry.

It is important to note that the dissociation pressures and fraction occupancies of clathrate hydrates predicted with the model of van der Waals and Platteeuw (1959) depend on parameters fitted on experimental equilibrium data. The key step in this model is the description of the guest-clathrate interaction potential, which is often based on the Kihara potential with adjustable parameters. In this work, we used Kihara parameters optimized by Herri and Chassefière (2012) for temperatures

relevant to Mars. However, the use of these parameters outside a range of temperature and pressure for which they have been determined may lead to erroneous fraction occupancies. In future studies on methane trapping in clathrate hydrates formed in extreme environment conditions, comparison with experimental data on pure and multiple guest clathrate hydrates is therefore necessary to determine the best set of adjustable parameters.

As shown in our sensitivity study, the clathrate stability zone is very responsive to the composition of the subsurface material. In our simulations to establish global maps of the top of the stability zone, we mainly considered a basaltic composition, which is fairly representative of the martian crust. However, local variations in the soil material could strongly affect the methane clathrate distribution displayed on our global maps and even prevent clathrate formation at low latitude if the thermal conductivity of the material is quite small. In order to further constrain the clathrate stability field on Mars, geological observations coupled to a comprehensive sensitivity analysis with respect to soil parameters is thus required. In addition, our global maps do not show metastable zones. Indeed, some clathrate reservoirs could be localized outside their present stability field in areas associated to ancient stability zones. These reservoirs could represent essential sources in the study of methane outgassing scenarios since, being unstable, they would gradually release methane from depths possibly very close to the surface. Experimental work on kinetic of clathrate formation and dissociation should be used together with a subsurface thermal model taking into account obliquity variations to evaluate the potential extent and locations of these metastable clathrate reservoirs. Finally, in order to give a better accurate estimation of the methane clathrate occurences on Mars, a physical model such as the one presented in this work need to be coupled with topography/geological analysis to determine possible regions within the clathrate stability zone where sufficient CH_4 supplies could exist.

Regarding our gas transport model, competition for adsorption sites was not taken into account. However, if several species diffuse with methane, some would be adsorbed with more or less efficiency than methane, resulting in less adsorbed CH_4 molecules and a higher CH_4 surface flux than when methane diffuses alone. Moreover, the adsorption parameters such as the specific surface area and the adsorption rate constant of the regolith have to be determined using experiments on analog materials. The range of values taken by these parameters over all material types can be important. Therefore, as previously, methane adsorption studies would be improved by the coupling with detailed geological observations and analysis of Mars.

Although Trace Gas Orbiter is currently not detecting any martian methane, this does not prevent potential future observations, especially if the methane is outgassed only episodically. From the point of view of diffusion, a higher surface flux of methane should be observed in warmer regions and periods. Also, gas accumulation being a process spread over time, martian regions that already have been recognized as CH_4 emission areas in the past would be expected to repeat that episodic releases through time (Etiope and Oehler, 2019). The region observed by Mumma et al. (2009) or Gale crater seem therefore to be good locations for follow-up methane studies. In addition, it is important to note that methane outgassing scenarios are strongly dependent on the subsurface environment. The Mars InSight Lander should provide new data to constrain seismicity and tectonism on Mars and thus new clathrate destabilization scenarios linked to pressure changes.

In addition to determining the methane source(s) on Mars, identifying the CH_4 destruction mechanism(s) is another martian challenge to be solved. The observed spatial and temporal heterogeneity of CH_4 in the martian atmosphere considerably questions our current understanding of atmospheric chemistry and physics on Mars. Indeed, the reported variations in methane concentration imply strong destruction mechanisms acting about 600 times faster than the only methane sink currently accepted on Mars (Lefèvre and Forget, 2009). The latest published observations (Korablev et al., 2019; Webster et al., 2018) also seem to indicate the presence of exotic processes quickly removing methane from the atmosphere. Indeed, this hypothesis is required for both observations, the detection by MSL and the non-detection by TGO, to remain simultaneously valid. Ongoing measurements by Trace Gas Orbiter should provide new valuable constraints on the frequency and magnitude of methane releases on a global scale. Identify the CH_4 sink remains a major challenge in the study of martian methane mystery and should be treated as a priority.

In 2020, one step further in the astrobiological investigation of the Red Planet will be achieved with the launch of the Mars 2020 rover and the ExoMars 2020 missions, that will set the stage for Mars sample return missions. Both rovers will carry a comprehensive suite of instruments dedicated to geology and exobiology studies and will search for evidences of past or present microbial life. While the first mission plans to collect core samples and set them aside in a cache on the surface in order to return them later on Earth, the second has been designed to drill down to a depth of 2 m where potential signs of life could be preserved. To discriminate between abiotic and biotic sources of methane on Mars,

a series of geochemical analyses including measurements of CH_4 isotopes has to be performed preferably below the ground. However, CH_4 isotopic ratio observed just below the surface could be misleading and should be carefully interpreted. The original isotopic composition can considerably change during gas migration in the subsurface and observations should therefore be examined together with the modelling of diffusive transport or other processes on the isotopic ratio. The gas transport model developed in this work could then be used for this purpose. In addition, comparing the future measurements with the effect of transport on isotopic fractionation could further constrain the CH_4 source depth.

Regarding the development of a future mission dedicated to the detection of clathrate hydrates, if those compounds are present on the surface of the observed moon or planet, spectroscopic methods can be used to identify them. On the other hand, it gets more complicated when clathrates are stable below the surface, as is the case on Mars. On Earth, evidence of clathrate hydrate in the seafloor and in the permafrost is collected via deep sea drilling or sediment coring but their presence is more often deduced indirectly from geophysical and geochemical measurements (Buffett, 2000). In marine sediments, clathrate detection techniques make use of velocity contrasts beneath the ocean floor indicating a change of material density. The bottom-simulating reflector (BSR), a seismic reflection that parallels the seafloor reflection, marks the limit between a high-velocity sediment layer denoting the presence of clathrates in the pore volume or as massive deposits and a low-velocity sediment layer implying the presence of gas bubbles. The BSR is therefore taken as the predicted base of the clathrate stability zone. Unfortunately, this technique as well as radar observations are not applicable in permafrost to distinguish between water ice and clathrate as those compounds present similar seismic and electromagnetic properties. In-situ clathrate detection techniques on Mars should be applied at high latitude, methane clathrate stability conditions being met very close to the surface in these regions, and thermal conductivity measurements could be performed to differentiate clathrate from water ice. On the other hand, detection experiments could involve a forced dissociation, as proposed by Duxbury et al. (2001) for the moon, followed by an analysis of the released gases.

For the detection of clathrates located at the base of their stability zone that is to say below the cryosphere, Duxbury et al. (2004) have proposed a method combining thermodynamic modelling and radar data to limit the search areas for future drilling. In this approach, the thermodynamic model simulates the effect of the latent heat released or absorbed during clathrate formation and dissociation, respectively, on the internal

heat flow above the clathrate deposit. The resulting increase or decrease of the temperature translates into a curvature of the 0°C isotherm, causing a cap-shaped curve (in the case of clathrate formation) or a U-shaped curve (in the case of clathrate dissociation). This 0°C isotherm showing the permafrost/ground water interface can be located using electromagnetic sounding methods. And if a curvature is detected, it can be a sign of a potential underlying clathrate reservoir. The thermal model developed in this work should be upgraded to 2D to take into account this phenomenon.

Clathrate hydrates, in addition to trap gases potentially produced during a past period of the Solar System, can also play a role in the evolution of planetary interior and habitability. Indeed, Kamata et al. (2019) have recently shown that the presence of a thin layer of clathrate hydrates at the base of the icy shell of Pluto can explain the existence of a subsurface ocean. The thermal conductivity of clathrate hydrates being unusually low, about a fifth of that of water ice, they act as a thermal insulator. The presence of clathrate layers could thus be significant to maintain a subsurface ocean, especially in minimally heated terrestrial worlds. It would be interesting for future studies on the evolution of ocean-bearing planets/moons to consider clathrates as a material composing the icy crust.

Finally, methane being known to be an effective greenhouse gas and clathrate hydrates being widely distributed along continental margins and in permafrost, questions about their role in climate change have been raised. Significant global dissociation of methane clathrates has already occured at the end of the Paleocene Epoch, 56 million years ago, causing a 4-8°C temperature rise over a brief geologic time interval called the Late Paleocene Thermal Maximum (Dickens et al., 1995). Massive release scenarios take into account the fact that clathrates are stable very close to the surface. Increases in temperature or decreases in pressure due to sea level changes contribute to decompose methane clathrates. In order to understand if clathrate dissociation in response to climate change is a global process, specific studies on kinetic dissociation of clathrates, methane migration into the atmosphere and the reaction of clathrates to environmental changes are needed.

Appendix A

Calculation of the fugacity

In this study, the fugacity f of clathrate former(s) in the gas phase is computed using the Peng-Robinson equation of state (PR EoS) (Peng and Robinson, 1976):

$$P = \frac{RT}{v-b} - \frac{a(T)}{v(v+b)+b(v-b)} \tag{A.1}$$

where P is the pressure, R is the gas constant, T is the thermodynamic temperature, v is the molar volume and a and b are the parameters of the PR EoS. The Equation A.1 can be rewritten in terms of the compressibility factor $Z \equiv (Pv/RT)$ as:

$$Z^3 - (1-B)Z^2 + (A - 3B^2 - 2B)Z - (AB - B^2 - B^3) = 0 \tag{A.2}$$

with

$$A = \frac{aP}{R^2T^2} \tag{A.3a}$$

$$B = \frac{bP}{RT} \tag{A.3b}$$

$$a(T) = 0.45724\,\frac{R^2T_c^2}{P_c}\,\alpha(T_r,\omega) \tag{A.3c}$$

$$\alpha(T_r,\omega) = \left(1 + \kappa\,(1 - T_r^{1/2})\right)^2 \tag{A.3d}$$

$$\kappa = 0.37464 + 1.54226\,\omega - 0.26992\,\omega^2 \tag{A.3e}$$

$$b = 0.0778\,\frac{RT_c}{P_c} \tag{A.3f}$$

where the variables T_c and P_c represent the critical temperature and critical pressure, respectively, and $\alpha(T_r,\omega)$ is a dimensionless function of

reduced temperature $T_r \equiv (T/T_c)$ and acentric factor ω. Note that at the critical temperature, this function is equal to unity. Critical constants and acentric factors for different species are given in Table A.1.

Table A.1: Critical temperature, pressure and acentric factors for the various species considered in this study.

Species	T_c (K)	P_c (MPa)	ω
CH_4	191	4.6	0.010
CO_2	304	7.38	0.225
N_2	126	3.39	0.038
Ar	151	4.86	0.0
H_2	33	1.29	-0.22

When the Peng-Robinson equation of state is used for a mixture, some mixing rules are required to describe the composition dependence of parameters a and b. In this work, the van der Waals mixing rules are used:

$$a_m = \sum_i \sum_j y_i y_j \sqrt{a_i a_j}(1 - k_{ij}) \quad (k_{ij} = k_{ji},\ k_{ii} = 0) \tag{A.4a}$$

$$b_m = \sum_i y_i b_i \tag{A.4b}$$

where a_i and b_i are pure component properties, y_i is the molar fraction of component i and k_{ij} is a binary interaction coefficient, a correction factor that can be obtained by fitting to experimental phase equilibrium data. We used values for k_{ij} found in the litterature ($k_{CH_4-CO_2}$ = 0.0919, $k_{N_2-CO_2}$ = -0.017, $k_{CH_4-N_2}$ = 0.0311, k_{CO_2-Ar} = 0.163; Fateen et al. (2013); Li and Yan (2009)) and, when those were not available, we estimated the binary interaction coefficient via the correlation given by Gao et al. (1992):

$$1 - k_{ij} = \left(\frac{2\sqrt{T_{c_i} T_{c_j}}}{T_{c_i} + T_{c_j}} \right)^{Z_{c_{ij}}} \tag{A.5a}$$

$$Z_{c_{ij}} = \frac{Z_{c_i} + Z_{c_j}}{2} \tag{A.5b}$$

where Z_{c_i} is the critical compressibility factor of component i.

If the molar fractions of clathrate formers in the gas phase are known, the volume of that phase may be predicted at a given temperature and

pressure. Since the Equation A.2 is cubic, three volume roots are obtained for each set of parameters and the largest one corresponds to the compressibility factor of the vapor. Alternatively, if the liquid phase mole fractions are used in the equation of state, the smallest positive root is used for the liquid. The Newton-Raphson method is a useful numerical tool for solving the Equation A.2 ($g(Z) = 0$) provided that a first guess close to the actual root is assumed. This iterative procedure requires the evaluation of both the function $g(Z)$, and the derivative $g'(Z)$, at arbitrary points Z and provides a new estimate of the root Z_{new} based on the previous one Z_{old}:

$$Z_{\text{new}} = Z_{\text{old}} - \frac{g(Z_{\text{old}})}{g'(Z_{\text{old}})} \tag{A.6}$$

Generally, the starting guess for Z is taken equals to 1 for the vapor phase, while $Z = \frac{bP}{RT}$ is the first estimate of the liquid root. On the other hand, the PR EoS can be solved analytically with the scheme below (Cardano's method). The Equation A.2 is first rewritten as:

$$Z^3 + a_1 Z^2 + a_2 Z + a_3 = 0 \tag{A.7}$$

where

$$a_1 = -(1 - B) \tag{A.8a}$$
$$a_2 = A - 3B^2 - 2B \tag{A.8b}$$
$$a_3 = -(AB - B^2 - B^3) \tag{A.8c}$$

Then, we compute:

$$Q = \frac{3a_2 - a_1^2}{9}, \quad R = \frac{9a_1a_2 - 27a_3 - 2a_1^3}{54} \tag{A.9}$$

Let $D = Q^3 + R^2$ be the discriminant, we have three different cases:

- If $D < 0$: all roots are real and unequal.

In this case, we calculate $\cos(\theta) = \frac{R}{\sqrt{-Q^3}}$ and the three roots are expresssed as:

$$z_1 = 2\sqrt{-Q}\cos\left(\frac{\theta}{3}\right) - \frac{a_1}{3} \tag{A.10a}$$

$$z_2 = 2\sqrt{-Q}\cos\left(\frac{\theta}{3} + \frac{2\pi}{3}\right) - \frac{a_1}{3} \tag{A.10b}$$

$$z_3 = 2\sqrt{-Q}\cos\left(\frac{\theta}{3} + \frac{4\pi}{3}\right) - \frac{a_1}{3} \tag{A.10c}$$

- If $D = 0$: all roots are real and at least two are equal.
- If $D > 0$: one root is real and two are complex conjugates.

In this case, the real root is given by:

$$z_1 = S + T - \frac{a_1}{3} \tag{A.11}$$

where

$$S = \sqrt[3]{R + \sqrt{D}} \tag{A.12a}$$

$$T = \sqrt[3]{R - \sqrt{D}} \tag{A.12b}$$

Finally, the fugacity f of clathrate former(s) in the phase of interest is obtained with the following equations:

$$\ln\left(\frac{f}{P}\right) = Z - 1 - \ln(Z - B) - \frac{A}{2\sqrt{2}B}\ln\left(\frac{Z + (1+\sqrt{2})B}{Z + (1-\sqrt{2})B}\right) \tag{A.13}$$

$$\ln\left(\frac{f_i}{y_i P}\right) = \frac{b_i}{b_m}(Z-1) - \ln(Z-B) - \frac{A}{2\sqrt{2}B}\left(\frac{2\sum_j y_j a_{ji}}{a_m} - \frac{b_i}{b_m}\right) \ln\left(\frac{Z + (1+\sqrt{2})B}{Z + (1-\sqrt{2})B}\right) \tag{A.14}$$

where the first equation applies to a pure component, while the second is used for a mixture. Examples of fugacity coefficients obtained for a pure component ($\Phi = \frac{f}{P}$) and a gas mixture ($\Phi_i = \frac{f_i}{y_i P}$) are shown in Fig. A.1 and Fig. A.2 respectively.

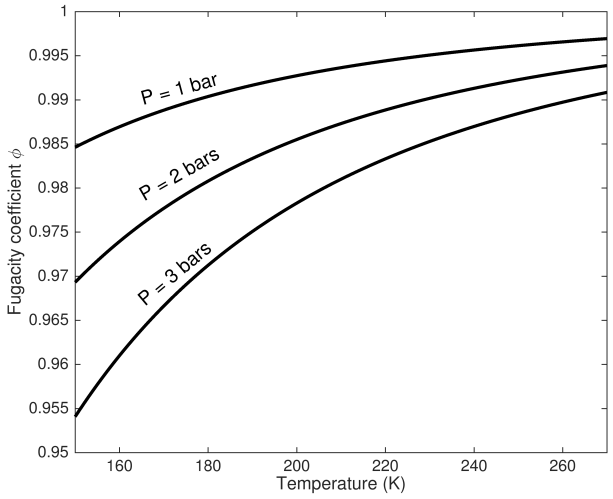

Figure A.1: Calculated fugacity coefficient for methane as a function of temperature and pressure.

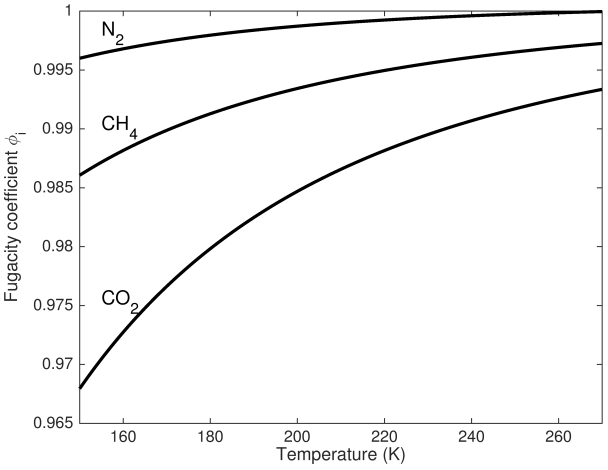

Figure A.2: Calculated fugacity coefficients at 1 bar for a gas mixture including 50% of CH_4, 40% of CO_2 and 10% of N_2 as a function of temperature.

Appendix B

Crank-Nicolson scheme

To determine the evolution of subsurface temperature with time, the Crank-Nicolson method, obtained by computing the average of the explicit and implicit forward time centered space (FTCS) schemes, is used to solve the heat equation:

$$\rho c \frac{\partial T}{\partial t} = \frac{\partial}{\partial z}\left(k \frac{\partial T}{\partial z}\right) + \rho H, \quad k \frac{\partial T}{\partial z} = F \tag{B.1}$$

where ρ is density, c is specific heat capacity, T is temperature, z is vertical coordinate, t is time, k is thermal conductivity, H is radiogenic heat production and F is heat flow. The first term of the second member of the Equation B.1 can be differentiated on an irregular grid as:

$$\frac{\partial}{\partial z} F_j = \frac{F_{j+1/2} - F_{j-1/2}}{(z_{j+1} - z_{j-1})/2} = 2 \frac{k_{j+1/2} \frac{T_{j+1} - T_j}{z_{j+1} - z_j} - k_{j-1/2} \frac{T_j - T_{j-1}}{z_j - z_{j-1}}}{z_{j+1} - z_{j-1}} \tag{B.2}$$

We then obtain:

$$\begin{aligned} (\rho c)_j \frac{\partial T_j}{\partial t} =& \frac{2k_{j+1/2}}{(z_{j+1} - z_j)(z_{j+1} - z_{j-1})} T_{j+1} \\ & - \frac{2}{z_{j+1} - z_{j-1}} \left(\frac{k_{j+1/2}}{z_{j+1} - z_j} + \frac{k_{j-1/2}}{z_j - z_{j-1}} \right) T_j \\ & + \frac{2k_{j-1/2}}{(z_j - z_{j-1})(z_{j+1} - z_{j-1})} T_{j-1} + \rho_j H \end{aligned} \tag{B.3}$$

We introduce:

$$\alpha_j = \frac{\Delta t}{(\rho c)_j} \frac{k_{j+1/2}}{(z_{j+1} - z_j)(z_{j+1} - z_{j-1})} \tag{B.4a}$$

$$\gamma_j = \frac{\Delta t}{(\rho c)_j} \frac{k_{j-1/2}}{(z_j - z_{j-1})(z_{j+1} - z_{j-1})} \tag{B.4b}$$

Equation B.3 thus becomes:

$$\Delta t \frac{\partial T_j}{\partial t} = 2\alpha_j T_{j+1} - 2(\alpha_j + \gamma_j)T_j + 2\gamma_j T_{j-1} + \frac{\Delta t H}{c_j} \tag{B.5}$$

Applying Crank-Nicolson, we get:

$$\begin{aligned} T_j^{n+1} - T_j^n =& \alpha_j T_{j+1}^{n+1} - (\alpha_j + \gamma_j)T_j^{n+1} + \gamma_j T_{j-1}^{n+1} \\ &+ \alpha_j T_{j+1}^n - (\alpha_j + \gamma_j)T_j^n + \gamma_j T_{j-1}^n + \frac{\Delta t H}{c_j} \end{aligned} \tag{B.6}$$

Rearranging the equation to isolate the different time-variables gives:

$$\begin{aligned} &- \alpha_j T_{j+1}^{n+1} + (1 + \alpha_j + \gamma_j)T_j^{n+1} - \gamma_j T_{j-1}^{n+1} \\ &= \alpha_j T_{j+1}^n + (1 - \alpha_j - \gamma_j)T_j^n + \gamma_j T_{j-1}^n + \frac{\Delta t H}{c_j} \end{aligned} \tag{B.7}$$

This system of linear equations is tridiagonal and can easily be solved at each time step by *LU* decomposition (see *tridag* routine from *Numerical Recipes* (Press et al., 1997), for instance). The thermal conductivity k is defined on half-points and $(\rho c)_j = \frac{(\rho c)_{j-1/2} + (\rho c)_{j+1/2}}{2}$ so that these parameters do not have to be determined at the interface of two layers with different thermal properties. The upper and lower boundary conditions are given by the surface temperature and the heat flow, respectively.

Lower boundary condition

If N is the total number of subsurface layers and assuming $z_{N+1} - z_N = z_N - z_{N-1}$, we can write:

$$k_{N+1/2}(T_{N+1} - T_N) = (z_{N+1} - z_N)F \tag{B.8}$$

and thus

$$T_{N+1} = T_N + \frac{(z_{N+1} - z_N)F}{k_{N+1/2}} \tag{B.9}$$

Using the above relation and the expression of α_N in Equation B.7 for $j = N$ leads to:

$$\begin{aligned}(1+\gamma_N)T_N^{n+1} - \gamma_N T_{N-1}^{n+1} =& (1-\gamma_N)T_N^n + \gamma_N T_{N-1}^n \\ &+ \frac{\Delta t F}{(\rho c)_N (z_N - z_{N-1})} + \frac{\Delta t H}{c_N}\end{aligned} \tag{B.10}$$

Bibliography

Aharonson, O., Schorghofer, N., 2006. Subsurface ice on Mars with rough topography. Journal of Geophysical Research: Planets 111 (E11).

Allison, M., McEwen, M., 2000. A post-Pathfinder evaluation of areocentric solar coordinates with improved timing recipes for Mars seasonal/diurnal climate studies. Planetary and Space Science 48 (2-3), 215–235.

Amali, S., Rolston, D. E., 1993. Theoretical investigation of multicomponent volatile organic vapor diffusion: Steady-state fluxes. Journal of environmental quality 22 (4), 825–831.

Anderson, B. J., Bazant, M. Z., Tester, J. W., Trout, B. L., 2005. Application of the cell potential method to predict phase equilibria of multicomponent gas hydrate systems. The Journal of Physical Chemistry B 109 (16), 8153–8163.

Anderson, G. K., 2004. Enthalpy of dissociation and hydration number of methane hydrate from the Clapeyron equation. The Journal of Chemical Thermodynamics 36 (12), 1119–1127.

Aoki, S., Richter, M. J., DeWitt, C., Boogert, A., Encrenaz, T., Sagawa, H., Nakagawa, H., Vandaele, A. C., Giuranna, M., Greathouse, T. K., et al., 2018. Stringent upper limit of CH_4 on Mars based on SOFIA/EXES observations. Astronomy & Astrophysics 610, A78.

Arnošt, D., Schneider, P., 1995. Dynamic transport of multicomponent mixtures of gases in porous solids. The Chemical Engineering Journal and the Biochemical Engineering Journal 57 (2), 91–99.

Atreya, S. K., Gu, Z. G., 1995. Photochemistry and stability of the atmosphere of Mars. Advances in Space Research 16 (6), 57–68.

Atreya, S. K., Mahaffy, P. R., Wong, A.-S., 2007. Methane and related trace species on Mars: Origin, loss, implications for life, and habitability. Planetary and Space Science 55 (3), 358–369.

Bar-Nun, A., Dimitrov, V., 2006. Methane on Mars: A product of H_2O photolysis in the presence of CO. Icarus 181 (1), 320–322.

Bar-Nun, A., Dimitrov, V., 2007. "Methane on Mars: A product of H_2O photolysis in the presence of CO": Response to VA Krasnopolsky. Icarus 188 (2), 543–545.

Beck, P., Pommerol, A., Schmitt, B., Brissaud, O., 2010. Kinetics of water adsorption on minerals and the breathing of the Martian regolith. Journal of Geophysical Research: Planets 115 (E10).

Bird, R. B., Stewart, W. E., Lightfoot, E. N., 2007. Transport phenomena. John Wiley & Sons.

Boushehri, A., Bzowski, J., Kestin, J., Mason, E. A., 1987. Equilibrium and transport properties of eleven polyatomic gases at low density. Journal of physical and chemical reference data 16 (3), 445–466.

Buffett, B. A., 2000. Clathrate hydrates. Annual Review of Earth and Planetary Sciences 28 (1), 477–507.

Cao, Z., Tester, J. W., Sparks, K. A., Trout, B. L., 2001. Molecular computations using robust hydrocarbon-water potentials for predicting gas hydrate phase equilibria. The Journal of Physical Chemistry B 105 (44), 10950–10960.

Carter, J., Poulet, F., Bibring, J.-P., Mangold, N., Murchie, S., 2013. Hydrous minerals on Mars as seen by the CRISM and OMEGA imaging spectrometers: Updated global view. Journal of Geophysical Research: Planets 118 (4), 831–858.

Chapoy, A., Gholinezhad, J., Tohidi, B., 2010. Experimental clathrate dissociations for the hydrogen + water and hydrogen + tetrabutylammonium bromide + water systems. Journal of Chemical & Engineering Data 55 (11), 5323–5327.

Chassefière, E., 2009. Metastable methane clathrate particles as a source of methane to the martian atmosphere. Icarus 204 (1), 137–144.

Chassefière, E., Leblanc, F., 2011a. Explaining the redox imbalance between the H and O escape fluxes at Mars by the oxidation of methane. Planetary and Space Science 59 (2-3), 218–226.

Chassefière, E., Leblanc, F., 2011b. Methane release and the carbon cycle on Mars. Planetary and Space Science 59 (2-3), 207–217.

Chastain, B. K., Chevrier, V., 2007. Methane clathrate hydrates as a potential source for martian atmospheric methane. Planetary and Space Science 55 (10), 1246–1256.

Chazallon, B., Kuhs, W. F., 2002. In situ structural properties of N_2-, O_2-, and air-clathrates by neutron diffraction. The Journal of chemical physics 117 (1), 308–320.

Chevrier, V. F., Hanley, J., Altheide, T. S., 2009. Stability of perchlorate hydrates and their liquid solutions at the Phoenix landing site, Mars. Geophysical Research Letters 36 (10).

Choukroun, M., Castillo-Rogez, J. C., Young, J. B., Mielke, R. E., 2010a. Preliminary comparison between the dissipation in CO_2 clathrates hydrates and water ice. In: Lunar and Planetary Science Conference. Vol. 41. p. 2172.

Choukroun, M., Grasset, O., Tobie, G., Sotin, C., 2010b. Stability of methane clathrate hydrates under pressure: Influence on outgassing processes of methane on Titan. Icarus 205 (2), 581–593.

Choukroun, M., Kieffer, S. W., Lu, X., Tobie, G., 2013. Clathrate hydrates: implications for exchange processes in the outer solar system. In: The Science of Solar System Ices. Springer, pp. 409–454.

Christensen, T. R., Johansson, T., Åkerman, H. J., Mastepanov, M., Malmer, N., Friborg, T., Crill, P., Svensson, B. H., 2004. Thawing sub-arctic permafrost: Effects on vegetation and methane emissions. Geophysical Research Letters 31 (4).

Circone, S., Kirby, S. H., Stern, L. A., 2005. Direct measurement of methane hydrate composition along the hydrate equilibrium boundary. The Journal of Physical Chemistry B 109 (19), 9468–9475.

Clifford, S. M., 1993. A model for the hydrologic and climatic behavior of water on Mars. Journal of Geophysical Research: Planets 98 (E6), 10973–11016.

Clifford, S. M., Parker, T. J., 2001. The evolution of the Martian hydrosphere: Implications for the fate of a primordial ocean and the current state of the northern plains. Icarus 154 (1), 40–79.

Court, R. W., Sephton, M. A., 2009. Investigating the contribution of methane produced by ablating micrometeorites to the atmosphere of Mars. Earth and Planetary Science Letters 288 (3-4), 382–385.

Cunningham, R. E., Williams, R. J. J., 1980. Diffusion in gases and porous media. Vol. 1. Springer.

Dartois, E., Deboffle, D., 2008. Methane clathrate hydrate FTIR spectrum - Implications for its cometary and planetary detection. Astronomy & Astrophysics 490 (3), L19–L22.

Dartois, E., Schmitt, B., 2009. Carbon dioxide clathrate hydrate FTIR spectrum - Near infrared combination modes for astrophysical remote detection. Astronomy & Astrophysics 504 (3), 869–873.

Davy, H., 1811. I. The Bakerian Lecture. On some of the combinations of oxymuriatic gas and oxygene, and on the chemical relations of these principles, to inflammable bodies. Philosophical Transactions of the Royal Society of London (101), 1–35.

Deaton, W. M., Frost, E. M., 1946. Gas hydrates and their relation to the operation of natural gas pipe lines. US Bureau of Mines Monograph 8:101.

Delsemme, A. H., Swings, P., 1952. Hydrates de gaz dans les noyaux cométaires et les grains interstellaires. In: Annales d'astrophysique. Vol. 15. Caisse nationale de la recherche scientifique, pp. 1–6.

Dickens, G. R., O'Neil, J. R., Rea, D. K., Owen, R. M., 1995. Dissociation of oceanic methane hydrate as a cause of the carbon isotope excursion at the end of the Paleocene. Paleoceanography 10 (6), 965–971.

Durham, W. B., Stern, L. A., Kirby, S. H., 2003. Ductile flow of methane hydrate. Canadian Journal of Physics 81 (1-2), 373–380.

Duxbury, N. S., Abyzov, S. S., Romanovsky, V. E., Yoshikawa, K., 2004. A combination of radar and thermal approaches to search for methane clathrate in the Martian subsurface. Planetary and Space Science 52 (1-3), 109–115.

Duxbury, N. S., Nealson, K. H., Romanovsky, V. E., 2001. On the possibility of clathrate hydrates on the Moon. Journal of Geophysical Research: Planets 106 (E11), 27811–27813.

Ehlmann, B. L., Edwards, C. S., 2014. Mineralogy of the Martian surface. Annual Review of Earth and Planetary Sciences 42, 291–315.

Ehlmann, B. L., Mustard, J. F., 2012. An in-situ record of major environmental transitions on early Mars at Northeast Syrtis Major. Geophysical research letters 39 (11).

Ehlmann, B. L., Mustard, J. F., Murchie, S. L., 2010. Geologic setting of serpentine deposits on Mars. Geophysical research letters 37 (6).

Elwood Madden, M., Ulrich, S., Szymcek, P., McCallum, S., Phelps, T., 2009. Experimental formation of massive hydrate deposits from accumulation of CH_4 gas bubbles within synthetic and natural sediments. Marine and Petroleum Geology 26 (3), 369–378.

Elwood Madden, M. E., Leeman, J. R., Root, M. J., Gainey, S., 2011. Reduced sulfur-carbon-water systems on Mars may yield shallow methane hydrate reservoirs. Planetary and Space Science 59, 203–206.

Elwood Madden, M. E., Ulrich, S. M., Onstott, T. C., Phelps, T. J., 2007. Salinity–induced hydrate dissociation: A mechanism for recent CH_4 release on Mars. Geophysical research letters 34 (11).

Encrenaz, T., Bézard, B., Owen, T., Lebonnois, S., Lefèvre, F., Greathouse, T., Richter, M., Lacy, J., Atreya, S., Wong, A., et al., 2005. Infrared imaging spectroscopy of Mars: H_2O mapping and determination of CO_2 isotopic ratios. Icarus 179 (1), 43–54.

Encrenaz, T., Greathouse, T. K., Richter, M. J., Lacy, J. H., Fouchet, T., Bézard, B., Lefèvre, F., Forget, F., Atreya, S. K., 2011. A stringent upper limit to SO_2 in the Martian atmosphere. Astronomy & Astrophysics 530, A37.

Etiope, G., 2015. Natural gas seepage. The Earth's Hydrocarbon Degassing. Springer, Switzerland 199, 199.

Etiope, G., 2018. Understanding the origin of methane on Mars through isotopic and molecular data from the ExoMars orbiter. Planetary and Space Science 159, 93–96.

Etiope, G., Ionescu, A., 2015. Low-temperature catalytic CO_2 hydrogenation with geological quantities of ruthenium: a possible abiotic CH_4 source in chromitite-rich serpentinized rocks. Geofluids 15 (3), 438–452.

Etiope, G., Oehler, D. Z., 2019. Methane spikes, background seasonality and non-detections on Mars: A geological perspective. Planetary and Space Science 168, 52–61.

Etiope, G., Sherwood Lollar, B., 2013. Abiotic methane on Earth. Reviews of Geophysics 51 (2), 276–299.

Falabella, B. J., 1975. A study of natural gas hydrates. Ph. D. Dis., Univ. of Massachusetts.

Farrell, W. M., Delory, G. T., Atreya, S. K., 2006. Martian dust storms as a possible sink of atmospheric methane. Geophysical research letters 33 (21).

Fateen, S.-E. K., Khalil, M. M., Elnabawy, A. O., 2013. Semi-empirical correlation for binary interaction parameters of the Peng–Robinson equation of state with the van der Waals mixing rules for the prediction of high-pressure vapor–liquid equilibrium. Journal of advanced research 4 (2), 137–145.

Feldman, W. C., Prettyman, T. H., Maurice, S., Plaut, J. J., Bish, D. L., Vaniman, D. T., Mellon, M. T., Metzger, A. E., Squyres, S. W., Karunatillake, S., et al., 2004. Global distribution of near-surface hydrogen on Mars. Journal of Geophysical Research: Planets 109 (E9).

Flynn, G. J., 1996. The delivery of organic matter from asteroids and comets to the early surface of Mars. Earth, Moon, and Planets 72 (1), 469–474.

Fonti, S., Mancarella, F., Liuzzi, G., Roush, T. L., Frouard, M. C., Murphy, J., Blanco, A., 2015. Revisiting the identification of methane on Mars using TES data. Astronomy & Astrophysics 581, A136.

Fonti, S., Marzo, G. A., 2010. Mapping the methane on Mars. Astronomy & Astrophysics 512, A51.

Forget, F., Hourdin, F., Fournier, R., Hourdin, C., Talagrand, O., Collins, M., Lewis, S. R., Read, P. L., Huot, J.-P., 1999. Improved general circulation models of the Martian atmosphere from the surface to above 80 km. Journal of Geophysical Research: Planets 104 (E10), 24155–24175.

Formisano, V., Atreya, S., Encrenaz, T., Ignatiev, N., Giuranna, M., 2004. Detection of methane in the atmosphere of Mars. Science 306 (5702), 1758–1761.

Fries, M., Christou, A., Archer, D., Conrad, P., Cooke, W., Eigenbrode, J., ten Kate, I. L., Matney, M., Niles, P., Sykes, M., et al., 2016. A cometary origin for martian atmospheric methane. Geochem. Perspect. Lett. 2 (1), 10–22.

Gainey, S. R., Elwood Madden, M. E., 2012. Kinetics of methane clathrate formation and dissociation under Mars relevant conditions. Icarus 218 (1), 513–524.

Gao, G., Daridon, J.-L., Saint-Guirons, H., Xans, P., Montel, F., 1992. A simple correlation to evaluate binary interaction parameters of the Peng-Robinson equation of state: binary light hydrocarbon systems. Fluid phase equilibria 74, 85–93.

Geminale, A., Formisano, V., Giuranna, M., 2008. Methane in Martian atmosphere: Average spatial, diurnal, and seasonal behaviour. Planetary and Space Science 56 (9), 1194–1203.

Geminale, A., Formisano, V., Sindoni, G., 2011. Mapping methane in Martian atmosphere with PFS-MEX data. Planetary and Space Science 59 (2), 137–148.

Gibb, E. L., Mumma, M. J., Russo, N. D., DiSanti, M. A., Magee-Sauer, K., 2003. Methane in Oort cloud comets. Icarus 165 (2), 391–406.

Giuranna, M., Viscardy, S., Daerden, F., Neary, L., Etiope, G., Oehler, D., Formisano, V., et al., 2019. Independent confirmation of a methane spike on Mars and a source region east of Gale Crater. Nature Geoscience 12, 326–332.

Gloesener, E., Karatekin, Ö., Dehant, V., submitted. Stability and composition of CH_4-rich clathrate hydrates in the present martian subsurface.

Gough, R. V., Tolbert, M. A., McKay, C. P., Toon, O. B., 2010. Methane adsorption on a Martian soil analog: An abiogenic explanation for methane variability in the Martian atmosphere. Icarus 207 (1), 165–174.

Gough, R. V., Turley, J. J., Ferrell, G. R., Cordova, K. E., Wood, S. E., DeHaan, D. O., McKay, C. P., Toon, O. B., Tolbert, M. A., 2011. Can rapid loss and high variability of Martian methane be explained by surface H_2O_2? Planetary and Space Science 59 (2-3), 238–246.

Graham, T., 1833. On the law of the diffusion of gases. The London, Edinburgh, and Dublin Philosophical Magazine and Journal of Science 2 (9), 175–190.

Grott, M., Breuer, D., 2010. On the spatial variability of the Martian elastic lithosphere thickness: Evidence for mantle plumes? Journal of Geophysical Research: Planets 115 (E3).

Grotzinger, J. P., Hayes, A. G., Lamb, M. P., McLennan, S. M., 2013. Sedimentary processes on Earth, Mars, Titan, and Venus. Comparative Climatology of Terrestrial Planets 1, 439–472.

Haberle, R. M., 1998. Early Mars climate models. Journal of Geophysical Research: Planets 103 (E12), 28467–28479.

Haberle, R. M., Clancy, R. T., Forget, F., Smith, M. D., Zurek, R. W., 2017. The atmosphere and climate of Mars. Cambridge University Press.

Hahn, B. C., McLennan, S. M., Klein, E. C., 2011. Martian surface heat production and crustal heat flow from Mars Odyssey Gamma-Ray spectrometry. Geophysical Research Letters 38 (14).

Handa, Y. P., Tse, J. S., 1986. Thermodynamic properties of empty lattices of structure I and structure II clathrate hydrates. The Journal of Physical Chemistry 90 (22), 5917–5921.

Hauck, S. A., Phillips, R. J., 2002. Thermal and crustal evolution of Mars. Journal of Geophysical Research: Planets 107 (E7), 6–1.

Hecht, M. H., Kounaves, S. P., Quinn, R. C., West, S. J., Young, S. M. M., Ming, D. W., Catling, D. C., Clark, B. C., Boynton, W. V., Hoffman, J., et al., 2009. Detection of perchlorate and the soluble chemistry of martian soil at the Phoenix lander site. Science 325 (5936), 64–67.

Herr, K. C., Pimentel, G. C., 1969. Infrared absorptions near three microns recorded over the polar cap of Mars. Science 166 (3904), 496–499.

Herri, J.-M., Chassefière, E., 2012. Carbon dioxide, argon, nitrogen and methane clathrate hydrates: Thermodynamic modelling, investigation of their stability in Martian atmospheric conditions and variability of methane trapping. Planetary and Space Science 73 (1), 376–386.

Ho, C. K., Webb, S. W., 2006. Gas transport in porous media. Vol. 20. Springer.

Holder, G. D., Corbin, G., Papadopoulos, K. D., 1980. Thermodynamic and molecular properties of gas hydrates from mixtures containing methane, argon, and krypton. Industrial & Engineering Chemistry Fundamentals 19 (3), 282–286.

Holmes, J. A., Lewis, S. R., Patel, M. R., 2015. Analysing the consistency of martian methane observations by investigation of global methane transport. Icarus 257, 23–32.

Hudson, T. L., 2008. Growth, diffusion, and loss of subsurface ice on Mars: experiments and models. Ph.D. thesis, California Institute of Technology.

Jakosky, B. M., Mellon, M. T., Varnes, E. S., Feldman, W. C., Boynton, W. V., Haberle, R. M., 2005. Mars low-latitude neutron distribution: Possible remnant near-surface water ice and a mechanism for its recent emplacement. Icarus 175 (1), 58–67.

Jeffrey, G. A., 1984. Hydrate inclusion compounds. Journal of inclusion phenomena 1 (3), 211–222.

Jensen, S. K., Skibsted, J., Jakobsen, H. J., ten Kate, I. L., Gunnlaugsson, H. P., Merrison, J. P., Finster, K., Bak, E., Iversen, J. J., Kondrup, J. C., Nørnberg, P., 2014. A sink for methane on Mars? The answer is blowing in the wind. Icarus 236, 24–27.

Jhaveri, J., Robinson, D. B., 1965. Hydrates in the methane-nitrogen system. The Canadian Journal of Chemical Engineering 43 (2), 75–78.

Kamata, S., Nimmo, F., Sekine, Y., Kuramoto, K., Noguchi, N., Kimura, J., Tani, A., 2019. Pluto's ocean is capped and insulated by gas hydrates. Nature Geoscience 12 (6), 407.

Keppler, F., Vigano, I., McLeod, A., Ott, U., Früchtl, M., Röckmann, T., 2012. Ultraviolet-radiation-induced methane emissions from meteorites and the Martian atmosphere. Nature 486 (7401), 93.

Kieffer, H. H., Martin, T. Z., Peterfreund, A. R., Jakosky, B. M., Miner, E. D., Palluconi, F. D., 1977. Thermal and albedo mapping of Mars during the Viking primary mission. Journal of Geophysical Research 82 (28), 4249–4291.

Kieffer, S. W., Lu, X., Bethke, C. M., Spencer, J. R., Marshak, S., Navrotsky, A., 2006. A clathrate reservoir hypothesis for Enceladus' south polar plume. Science 314 (5806), 1764–1766.

Kite, E. S., Gao, P., Goldblatt, C., Mischna, M. A., Mayer, D. P., Yung, Y. L., 2017. Methane bursts as a trigger for intermittent lake-forming climates on post-Noachian Mars. Nature Geoscience 10 (10), 737.

Klauda, J. B., Sandler, S. I., 2002. Ab initio intermolecular potentials for gas hydrates and their predictions. The Journal of Physical Chemistry B 106 (22), 5722–5732.

Klauda, J. B., Sandler, S. I., 2003. Phase behavior of clathrate hydrates: a model for single and multiple gas component hydrates. Chemical engineering science 58 (1), 27–42.

Klauda, J. B., Sandler, S. I., 2005. Global distribution of methane hydrate in ocean sediment. Energy & Fuels 19 (2), 459–470.

Klinkenberg, L. J., et al., 1941. The permeability of porous media to liquids and gases. In: Drilling and production practice. American Petroleum Institute.

Kok, J. F., Renno, N. O., 2009. Electrification of wind-blown sand on Mars and its implications for atmospheric chemistry. Geophysical Research Letters 36 (5).

Komatsu, G., Ori, G. G., Cardinale, M., Dohm, J. M., Baker, V. R., Vaz, D. A., Ishimaru, R., Namiki, N., Matsui, T., 2011. Roles of methane and carbon dioxide in geological processes on Mars. Planetary and Space Science 59 (2-3), 169–181.

Korablev, O., Montmessin, F., Trokhimovskiy, A., Fedorova, A. A., Shakun, A. V., Grigoriev, A. V., Moshkin, B. E., Ignatiev, N. I., Forget, F., Lefèvre, F., et al., 2018. The atmospheric chemistry suite (ACS) of three spectrometers for the ExoMars 2016 Trace Gas Orbiter. Space science reviews 214 (1), 7.

Korablev, O., Vandaele, A. C., Montmessin, F., Fedorova, A., Trokhimovskiy, A., Forget, F., et al., 2019. No detection of methane on Mars from early ExoMars Trace Gas Orbiter observations. Nature 568, 517–520.

Krasnopolsky, V. A., 1993. Photochemistry of the Martian atmosphere (mean conditions). Icarus 101 (2), 313–332.

Krasnopolsky, V. A., 2006. Some problems related to the origin of methane on Mars. Icarus 180 (2), 359–367.

Krasnopolsky, V. A., 2007. Comment on "Methane on Mars: A product of H_2O photolysis in the presence of CO" by A. Bar-Nun and V. Dimitrov. Icarus 188 (2), 540–542.

Krasnopolsky, V. A., 2012. Search for methane and upper limits to ethane and SO_2 on Mars. Icarus 217 (1), 144–152.

Krasnopolsky, V. A., Bjoraker, G. L., Mumma, M. J., Jennings, D. E., 1997. High-resolution spectroscopy of Mars at 3.7 and 8 μm: A sensitive search for H_2O_2, H_2CO, HCl, and CH_4, and detection of HDO. Journal of Geophysical Research: Planets 102 (E3), 6525–6534.

Krasnopolsky, V. A., Maillard, J. P., Owen, T. C., 2004. Detection of methane in the martian atmosphere: evidence for life? Icarus 172 (2), 537–547.

Kress, M. E., McKay, C. P., 2004. Formation of methane in comet impacts: implications for Earth, Mars, and Titan. Icarus 168 (2), 475–483.

Kuhs, W. F., Klapproth, A., Gotthardt, F., Techmer, K., Heinrichs, T., 2000. The formation of meso-and macroporous gas hydrates. Geophysical research letters 27 (18), 2929–2932.

Lakhlifi, A., Dahoo, P. R., Picaud, S., Mousis, O., 2015. A simple van't Hoff law for calculating Langmuir constants in clathrate hydrates. Chemical Physics 448, 53–60.

Larson, S. D., 1955. Phase studies of the two-component carbon dioxide-water system, involving the carbon dioxide hydrate. Ph. D. Thesis, Univ. of Michigan.

Laskar, J., Correia, A. C. M., Gastineau, M., Joutel, F., Levrard, B., Robutel, P., 2004. Long term evolution and chaotic diffusion of the insolation quantities of Mars. Icarus 170 (2), 343–364.

Lasue, J., Quesnel, Y., Langlais, B., Chassefière, E., 2015. Methane storage capacity of the early martian cryosphere. Icarus 260, 205–214.

Lefèvre, F., Forget, F., 2009. Observed variations of methane on Mars unexplained by known atmospheric chemistry and physics. Nature 460 (7256), 720.

Lele, A., 2014. Mission Mars: India's Quest for the Red Planet. Springer.

Lellouch, E., Encrenaz, T., de Graauw, T., Erard, S., Morris, P., Crovisier, J., Feuchtgruber, H., Girard, T., Burgdorf, M., 2000. The 2.4–45 μm spectrum of Mars observed with the infrared space observatory. Planetary and Space Science 48 (12-14), 1393–1405.

Li, H., Yan, J., 2009. Evaluating cubic equations of state for calculation of vapor–liquid equilibrium of CO_2 and CO_2-mixtures for CO_2 capture and storage processes. Applied Energy 86 (6), 826–836.

Lipenkov, V. Y., Istomin, V. A., 2001. On the stability of air clathrate-hydrate crystals in subglacial Lake Vostok, Antarctica. Materialy Glyatsiol. Issled 91 (129), 2001.

Lokshin, K. A., Zhao, Y., He, D., Mao, W. L., Mao, H.-K., Hemley, R. J., Lobanov, M. V., Greenblatt, M., 2004. Structure and dynamics of hydrogen molecules in the novel clathrate hydrate by high pressure neutron diffraction. Physical Review Letters 93 (12), 125503.

Loveday, J. S., Nelmes, R. J., 2008. High-pressure gas hydrates. Physical Chemistry Chemical Physics 10 (7), 937–950.

Loveday, J. S., Nelmes, R. J., Guthrie, M., Belmonte, S. A., Allan, D. R., Klug, D. D., Tse, J. S., Handa, Y. P., 2001a. Stable methane hydrate above 2 GPa and the source of Titan's atmospheric methane. Nature 410 (6829), 661.

Loveday, J. S., Nelmes, R. J., Guthrie, M., Klug, D. D., Tse, J. S., 2001b. Transition from cage clathrate to filled ice: the structure of methane hydrate III. Physical Review Letters 87 (21), 215501.

Luspay-Kuti, A., Mousis, O., Hässig, M., Fuselier, S. A., Lunine, J. I., Marty, B., Mandt, K. E., Wurz, P., Rubin, M., 2016. The presence of clathrates in comet 67P/Churyumov-Gerasimenko. Science advances 2 (4), e1501781.

Lyons, J. R., Manning, C., Nimmo, F., 2005. Formation of methane on Mars by fluid-rock interaction in the crust. Geophysical Research Letters 32 (13).

Macdonald, A. H., Fyfe, W. S., 1985. Rate of serpentinization in seafloor environments. Tectonophysics 116 (1-2), 123–135.

Maguire, W. C., 1977. Martian isotopic ratios and upper limits for possible minor constituents as derived from Mariner 9 infrared spectrometer data. Icarus 32 (1), 85–97.

Makogon, T. Y., Sloan, E. D. J., 1994. Phase equilibrium for methane hydrate from 190 to 262 K. Journal of Chemical and Engineering Data 39 (2), 351–353.

Makogon, Y. F., 1965. Hydrate formation in the gas-bearing beds under permafrost conditions. Gazovaia Promyshlennost 5, 14–15.

Manakov, A. Y., Voronin, V. I., Kurnosov, A. V., Teplykh, A. E., Komarov, V. Y., Dyadin, Y. A., 2004. Structural investigations of argon

hydrates at pressures up to 10 kbar. Journal of inclusion phenomena and macrocyclic chemistry 48 (1-2), 11–18.

Mao, W. L., Mao, H.-k., Goncharov, A. F., Struzhkin, V. V., Guo, Q., Hu, J., Shu, J., Hemley, R. J., Somayazulu, M., Zhao, Y., 2002. Hydrogen clusters in clathrate hydrate. Science 297 (5590), 2247–2249.

Marboeuf, U., Mousis, O., Ehrenreich, D., Alibert, Y., Cassan, A., Wakelam, V., Beaulieu, J.-P., 2008. Composition of ices in low-mass extrasolar planets. The Astrophysical Journal 681 (2), 1624.

Marboeuf, U., Mousis, O., Petit, J.-M., Schmitt, B., 2009. Clathrate hydrates formation in short-period comets. The Astrophysical Journal 708 (1), 812.

Marlow, J. J., LaRowe, D. E., Ehlmann, B. L., Amend, J. P., Orphan, V. J., 2014. The potential for biologically catalyzed anaerobic methane oxidation on ancient Mars. Astrobiology 14 (4), 292–307.

Marshall, D. R., Saito, S., Kobayashi, R., 1964. Hydrates at high pressures: Part I. Methane-water, argon-water, and nitrogen-water systems. AIChE Journal 10 (2), 202–205.

Maslin, M., Owen, M., Betts, R., Day, S., Jones, T. D., Ridgwell, A., 2010. Gas hydrates: past and future geohazard? Philosophical Transactions of the Royal Society of London A: Mathematical, Physical and Engineering Sciences 368 (1919), 2369–2393.

Mason, E. A., Malinauskas, A. P., 1983. Gas transport in porous media: the dusty-gas model. Vol. 17. Elsevier Science Ltd.

Max, M., Johnson, A., Clifford, S., 2011. Methane hydrate on Mars: a resource-rich stepping stone to the outer planets. In: Proceedings of the 7th International Conference on Gas Hydrates (ICGH 2011), Edinburgh, Scotland.

Max, M. D., 2003. Natural gas hydrate in oceanic and permafrost environments. Vol. 5. Springer Science & Business Media.

Max, M. D., Clifford, S. M., 2000. The state, potential distribution, and biological implications of methane in the Martian crust. Journal of Geophysical Research: Planets 105 (E2), 4165–4171.

McGovern, P. J., Solomon, S. C., Smith, D. E., Zuber, M. T., Simons, M., Wieczorek, M. A., Phillips, R. J., Neumann, G. A., Aharonson, O., Head, J. W., 2002. Localized gravity/topography admittance and

correlation spectra on Mars: Implications for regional and global evolution. Journal of Geophysical Research: Planets 107 (E12), 19–1–19–25.

McGovern, P. J., Solomon, S. C., Smith, D. E., Zuber, M. T., Simons, M., Wieczorek, M. A., Phillips, R. J., Neumann, G. A., Aharonson, O., Head, J. W., 2004. Correction to "Localized gravity/topography admittance and correlation spectra on Mars: Implications for regional and global evolution". Journal of Geophysical Research: Planets 109 (E07007).

McKoy, V., Sinanoğlu, O., 1963. Theory of dissociation pressures of some gas hydrates. The Journal of Chemical Physics 38 (12), 2946–2956.

McMahon, S., Parnell, J., Blamey, N. J. F., 2013. Sampling methane in basalt on Earth and Mars. International Journal of Astrobiology 12 (2), 113–122.

Mellon, M. T., Feldman, W. C., Prettyman, T. H., 2004. The presence and stability of ground ice in the southern hemisphere of Mars. Icarus 169, 324–340.

Mellon, M. T., Jakosky, B. M., 1993. Geographic variations in the thermal and diffusive stability of ground ice on Mars. Journal of Geophysical Research: Planets 98 (E2), 3345–3364.

Meslin, P.-Y., Gough, R., Lefèvre, F., Forget, F., 2011. Little variability of methane on Mars induced by adsorption in the regolith. Planetary and Space Science 59 (2-3), 247–258.

Miller, S. L., 1961. The occurrence of gas hydrates in the solar system. Proceedings of the National Academy of Sciences 47 (11), 1798–1808.

Miller, S. L., Smythe, W. D., 1970. Carbon dioxide clathrate in the Martian ice cap. Science 170 (3957), 531–533.

Millour, E., Forget, F., Spiga, A., Navarro, T., Madeleine, J.-B., Montabone, L., Pottier, A., Lefevre, F., Montmessin, F., Chaufray, J.-Y., et al., 2015. The Mars Climate Database (MCD version 5.2). EPSC Abstracts 10, 438.

Mischna, M. A., Allen, M., Richardson, M. I., Newman, C. E., Toigo, A. D., 2011. Atmospheric modeling of Mars methane surface releases. Planetary and Space Science 59, 227–237.

Mohammadi, A. H., Richon, D., 2010. Ice–clathrate hydrate–gas phase equilibria for air, oxygen, nitrogen, carbon monoxide, methane, or ethane + water system. Industrial & Engineering Chemistry Research 49 (8), 3976–3979.

Mohammadi, A. H., Richon, D., 2011. Ice–clathrate hydrate–gas phase equilibria for argon + water and carbon dioxide + water systems. Industrial & Engineering Chemistry Research 50 (19), 11452–11454.

Moores, J. E., Gough, V. R., Martinez, G. M., Meslin, P.-Y., Smith, C. L., Atreya, S. K., Mahaffy, P. R., Newman, C. E., Webster, C. R., 2019. Methane seasonal cycle at Gale Crater on Mars consistent with regolith adsorption and diffusion. Nature Geoscience 12, 321–325.

Mousis, O., Chassefiere, E., Holm, N. G., Bouquet, A., Waite, J. H., Geppert, W. D., Picaud, S., Aikawa, Y., Ali-Dib, M., Charlou, J.-L., et al., 2015. Methane clathrates in the solar system. Astrobiology 15 (4), 308–326.

Mousis, O., Chassefière, E., Lasue, J., Chevrier, V., Madden, M. E. E., Lakhlifi, A., Lunine, J. I., Montmessin, F., Picaud, S., Schmidt, F., et al., 2013a. Volatile trapping in Martian clathrates. Space Science Reviews 174 (1-4), 213–250.

Mousis, O., Lunine, J. I., Mandt, K. E., Schindhelm, E., Weaver, H. A., Stern, S. A., Waite, J. H., Gladstone, R., Moudens, A., 2013b. On the possible noble gas deficiency of Pluto's atmosphere. Icarus 225 (1), 856–861.

Mousis, O., Lunine, J. I., Picaud, S., Cordier, D., 2010. Volatile inventories in clathrate hydrates formed in the primordial nebula. Faraday discussions 147, 509–525.

Mousis, O., Simon, J.-M., Bellat, J.-P., Schmidt, F., Bouley, S., Chassefière, E., Sautter, V., Quesnel, Y., Picaud, S., Lectez, S., 2016. Martian zeolites as a source of atmospheric methane. Icarus 278, 1–6.

Mumma, M., Novak, R., DiSanti, M., Bonev, B., Dello Russo, N., 2004. Detection and mapping of methane and water on Mars. In: Bulletin of the American Astronomical Society. Vol. 36. p. 1127.

Mumma, M. J., Villanueva, G. L., Novak, R. E., Hewagama, T., Bonev, B. P., DiSanti, M. A., Mandell, A. M., Smith, M. D., 2009. Strong release of methane on Mars in northern summer 2003. Science 323 (5917), 1041–1045.

Murchie, S. L., Mustard, J. F., Ehlmann, B. L., Milliken, R. E., Bishop, J. L., McKeown, N. K., Noe Dobrea, E. Z., Seelos, F. P., Buczkowski, D. L., Wiseman, S. M., et al., 2009. A synthesis of Martian aqueous mineralogy after 1 Mars year of observations from the Mars Reconnaissance Orbiter. Journal of Geophysical Research: Planets 114 (E2).

Nagashima, H. D., Nemoto, K., Ohmura, R., 2018. Phase equilibrium for argon clathrate hydrate at the temperatures from 197.6 K to 274.1 K. The Journal of Chemical Thermodynamics 127, 86–91.

Nair, H., Allen, M., Anbar, A. D., Yung, Y. L., Clancy, R. T., 1994. A photochemical model of the Martian atmosphere. Icarus 111 (1), 124–150.

Neukum, G., Jaumann, R., Hoffmann, H., Hauber, E., Head, J., Basilevsky, A., Ivanov, B., Werner, S., Van Gasselt, S., Murray, J., et al., 2004. Recent and episodic volcanic and glacial activity on Mars revealed by the High Resolution Stereo Camera. Nature 432 (7020), 971.

Ng, H.-J., Robinson, D. B., 1985. Hydrate formation in systems containing methane, ethane, propane, carbon dioxide or hydrogen sulfide in the presence of methanol. Fluid Phase Equilibria 21 (1-2), 145–155.

Oehler, D. Z., Etiope, G., 2017. Methane seepage on Mars: where to look and why. Astrobiology 17 (12), 1233–1264.

Ojha, L., Wilhelm, M. B., Murchie, S. L., McEwen, A. S., Wray, J. J., Hanley, J., Massé, M., Chojnacki, M., 2015. Spectral evidence for hydrated salts in recurring slope lineae on Mars. Nature Geoscience 8 (11), 829–832.

Osterloo, M. M., Hamilton, V. E., Bandfield, J. L., Glotch, T. D., Baldridge, A. M., Christensen, P. R., Tornabene, L. L., Anderson, F. S., 2008. Chloride-bearing materials in the southern highlands of Mars. Science 319 (5870), 1651–1654.

Oze, C., Sharma, M., 2005. Have olivine, will gas: Serpentinization and the abiogenic production of methane on Mars. Geophysical Research Letters 32 (10).

Parro, L. M., Jiménez-Díaz, A., Mansilla, F., Ruiz, J., 2017. Present-day heat flow model of Mars. Scientific Reports 7.

Pellenbarg, R. E., Max, M. D., Clifford, S. M., 2003. Methane and carbon dioxide hydrates on Mars: Potential origins, distribution, detection, and implications for future in situ resource utilization. Journal of Geophysical Research: Planets 108 (E4).

Peng, D.-Y., Robinson, D. B., 1976. A new two-constant equation of state. Industrial & Engineering Chemistry Fundamentals 15 (1), 59–64.

Pla-García, J., Rafkin, S. C. R., Karatekin, Ö., Gloesener, E., 2019. Comparing MSL Curiosity rover TLS-SAM methane measurements with Mars Regional Atmospheric Modeling System (MRAMS) atmospheric transport experiments. Journal of Geophysical Research: Planets.

Pommerol, A., Schmitt, B., Beck, P., Brissaud, O., 2009. Water sorption on Martian regolith analogs: Thermodynamics and near-infrared reflectance spectroscopy. Icarus 204 (1), 114–136.

Pratt, R. M., Ballard, A. L., Sloan Jr, E. D., 2001. Beware of singularities when calculating clathrate hydrate cell potentials! AIChE journal 47 (8), 1897–1898.

Press, W. H., Teukolsky, S. A., Vetterling, W. T., Flannery, B. P., 1997. Numerical Recipes in Fortran 77: The Art of Scientific Computing (Vol. 1 of Fortran Numerical Recipes). Cambridge University Press.

Prieto-Ballesteros, O., Kargel, J. S., Fairén, A. G., Fernández-Remolar, D. C., Dohm, J. M., Amils, R., 2006. Interglacial clathrate destabilization on Mars: Possible contributing source of its atmospheric methane. Geology 34 (3), 149–152.

Prieto-Ballesteros, O., Kargel, J. S., Fernández-Sampedro, M., Selsis, F., Martínez, E. S., Hogenboom, D. L., 2005. Evaluation of the possible presence of clathrate hydrates in Europa's icy shell or seafloor. Icarus 177 (2), 491–505.

Putzig, N. E., Mellon, M. T., 2007. Apparent thermal inertia and the surface heterogeneity of Mars. Icarus 191 (1), 68–94.

Ranieri, U., Koza, M. M., Kuhs, W. F., Klotz, S., Falenty, A., Gillet, P., Bove, L. E., 2017. Fast methane diffusion at the interface of two clathrate structures. Nature communications 8 (1), 1076.

Robinson, D. B., Hutton, J. B., et al., 1967. Hydrate formation in systems containing methane, hydrogen sulphide and carbon dioxide. Journal of Canadian Petroleum Technology 6 (01), 6–9.

Rodriguez, J. A. P., Kargel, J., Crown, D. A., Bleamaster, L. F., Tanaka, K. L., Baker, V., Miyamoto, H., Dohm, J. M., Sasaki, S., Komatsu, G., 2006. Headward growth of chasmata by volatile outbursts, collapse, and drainage: Evidence from Ganges chaos, Mars. Geophysical Research Letters 33 (18).

Roos-Serote, M., Atreya, S. K., Webster, C. R., Mahaffy, P. R., 2016. Cometary origin of atmospheric methane variations on Mars unlikely. Journal of Geophysical Research: Planets 121 (10), 2108–2119.

Root, M. J., Elwood Madden, M. E., 2012. Potential effects of obliquity change on gas hydrate stability zones on Mars. Icarus 218 (1), 534–544.

Ross, R. G., Andersson, P., Bäckström, G., 1981. Unusual PT dependence of thermal conductivity for a clathrate hydrate. Nature 290 (5804), 322.

Ruff, S. W., 2004. Spectral evidence for zeolite in the dust on Mars. Icarus 168 (1), 131–143.

Scanlon, B. R., Nicot, J. P., Massmann, J. W., 2002. Soil gas movement in unsaturated systems. Soil physics companion 389, 297–341.

Schorghofer, N., Aharonson, O., 2005. Stability and exchange of subsurface ice on Mars. Journal of Geophysical Research: Planets 110 (E5).

Schorghofer, N., Edgett, K. S., 2006. Seasonal surface frost at low latitudes on Mars. Icarus 180 (2), 321–334.

Schuerger, A. C., Moores, J. E., Clausen, C. A., Barlow, N. G., Britt, D. T., 2012. Methane from UV-irradiated carbonaceous chondrites under simulated Martian conditions. Journal of Geophysical Research: Planets 117 (E8).

Scott, H. P., Hemley, R. J., Mao, H.-k., Herschbach, D. R., Fried, L. E., Howard, W. M., Bastea, S., 2004. Generation of methane in the Earth's mantle: in situ high pressure–temperature measurements of carbonate reduction. Proceedings of the National Academy of Sciences 101 (39), 14023–14026.

Skiba, S. S., Larionov, E. G., Manakov, A. Y., Kolesov, B. A., Ancharov, A. I., Aladko, E. Y., 2009. Double clathrate hydrate of propane and

hydrogen. Journal of Inclusion Phenomena and Macrocyclic Chemistry 63 (3-4), 383–386.

Sloan, E. D., Koh, C. A., 2007. Clathrate hydrates of natural gases. 3rd ed., CRC press, Boca Raton.

Smith, M. D., 2002. The annual cycle of water vapor on Mars as observed by the Thermal Emission Spectrometer. Journal of Geophysical Research: Planets 107 (E11), 25–1.

Smith, N. J. P., Shepherd, T. J., Styles, M. T., Williams, G. M., 2005. Hydrogen exploration: a review of global hydrogen accumulations and implications for prospective areas in NW Europe. In: Geological Society, London, Petroleum Geology Conference series. Vol. 6. Geological Society of London, pp. 349–358.

Smith, P. H., Tamppari, L. K., Arvidson, R. E., Bass, D., Blaney, D., Boynton, W. V., Carswell, A., et al., 2009. H_2O at the Phoenix Landing Site. Science 325 (5936), 58–61.

Stevens, A. H., Patel, M. R., Lewis, S. R., 2015. Numerical modelling of the transport of trace gases including methane in the subsurface of Mars. Icarus 250, 587–594.

Stevens, A. H., Patel, M. R., Lewis, S. R., 2017. Modelled isotopic fractionation and transient diffusive release of methane from potential subsurface sources on Mars. Icarus 281, 240–247.

Strobel, T. A., Koh, C. A., Sloan, E. D., 2009. Thermodynamic predictions of various tetrahydrofuran and hydrogen clathrate hydrates. Fluid Phase Equilibria 280 (1-2), 61–67.

Sun, R., Duan, Z., 2005. Prediction of ch_4 and co_2 hydrate phase equilibrium and cage occupancy from ab initio intermolecular potentials. Geochimica et Cosmochimica Acta 69 (18), 4411–4424.

Takenouchi, S., Kennedy, G. C., 1965. Dissociation pressures of the phase $CO_2 \cdot$ 5 3/4 H_2O. The Journal of geology 73 (2), 383–390.

Taylor, G. J., Stopar, J. D., Boynton, W. V., Karunatillake, S., Keller, J. M., Brückner, J., Wänke, H., Dreibus, G., Kerry, K. E., Reedy, R. C., et al., 2006. Variations in K/Th on Mars. Journal of Geophysical Research: Planets 111 (E3).

Temel, O., Karatekin, Ö., Gloesener, E., Mischna, M. A., van Beeck, J., 2019. Atmospheric transport of subsurface, sporadic, time-varying methane releases on Mars. Icarus 325, 39–54.

Thomas, C., Mousis, O., Picaud, S., Ballenegger, V., 2009. Variability of the methane trapping in martian subsurface clathrate hydrates. Planetary and Space Science 57 (1), 42–47.

Thomas, C., Picaud, S., Ballenegger, V., Mousis, O., 2010. Sensitivity of predicted gas hydrate occupancies on treatment of intermolecular interactions. The Journal of chemical physics 132 (10), 104510.

Thorstenson, D. C., Pollock, D. W., 1989a. Gas transport in unsaturated porous media: The adequacy of Fick's law. Reviews of Geophysics 27 (1), 61–78.

Thorstenson, D. C., Pollock, D. W., 1989b. Gas transport in unsaturated zones: Multicomponent systems and the adequacy of Fick's laws. Water Resources Research 25 (3), 477–507.

Tobie, G., Lunine, J. I., Sotin, C., 2006. Episodic outgassing as the origin of atmospheric methane on Titan. Nature 440 (7080), 61.

Tse, J. S., 1990. Thermal expansion of structure-H clathrate hydrates. Journal of inclusion phenomena and molecular recognition in chemistry 8 (1-2), 25–32.

Tse, J. S., White, M. A., 1988. Origin of glassy crystalline behavior in the thermal properties of clathrate hydrates: a thermal conductivity study of tetrahydrofuran hydrate. The Journal of Physical Chemistry 92 (17), 5006–5011.

Tung, H. C., Bramall, N. E., Price, P. B., 2005. Microbial origin of excess methane in glacial ice and implications for life on Mars. Proceedings of the National Academy of Sciences 102 (51), 18292–18296.

van der Waals, J. H., Platteeuw, J. C., 1959. Clathrate solutions. Advances in Chemical Physics, Volume 2, 1–57.

Vandaele, A. C., Neefs, E., Drummond, R., Thomas, I. R., Daerden, F., Lopez-Moreno, J.-J., Rodriguez, J., Patel, M. R., Bellucci, G., Allen, M., et al., 2015. Science objectives and performances of NOMAD, a spectrometer suite for the ExoMars TGO mission. Planetary and Space Science 119, 233–249.

Vasavada, A. R., Piqueux, S., Lewis, K. W., Lemmon, M. T., Smith, M. D., 2017. Thermophysical properties along Curiosity's traverse in Gale crater, Mars, derived from the REMS ground temperature sensor. Icarus 284, 372–386.

Villanueva, G. L., Mumma, M. J., Novak, R. E., Radeva, Y. L., Käufl, H. U., Smette, A., Tokunaga, A., Khayat, A., Encrenaz, T., Hartogh, P., 2013. A sensitive search for organics (CH_4, CH_3OH, H_2CO, C_2H_6, C_2H_2, C_2H_4), hydroperoxyl (HO_2), nitrogen compounds (N_2O, NH_3, HCN) and chlorine species (HCl, CH_3Cl) on Mars using ground-based high-resolution infrared spectroscopy. Icarus 223 (1), 11–27.

Viscardy, S., Daerden, F., Neary, L., 2016. Formation of layers of methane in the atmosphere of Mars after surface release. Geophysical Research Letters 43 (5), 1868–1875.

Vu, T. H., Gloesener, E., Choukroun, M., Ibourichene, A., Hodyss, R., 2014. Experimental study on the effect of ammonia on the phase behavior of tetrahydrofuran clathrates. The Journal of Physical Chemistry B 118 (47), 13371–13377.

Wallace, D., Sagan, C., 1979. Evaporation of ice in planetary atmospheres: Ice-covered rivers on Mars. Icarus 39 (3), 385–400.

Wang, W., Wang, S., Ma, X., Gong, J., 2011. Recent advances in catalytic hydrogenation of carbon dioxide. Chemical Society Reviews 40 (7), 3703–3727.

Webster, C. R., Mahaffy, P. R., 2011. Determining the local abundance of Martian methane and its' $^{13}C/^{12}C$ and D/H isotopic ratios for comparison with related gas and soil analysis on the 2011 Mars Science Laboratory (MSL) mission. Planetary and Space Science 59 (2-3), 271–283.

Webster, C. R., Mahaffy, P. R., Atreya, S. K., Flesch, G. J., Farley, K. A., et al., 2013. Low upper limit to methane abundance on Mars. Science, 1242902.

Webster, C. R., Mahaffy, P. R., Atreya, S. K., Flesch, G. J., Mischna, M. A., Meslin, P.-Y., Farley, K. A., Conrad, P. G., Christensen, L. E., Pavlov, A. A., et al., 2015. Mars methane detection and variability at Gale crater. Science 347 (6220), 415–417.

Webster, C. R., Mahaffy, P. R., Atreya, S. K., Moores, J. E., Flesch, G. J., Malespin, C., McKay, C. P., Martinez, G., Smith, C. L., Martin-Torres, J., et al., 2018. Background levels of methane in Mars' atmosphere show strong seasonal variations. Science 360 (6393), 1093–1096.

Weiss, B. P., Yung, Y. L., Nealson, K. H., 2000. Atmospheric energy for subsurface life on Mars? Proceedings of the National Academy of Sciences 97 (4), 1395–1399.

Yakushev, V. S., Istomin, V. A., 1992. Gas hydrates self-preservation effect. In: *Physics and Chemistry of Ice*. Hokkaido University Press, Sapporo.

Yasuda, K., Ohmura, R., 2008. Phase equilibrium for clathrate hydrates formed with methane, ethane, propane, or carbon dioxide at temperatures below the freezing point of water. Journal of Chemical & Engineering Data 53 (9), 2182–2188.

Zahnle, K., 2015. Play it again, SAM. Science 347 (6220), 370–371.

Zahnle, K., Freedman, R. S., Catling, D. C., 2011. Is there methane on Mars? Icarus 212 (2), 493–503.

Zent, A. P., Hecht, M. H., Cobos, D. R., Wood, S. E., Hudson, T. L., Milkovich, S. M., DeFlores, L. P., Mellon, M. T., 2010. Initial results from the thermal and electrical conductivity probe (TECP) on Phoenix. Journal of Geophysical Research: Planets 115 (E3).

Zent, A. P., Howard, D. J., Quinn, R. C., 2001. H_2O adsorption on smectites: Application to the diurnal variation of H_2O in the Martian atmosphere. Journal of Geophysical Research: Planets 106 (E7), 14667–14674.

Zent, A. P., Quinn, R. C., 1997. Measurement of H_2O adsorption under Mars-like conditions: Effects of adsorbent heterogeneity. Journal of Geophysical Research: Planets 102 (E4), 9085–9095.